# Experimental Study of the In-Plane Behaviour of All-Masonry Infilled Frame Systems under Lateral Loading

By

Seyedali Hosseini

Submitted in partial fulfilment of the requirements
for the degree of Master of Applied Science

at

Dalhousie University
Halifax, Nova Scotia
December 2020

# TABLE OF CONTENT

# LIST OF TABLES

# LIST OF FIGURES

# ABSTRACT

This study is part of on-going experimental research, aiming to further investigate the in-plane behaviour of concrete masonry infills bounded by reinforced masonry frames (all-masonry infilled frames). A total of six all-masonry infilled frame specimens was tested under in-plane loading applied at the frame top beam level to specimen failure. The parameters studied included vertical loading, infill aspect ratio, presence of interfacial gaps, and cyclic loading. Two levels of vertical load were studied where the vertical load was applied through frame columns and held constant while the lateral load was monotonically increased to the specimen failure. In the infill aspect ratio study, two specimens with different aspect ratios (one squat and one slender) were constructed and tested under monotonic lateral loading. The last two specimens had window openings and pre-defined gaps and were tested under cyclic lateral loading. Load vs. displacement response, failure mode, and ultimate load for each specimen were obtained and discussed in detail. The performance of specimens was compared with previous studies conducted in the same research group. The experimental results were also used to evaluate the validity of stiffness and strength provisions contained in CSA S304.14 and TMS 402/602.16 masonry design standards.

The final failure mode for the infilled frame specimens was observed to be predominated by severe diagonal cracking extending into the boundary columns. Except for the specimen with side gaps and tested under cyclic loading, no evident corner crushing was observed. An increase in the vertical load resulted in an increase in the ultimate load but less ductile behaviour of specimens. When the vertical load was applied through frame columns vs. frame top beam, the above-mentioned trend was more pronounced. As the infill aspect ratio increased, the stiffness of the infilled frame decreased, and uplift at the specimen loaded side increased, indicating an increase in flexural behaviour in an otherwise shear action dominated behaviour. However, the ultimate strength appears to be controlled still by the length of the diagonal strut. The side gaps had a more effect on the specimen's stiffness while the top gap had more detrimental effect on the specimen's ultimate load. The comparison with previous studies showed that behaviour, strength, and ductility of all-masonry infilled frames are similar to, and in some cases, slightly better than infilled RC frames under either monotonic or cyclic loading. In general, CSA S304-14 tends to overestimate the stiffness in comparison with TMS 402/602. In the case of strength prediction, CSA S304 performed better than TMS 402/602, with predicted values closer to the test results.

# LIST OF ABBREVIATIONS AND SYMBOLS USED

## Symbols

| | |
|---|---|
| $A$ | Compressive area of infill diagonal strut |
| $A_{\mathrm{nv}}$ | Net shear area |
| $b_w$ | Total width of infill |
| $l_d$ | The length of the equivalent strut |
| $d_v$ | Effective depth for shear calculation |
| $E_b$ | Elastic modulus of beam |
| $E_c$ | Elastic modulus of column |
| $E_m$ | Elastic modulus of the infill, |
| $E_f$ | Elastic modulus of frame, |
| e | Eccentricity |
| $f'_m$ | Maximum compressive strength of masonry |
| $f_y$ | Yield strength of reinforcing bars |
| $h_c$ | Height of column |
| $h_m$ | Height of the masonry panel |
| $I_b$ | Moment of inertia of area of beam |
| $I_c$ | Moment of inertia of area of column |
| $K_{ini}$ | Initial stiffness |
| $K_{cr}$ | Cracking stiffness |
| $K_{ult}$ | Ultimate stiffness |
| $l_m$ | Length of the masonry panel |
| $M_f$ | Factored moment at section |
| $\frac{M_f}{V_f d}$ | A value that shall not be less than 0.25 and more than 1 |
| $N_u$ | Normal compressive force |
| $P_1$ | Vertical component of diagonal compression force |
| $P_{cr}$ | Crack strength |
| $P_d$ | Compressive force acting normal to the sliding plane |
| $P_{ult}$ | Ultimate strength |
| $R_d$ | Ductility ratio |

| | |
|---|---|
| $t_e$ | Effective width of infill |
| μ | Coefficient of friction between the interface of the infill and frame |
| $v_m$ | Shear strength attributed to the masonry |
| $V_n$ | Nominal shear strength |
| $V_r$ | Ultimate load of different failure modes |
| $V_f$ | Factored shear at the section under consideration |
| $w$ | The width of the equivalent strut |
| $w_{eff}$ | Effective strut width based on CSA |
| $\gamma_g$ | Factor to account for partially grouted or ungrouted walls that are constructed of hollow or Simi-solid units |
| $\lambda$ | Relative stiffness parameter |
| $\theta$ | Slope of the strut with respect to the horizontal axis |
| $\phi_m$ | Masonry resistance factor |
| $\Delta_f$ | Displacement at failure |
| $\Delta_u$ | Displacement at failure |
| $\Delta_y$ | Yield displacement |
| $\alpha_b, \alpha_l$ | Contact length between the beam and the infill |
| $\alpha_c, \alpha_h$ | Contact length between the column and the infill |
| χ | Factor to account for direction of compressive stress in masonry member relative to the direction used for determination of $f'_m$ |

## Abbreviations

| | |
|---|---|
| ASTM | American Society for Testing and Materials |
| CC | Corner crushing |
| CMU | Concrete masonry unit |
| CSA | Canadian Standards Association |
| CV | Coefficient of variation |
| DC | Diagonal cracking |

| | |
|---|---|
| DSC | Diagonal strut compression |
| IF-AS-0.5 | Infilled frame with aspect ratio of 0.5 |
| IF-AS-1.3 | Infilled frame with aspect ratio of 1.3 |
| IF-LA-80 | Infilled frame with 80 kN vertical loading on columns |
| IF-LA-160 | Infilled frame with 160 kN vertical loading on columns |
| IF-W-SG-C | Infilled frame with window opening and side gaps under cyclic loading |
| IF-W-TG-C | Infilled frame with window opening and top gap under cyclic loading |
| LVDT | Linear variable differential transformer |
| MSJC | Masonry Society Joint Committee |
| NBCC | National Building Code of Canada |
| RC | Reinforced concrete |
| SS | Sliding shear |
| TMS | The Masonry Society |

# ACKNOWLEDGEMENTS

None of this could have been possible without all the hard work, support, encouragement, and love by my wife. Thank you for everything and keeping me on the right track.

I would like to express my deepest gratitude to my supervisor Dr. Yi Liu for her irreplaceable guidance, monitoring, and generous support. I feel fortunate that I have her as my supervisor. Without her direction and patience, this dissertation would not have been possible.

I would also like to thank my committee members, Dr. Pedram Sadeghian and Dr. Navid Bahrani, for taking the time to review this dissertation and provide valuable feedback.

I would like to thank Mr. Jordan Maerz, and Mr. Jesse Keane for their kind assistance during specimen construction and the test set up.

I would also like to thank Mr. Andrew Smith for providing me with the materials and a professional mason for the construction of specimens.

My thanks also go to the Canadian Concrete Masonry Producers Association for providing me with financial assistance.

Lastly, I would like to thank my family for their vital support, inspiration, and unconditional love. Work ethic is hereditary!

# CHAPTER 1 INTRODUCTION

## 1.1 BACKGROUND OF MASONRY INFILED FRAMES

Masonry is one of the oldest construction materials dating back ten thousand years ago. Masonry materials such as natural stones, cut stones and mud bricks were predominately used in construction prior to 1900s (Drysdale and Hamid 2005). They have gradually evolved to include calcium silicate, oven-dried clay (brick masonry), and more recently, concrete masonry units (CMUs). In North America, both concrete masonry units and masonry bricks are commonly used in masonry construction while the former is more often used in structural masonry for load bearing members and the latter is used in non-structural applications such as building veneers. With the development of steel and concrete construction industry, masonry also finds its application in the construction of masonry infilled frames where masonry products coexist with either concrete or steel materials.

Masonry infilled frames refer to either reinforced concrete (RC) or steel frames infilled with masonry materials (CMUs or bricks). They are often used in a building either as partition walls to separate spaces or cladding to complete the building envelope. If they are built in tight contact with their bounding frames, they will be designed as "participating infills" where their contribution to the stiffness, strength, and ductility of the frame system needs to be carefully considered. In essence, the contribution of the masonry infills is dependent on the extent of interaction between the infill and its bounding frame. Many studies on the general subject of in-plane behaviour of masonry infilled frames has been conducted in the past six decades. These studies mostly concentrated on developing a simple and rational approach to quantify the infill-frame interaction

in the stiffness and strength design of the frame system. A detailed literature review is provided in Chapter 2. In general, these studies have shown that behaviour of the masonry infilled frames is complex and is influenced by many factors such as the geometric and material properties of both the infill and its bounding frame, the interfacial condition, and loading conditions to just name a few. For design, the current Canadian masonry design standard (CSA S304-14) and American standard (TMS 406/602) both provide design equations for calculation of the frame system stiffness and strength considering the infill effect.

At present, reinforced concrete and steel are two main materials to be used as masonry infilled frames. Hence, the previous research and its findings have been strictly applicable to those types of infilled frames. While the construction technology for building either a RC or steel frame with masonry infills is mature, the fact that either type would require a coordination of two trades in both design and construction has prevented the masonry infills from being relied upon as structural elements in industry practice. In this case, masonry infills are often designed by architects while the frame structure is designed by structural engineers. The masonry infills are often treated as non-participating and non-structural elements, despite a large amount of physical evidence of the benefit of infills to the system behavior and availability of code provisions.

## 1.2 ALL-MASONRY INFILLED SYSTEM

The study of all-masonry infilled frame systems began in 2018 within the research group at Dalhousie University as part of an effort to develop an alternative to the current infilled frame system. An all-masonry infilled frame is conceptually similar to a masonry infilled RC frame with the difference being that the bounding frame is also made of masonry, as seen in Figure 1.1. Masonry reinforced columns and tied beams form the masonry frame while the masonry infill can

be constructed in the same manner as in the conventional infilled RC frames. Masonry columns are constructed with custom-made boundary element units with larger open areas for concentrated reinforcement and grouting. The masonry beam is formed using the bond beam and tied into columns. The masonry infills can remain unreinforced. From both construction and design perspectives, all-masonry infilled frames are advantageous as design for the frame and infill can be carried out in the same consulting firm and constructed at the same time with one material.

As a multi-phased study, the phase I was conducted by a colleague in the same research group (Foroushani 2019) where six all-masonry infilled frame specimens were tested with design parameters including masonry infill strength, infill reinforcement, and presence of vertical loading. It was found that the performance of all-masonry infilled frames was comparable to that of masonry infilled RC frames and in some cases, was even better. The details of work conducted by Foroushani (2019) are elaborated in Chapter two. Given the initial promising results, this study is the phase II study where more design parameters are investigated.

Figure 1.1 The proposed all-masonry infilled frame

## 1.3 RESEARCH OBJECTIVES

Continuing the phase I study, the main objective of this study is to further investigate experimentally important geometrical and loading design parameters of all-masonry infilled frames. The parameters considered in this study included infill aspect ratio, infill opening, interfacial gap, and the presence of axial loading. The effect of cyclic loading was also considered. A total of six all-masonry infilled frame specimens were tested. These specimens were subjected to in-plane static or cyclic loading. The results were compared with the results from phase I study (Foroushani 2019) as well as previous study conducted in the same research group on masonry infilled RC frames (Steeves 2017) as appropriate. Detailed research objectives are summarized in the following:

1. To augment experimental results on the capacity and behaviour of all-masonry infilled frames under in-plane loading.
2. To analyze the effect of the above-mentioned design parameters on the performance of all-masonry infilled frame systems.
3. To assess the performance of all-masonry infilled frame systems against masonry infilled RC frames.
4. To evaluate the efficacy of both CSA S304 and TMS402/602 in terms of stiffness and strength calculation based on the results obtained from this study.

## 1.4 OUTLINE OF RESEARCH

This thesis is organized in six chapters. The present chapter introduces the objectives and scope of the research. Chapter 2 presents a comprehensive literature review of masonry infilled frames in general and existing analytical methods for the stiffness and strength calculations of such systems; the research conducted at Dalhousie University. Chapter 3 provides a detailed description of the experimental program. Chapter 4 contains a description and discussion of the results from the specimens and auxiliary tests. Chapter 5 presents an evaluation of performance of all masonry infilled frames by comparing the experimental results with the analytical values and previous experimental results on RC frames. Finally, a summary of results, main conclusions and recommendations for future work are presented in Chapter 6.

# CHAPTER 2 LITERATURE REVIEW

## 2.1 INTRODUCTION

Since the all-masonry infilled frame is a new type of infilled frame system, the existing literature specifically on this type of system is limited to the research conducted by the Dal research group. Considering that the fundamental behavioral characteristics for masonry infills are similar between different frame types, this chapter first provides a review of general behaviour and failure modes and parametric studies on masonry infills bounded by RC and steel frames that may be relevant to this study. The experimental studies conducted in the same research group by Foroushani (2019) on all-masonry infilled frames and by Steeves (2017) on masonry infilled RC frames under cyclic loading are presented and their results are used in the later comparison with the results of this study. Finally, the current Canadian and American masonry design provisions with respect to masonry infilled frames are presented as their applicability to the all-masonry infilled frames is evaluated in Chapter 5.

## 2.2 IN-PLANE BEHAVIOUR OF MASONRY INFILLED FRAMES

### 2.2.1 General behaviour

The behavior of masonry infilled frames is dependent on the extent of interaction between the infill and its bounding frame throughout loading history. Polyakov (1960) was the first to observe this through an experiment of masonry infilled steel frame. He described that at relatively low level of lateral force, the infill and frame acted together to provide shear resistance to deformation. As load increased, due to the different modes of deformation of the infill and the frame, they began to separate and diagonal cracks connecting loaded corners began to form. As cracking developed and

the frame further deformed, at failure, the contact area between the infill and frame remained at two diagonal corners which are in compression, as shown in Figure 2.1. Hence, a masonry infill was considered to be replaceable using a diagonal strut connecting loaded corners, which has since formed the basis for the so-called “diagonal strut” concept. In this method, the stiffness and strength contribution of the masonry infill to the frame can be estimated using a strut of a certain width.

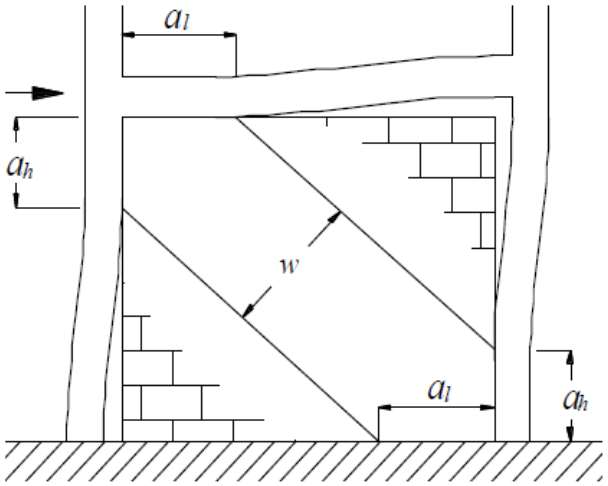


Figure 2.1 “Diagonal strut” concept: in-plane reaction of infilled frames (Holmes1961)

### 2.2.2 Diagonal strut method

Following this initial work, the diagonal strut concept has been further studied and developed to become the main method of analysis for masonry infill walls and has been adopted in various forms in most masonry design standards across the world. The key factor of the existing studies based on the diagonal strut concept was to determine the accurate contact area and thus the width of the strut for the stiffness and strength consideration of the masonry infill.

#### *2.2.2.1 Single-Strut Model*

Both experimental and analytical studies have been conducted to develop analytical models for calculating the strut width, w. A detailed literature review of these models can be found in Foroushani (2019). Table 2.1 provides a summary of these models for ease of reference with the geometric symbols shown in Figure 2.2. It can be concluded that two factors, i.e., the stiffness ratio of infill to frame and the slenderness ratio of the infill panel, seem to be the most influential in determining the strut width, w. The effect of both is captured through the factor, λ, in most models.

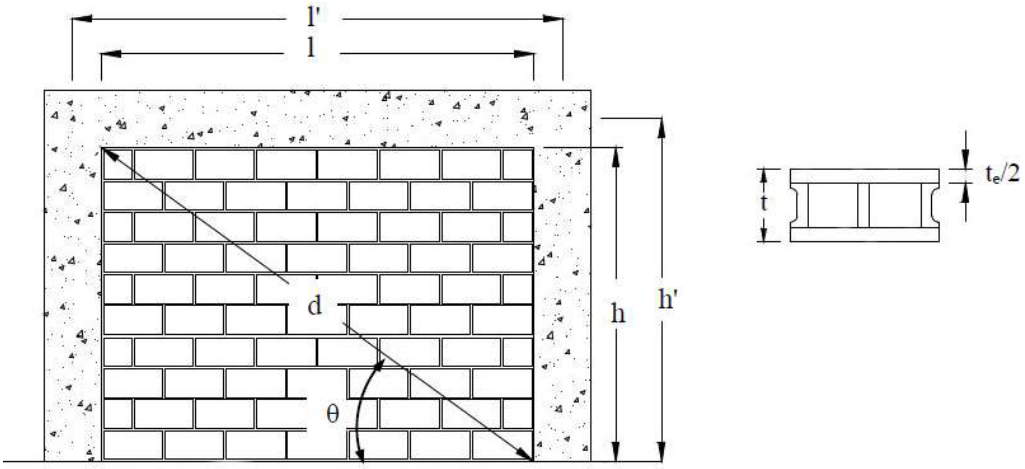


Figure 2.2. Geometric parameters in masonry infilled frames

Table 2.1 Summary of analytical models of the equivalent diagonal strut width

| Author | Equation | Type of Infill and Frame | Note |
|---|---|---|---|
| Smith and Carter (1969) | $w$=0.5 $(\frac{1}{h})^{-0.445}(\lambda_h h')^{0.335d}(\frac{1}{h})^{0.064}$ $\lambda_h = \sqrt[4]{\frac{E_I t \sin(2\theta)}{4E_c Ih}}$ | Experimental study Concrete masonry infilled RC frame | $\lambda_h$: Relative stiffness of the masonry infill and the frame θ: Slope of the infill diagonal to the horizontal. $E_I$ and $E_c$: Young's moduli of the infill and frame column |
| Mainstone (1971) | $w/d$=0.175$(\lambda_h h')^{-0.4}$ (4≤$\lambda_h h'$≤5) $w/d$=0.16$(\lambda_h h')^{-0.3}$ ($\lambda_h h' \geq 5$) | Experimental study Concrete masonry infilled steel frame | $\lambda_h$: Relative stiffness parameter |
| Liauw and Kwan (1984) | $w=\frac{0.86hcos\theta}{\sqrt{\lambda_h h}}$ ,$or$ $0.45hcos\theta$ | Finite element study Masonry infilled frame | θ: Slope of the infill diagonal to the horizontal. |
| Dawe and Seah (1989) | $w=\frac{2\pi}{3}(\frac{\cos\theta}{\lambda_P}+\frac{\sin\theta}{\lambda_T})$ $\lambda_P = \sqrt[4]{\frac{E_I t \sin(2\theta)}{4E_c I_P h'}}$ $\lambda_T = \sqrt[4]{\frac{E_I t \sin(2\theta)}{4E_c I_T h'}}$ | Experimental/Numerical study Concrete masonry infilled steel frame | t: Thickness of panel $\lambda_P$: Relative stiffness correlated to the beam $\lambda_T$: Relative stiffness correlated to the adjacent column $E_I$ and $E_c$: Elastic moduli of the infill and the RC frame |
| Hendry (1998) | $w = 0.5\sqrt[2]{\alpha_h + \alpha_l}$ $\alpha_h = \frac{\pi}{2}\sqrt[4]{\frac{E_C I_C h}{2E_I \,\mathrm{tsin}(2\theta)}}$ $\alpha_l = \pi\sqrt[4]{\frac{E_C I_b L}{2E_I \,\mathrm{tsin}(2\theta)}}$ | Numerical study Frame-infill system | $E_I$ and $E_c$ : Young's moduli of frame column and masonry infill $I_C$ and $I_b$: Moment of inertia of column and beam $\alpha_h$ and $\alpha_l$: Contact length between infills and column and beam |
| Flanagan and Bennett (1999) | $w = \frac{\pi t}{C\lambda_h \cos\theta}$ | Experimental study Clay tile infilled steel frame | C: Empirical constant varies with the in-plane drift t: Thickness of infill |

Table 2.1 Summary of analytical models of the equivalent diagonal strut width (cont'd)

| | | | |
|---|---|---|---|
| Al-Chaar (2002) | for $l/h \geq 1.5$<br>$w=0.0835Cd(1+2.574/\lambda_h h')$<br><br>for $l/h=1$<br>$w=0.1106d(1+6.027/\lambda_h h')$<br><br>$C = -0.3905(l/h)+ 1.7829$ | Experimental/numerical study<br>Concrete and brick masonry infilled RC frame | $d$: Infill diagonal length<br>C: Non-dimensional factor to consider aspect ratio effect |

*2.2.2.2 Multiple-Strut Model*

Some researchers suggested that a single strut may not be adequate to capture the effect of the infill exerted on the shear and moment resistance of the boundary frame. Thus, multi-strut models were also proposed. The following presents three such models. Crisafulli and Carr (2007) proposed a model consisting of two parallel struts and a shear spring to consider sliding shear and diagonal tension of the infill, as shown in Figure 2.3. However, the required parameters were found through a complicated calibration process using a few specific infill cases, which makes it difficult to be adopted in practice.

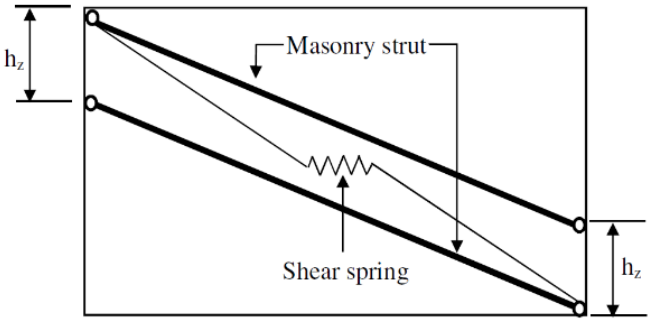


Figure 2.3 Two struts model (Crisafulli and Carr 2007)

Burton and Deierlein (2014) developed a "compression-only dual-strut model" composed of an elastic frame members for struts and zero-length spring elements positioned at the end of frame members to account for the loss in the capacity of axial load due to column shear failure. This

model is illustrated in Figure 2.4. This model is more to address the effect of the infill on the boundary frame but in terms of the infill itself, it is not too different from the single-strut model.

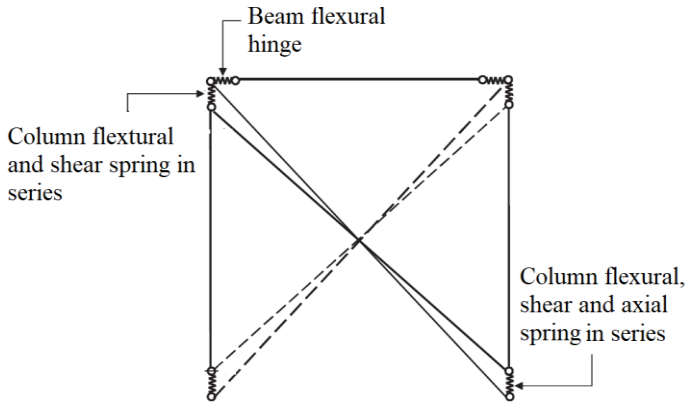


Figure 2.4.compression-only dual-strut model (Burton & Deierlein 2014)

El-dakhakhni et al. (2003) proposed the "three-Strut Model" as illustrated in Figure 2.5. This model composed of three struts, creating two diagonal regions for the panel where the red circles indicate the beam-column joints. The strut total area is expressed as follows:

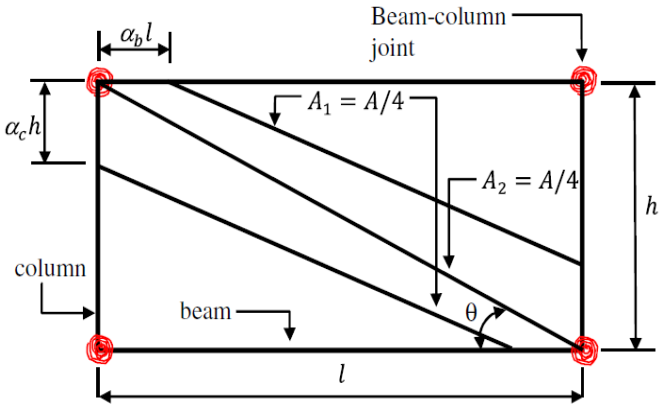


Figure 2.5. Multiple diagonal strut models (El-Dakhakhni et al., 2003)

$$A_d = \frac{(1-\alpha_c)\alpha_c h t}{\cos\theta} \qquad (2\text{-}1)$$

The contact lengths $\alpha_c h$ and $\alpha_b l$ were proposed to be associated with the plastic moment capacities of the beam, column and beam-column connection. Calibrated using a limited number of steel framed masonry infill specimens, this model was found to overestimate the strength and ductility of infilled frames in general.

### 2.2.3 Failure modes of infilled frames

There are some possible failure mechanisms for infilled frames. The following five failure modes have been recognized as common types of failure in masonry infilled frames: 1) Corner Crushing (CC) which causes failure of the infill in the loaded corners due to compression; 2) Sliding Shear (SS) in which horizontal sliding through bed joint happens. This failure mode usually comes from week mortar joint; 3) Diagonal strut compression (DSC) that appears in the central region of the diagonal strut due to out-of-plane buckling, which might be caused by slender infills. 4)Diagonal Cracking (DC) that observed through diagonal strut when the diagonal strut is subjected to compression and diagonal tension crack appears along the diagonal direction of the infill; and 5) Frame Failure (FF) that can be in the form of ductile plastic hinge development or sudden shear failure of the columns. These failure modes are shown in Figure 2.6. For masonry infilled steel or RC frames of typical material and geometry, corner crushing was identified as the most common failure mode. The diagonal tension cracking was also observed to often initiate the failure although the final failure.

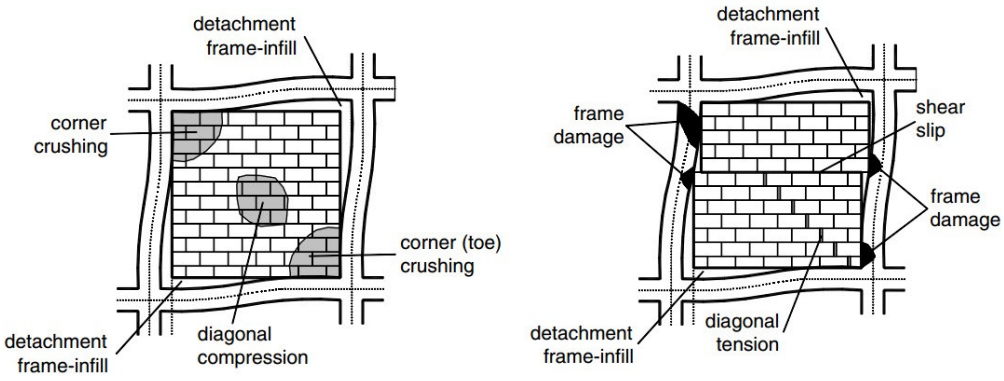


Figure 2.6. failure modes of infilled frames(Asteris et al. 2013)

### 2.2.4 Strength analysis of infilled frames

Several strength equations have been proposed to calculate the capacity of infilled system with different failure modes as explained above. A summary of proposed equations is shown in Table 2.2. As can be seen, most equations were proposed for corner crushing (CC), sliding shear (SS), and diagonal cracking (DC) as they were mostly often observed failure. These models were mainly empirical and based on the diagonal strut concept, relating the lateral strength of the infill to some forms of strut width. It should be pointed out that each model, whether developed based on experimental results or numerical studies, was calibrated against a set of experimental results of material and geometric properties of the infilled systems specific to the study. Most often, these experimental results were limited in the number of specimens and range of variation of parameters. Thus, none of these models is found universally applicable to all types of masonry infilled frames.

Table 2.2 Summary of proposed strength evaluation equations for masonry infilled frames

| Author | Equation | Type of Infill and Frame | Note |
|---|---|---|---|
| Mainstone (1971) | $H_{CC}$= $0.56(\lambda_h h)^{-0.875} f'_m\ h'\ \ tcot(\theta)$ $4 \leq \lambda_h h' \leq 5$<br>$H_{CC}$= $0.52(\lambda_h h)^{-0.8} f'_m\ h'\ tcot(\theta)\ \lambda_h h' \geq 5$ | Experimental study Concrete masonry infilled steel frame | $\lambda_h$: Relative stiffness parameter (Eq.**Error! Reference source not found.**) $f'_m$ = Masonry infill compressive strength |
| Rosenblueth (1980) | $H_{SS}$= $(0.9+0.3\frac{1}{h})\ f_{bs} ht$<br>$H_{CC}$= $\frac{2}{3}\alpha_c t\ f'_m\ sec(\theta)$<br>$\alpha_C = \frac{\pi}{2}\sqrt[4]{\frac{4E_C I_C h}{E_I\ \mathrm{tsin}(2\theta)}}$ | Experimental study Masonry infilled RC frame | $f_{bs}$= Shear bond strength between the masonry and mortar<br>$\alpha_C$= Contact length of the infill and column |
| Smith and Coull (1991) | $H_{CC} = f'_m t\ \frac{\pi}{2}\sqrt[4]{\frac{4E_C I_C h'}{E_I t}}$ | Numerical study All material infilled frames | (Terms are defined before) |
| Paulay and Priestley (1992) | $H_{DT}$= $\frac{\pi}{2} t\ df'_m \cos\theta$ | Numerical study Masonry infilled RC frames | (Terms are defined before) |
| Saneinejad and Hobbs (1995) | $H_{SS}$=$\min\begin{cases}\frac{\gamma\tau_0 td}{1-0.45\tan\theta}\cos\theta \\ 0.83\gamma td\cos\theta\end{cases}$<br>$H_{DT} = 2\sqrt{2} td f_t \cos^2\theta$<br>$H_{CC} = (1-\alpha_c)(\alpha_c h) t\sigma_c + (\alpha_b l)(t\tau_b)$ | Numerical study All material infilled frames | $f_t$= Tensile strength of infill<br>$\gamma$= Load factor<br>$\alpha_c h$ and $\alpha_c$ = Contact length and contact stress between the column and infill<br>$\alpha_b$ and $\tau_b$= Contact length and contact stress between the beam and infill |
| Mehrabi (1996) | $H_{SS}$= $0.34A_w + 0.9P_w$ | Experimental study Masonry infilled RC frames | $A_w$= Horizontal cross section of infill<br>$P_w$= Vertical load |
| Flanagan and Bennett (1999) | $H_{CC}$= $K_{CC} t\ f'_m$ | Experimental study Clay tile infilled Steel frame | $K_{CC}$= Empirical constant for corner crushing with a mean value of 246 mm for clay tile infills |

### 2.2.5 Irregular infills

The above presented analytical models/equations are only applicable to "regular infills" subjected to static lateral loading. In this context, "regular infills" refer to those constructed without perforations and there are no gaps at the infill-to-frame interface. For "irregular infills" where infill openings and interfacial gaps are present, or loading is cyclic, there are no available design guidelines accepted by the design community. Research on the "diagonal strut" concept to incorporating the effect of "irregularities" in infills is on-going and some findings on parameters relevant to this study are summarized in the following sections.

#### *2.2.5.1 Interfacial Gap*

The presence of interfacial gaps between beam and infill or column and infill causes a significant decrease in the stiffness and capacity of the infilled frame. Based on studies conducted by Yong (1984) and Dawe and Seah (1989a), the presence of a top gap of 20 mm between beam and infill results in a 50% reduction in the initial stiffness and strength of the infilled system. On the other hand, Flanagan (1994) stated that a 25 mm side gap between the column and infill did not affect ultimate capacity; however, a non-symmetrical cracking shape was observed. All previous studies suggested the presence of a gap significantly reduces the stiffness at the initial loading point. Once the gap was closed due to loading at the loaded corner, a marked increase in stiffness was observed. Further, a top gap seems to have more detrimental effect on the capacity of the infilled frame than the side gap. However, the latter affects more on the displacement and ductility of the system.

#### *2.2.5.2 Openings*

Infill openings were also reported to result in reductions in the stiffness and capacity of the infilled frame. Both opening size and location can affect the degree of the reductions. Mallick and Garg (1971) suggested the center of infill is the best location for opening. However, Kakaletsis and

Karayannis (2007) who tested RC infilled frames indicated that a better performance was observed when the location of opening was close to the edges of the infill to reduce the interruption of the diagonal strut formation. Soon (2011) showed that the reduction in infill capacity and the opening size do not have a linear relationship.

#### *2.2.5.3 Cyclic Loading*

Quasi-static cyclic loading can be defined as a testing procedure where slow cycles of loading, simulating seismic activity, are applied in order to study the performance of structures and structural members for crack propagation, hierarchy of collapse, and associated levels of damage. In comparison to monotonic loading, which assesses a material's yielding point, quasi-static cyclic gives insight into the hysteric characteristics such as strength and stiffness deterioration, energy dissipation, and ductility. The quasi-static loading is considered a good alternative for understanding the structural seismic performance in lieu of more sophisticated and advanced testing strategies such as pseudo-dynamic or shaking table testing. While a majority of experimental research on infilled frames has been conducted using monotonic loading, those conducted under cyclic loading conditions were limited.

Klingner et al. (1996) and Mehrabi et al. (1996) conducted experimental tests on half-scaled single storey infilled RC frame specimens subjected to monotonic or quasi-static cyclic loading. Results showed that infills can significantly increase the stiffness, strength and energy dissipation capacity of the infilled system, even if the system is under in- and out-of-plane lateral loads simultaneously. It was also found that specimens subjected to cyclic loading showed lower lateral resistance and faster strength degradation than their monotonically loaded counterparts.

A full-scale experimental study was conducted by Pujol and Fick (2010). They tested a three-storey concrete building and investigated the effect of masonry infills on the drift capacity of

concrete frames. The presence of infills was proven to enhance the performance of the frame in terms of constraining the "inter-storey drift" and increasing the lateral stiffness and base shear strength up to 500% and 100%, respectively.

Al-Nimry (2014) performed quasi-static cyclic load testing on 1/3 scale RC frames with limestone masonry infills. Experimental results showed a substantial decrease in ductility with the presence of axial load and reduced load capacity with the presence of openings.

## 2.3 EXPERIMENTAL STUDIES CONDUCTED AT DALHOUSIE UNIVERSITY

Two experimental studies conducted in the same research group are of relevance to this study and their findings are described below. One was conducted by Steeves (2017) on masonry infilled RC frames subjected to cyclic loading and the other was conducted by Foroushani (2019) on all-masonry infilled frames subjected to static loading. The geometry, dimensions, and material properties of the infills and frame are kept as consistent as appropriate among all three studies to enable later results comparison.

Steeves (2017) investigated the effect of gaps and openings on the in-plane behaviour of masonry infilled RC frames subjected to quasi-static cyclic loading. One bare frame, two specimens with gaps and two with window opening accounting for 20% of the infill area were loaded to failure. All infills were constructed with the same dimensions at 980 mm high and 1350 mm wide. The strength, stiffness, ductility, and energy dissipation of the specimens were discussed. The geometry and dimension of the infill and the boundary frames, as well as the gap size and location and infill openings used in the Steeves' study on infilled RC frames were adopted in this study as much as possible. The test setup and procedure were also kept the same between two studies. The objective

was to be able to compare the performance of a masonry infilled RC frame vs. an all-masonry infilled frames for a given set of parameters.

Foroushani (2019) tested a masonry bare frame and five all-masonry infilled frame specimens. The parameters included infill strength, infill horizontal reinforcement, and presence of vertical load applied through the top frame beam. For all specimens, masonry infills were constructed with un-grouted concrete masonry blocks and did not have any vertical reinforcement. According to Foroushani (2019), all-masonry infilled frames, in general, exhibited comparable or even greater ductility than their RC frame counterparts. When the strength is concerned, the all-masonry infilled frames attained similar and, in some cases, higher strengths than the RC frame counterparts. The study showed the potential for this all-masonry infilled frame system to be used as a lateral load resisting system but more experimental tests covering more parameters are needed.

## 2.4 NORTH AMERICAN DESIGN STANDARDS AND CODES

As mentioned previously, the diagonal strut method has been adopted in both the Canadian and American masonry design standards for design of masonry infills. Under the framework of this method, different equations for the strut width and strength calculations are, however, specified in the two standards. Also, it should be pointed out that the provisions contained in both standards only address the “regular infills”. Neither standards provide explicit treatment for infills when “irregularities” exists in the infill.

### 2.4.1 CSA S304.14

The Canadian masonry design standard CSA S304.14 (2014) follows a semi-empirical method through the diagonal strut concept for the design of infills. Mainly based on the work done by

Stafford-Smith and Carter (1969), the strut width, w, is correlated with contact areas between the infill and the frame beam and column, $\alpha_h$ and $\alpha_l$, as illustrated in Figure 2.7.

$$w = \sqrt{{\alpha_h}^2 + {\alpha_l}^2} \tag{2-2}$$

$$\alpha_h = \frac{\pi}{2}\sqrt[4]{\frac{4E_f I_c h}{E_m t_e \sin 2\theta}};\ \alpha_l = \pi\sqrt[4]{\frac{4E_f I_b l}{E_m t_e \sin 2\theta}} \tag{2-3}$$

where $t_e$ is the effective thickness of the masonry infill, $E_f$ is the elastic modulus of the frame material, $I_b$ and $I_c$ are the moment of inertia of the beam and column, respectively. The effective strut width $w_{eff}$ is then considered as w/2 as the stress distribution in that width can be considered uniform.

For stiffness consideration, S304-14 specifies that the effective strut width be further reduced to $0.5w_{eff}$. To determine the in-plane capacity of masonry infills S304-14, investigates corner crushing (CC), shear sliding (SS), and diagonal cracking (DC) failure modes. In all cases, the strength equations are related to the effective diagonal strut width.

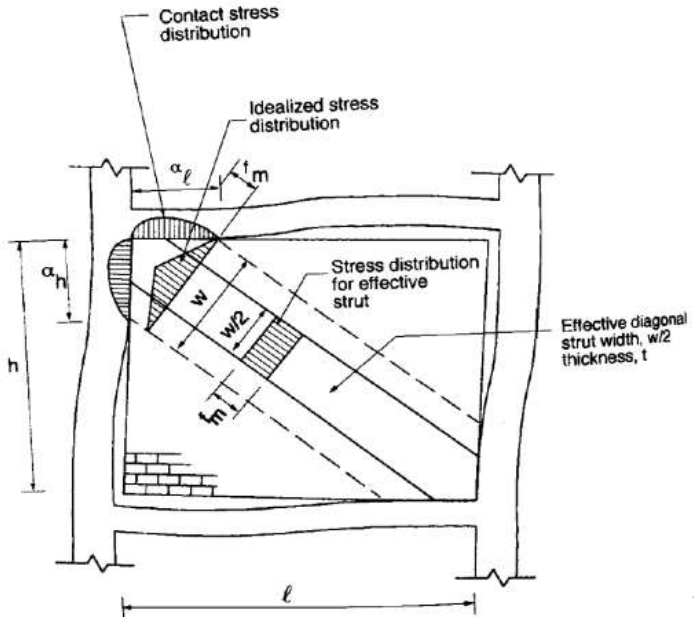


Figure 2.7 Illustration of geometric properties of the equivalent diagonal strut
(Adapted from Drysdale and Hamid 2005)

### 2.4.2 TMS 402/602

The American standard TMS 402/602 specifies that the infill be considered as an equivalent strut to calculate the stiffness of the infilled system. Based on the research conducted by Flanagan and Bennett (1999), the width of the diagonal strut is obtained by the following equation:

$$w = \frac{0.3}{\lambda_{strut} \cos \theta_{strut}} \tag{2-4}$$

where $\lambda_{strut}$ is the stiffness parameter and expressed as below, for the design of concrete and clay masonry infills:

$$\lambda_{strut} = \sqrt[4]{\frac{E_m t_e \sin 2\theta}{4 E_{bc} I_{bc} h}} \tag{2-5}$$

where $E_{bc}$ and $I_{bc}$ are the Young's modulus and moment of inertia of bounding columns, respectively, and $t_e$ is the effective thickness of the infill. The factor of 0.3 is used to account for the potential damage sustained by mortar joints with no damage to the infill (Flanagan and Bennett 1999). Although similar in concept, the TMS equation is a simplified diagonal strut equation where the bounding beam effect is considered negligible and the width is largely dependent on the bounding column stiffness.

In TMS 402/602, the in-plane strength of infilled frames is also evaluated based on three failure modes, i.e., corner crushing, sliding shear, and 25 *mm* lateral displacement of the frame. It should be pointed out that for corner crushing, the TMS simply uses a constant term of 6 inches as the diagonal strut width to account for the compressive capacity of the diagonal strut.

# CHAPTER 3 EXPERIMENTAL PROGRAM

## 3.1 GENERAL

This study experimentally investigates the strength and behaviour of all-masonry infilled frame systems. A total of six all-masonry infilled frame specimens was subjected to either static or cyclic in-plane loading to failure. Along with testing of the infilled specimens, auxiliary tests were also conducted to obtain the material properties of concrete masonry units (CMUs), mortar, grout, reinforcing steel and masonry prisms. The following sections provide a detailed description of infilled frame specimens, test setup and procedure while the associated auxiliary tests are presented in Appendix A.

## 3.2 INFILLED FRAME SPECIMENS

Table 3.1 provides a description of design parameters of the six specimens tested in the experimental program. The first four specimens were tested under monotonic lateral loading, two of which were used to study the effect of axial loading on the in-plane behaviour (IF-LA-80 and IF-LA-160) with two levels of axial loads of 80 and 160 kN respectively, and the other two were used to study the effect of infill aspect ratio (IF-AS-0.5 and IF-AS-1.3) with an aspect ratio, H/L, of 0.5 and 1.3 respectively. The last two specimens were tested under cyclic lateral loading (IF-W-TG-C and IF-W-SG-C) and they had a pre-defined gap of 12 mm located at two interfaces, including: 1) at top beam-infill interface (Top Gap), and 2) at two column-infill interfaces (Side Gap). These two specimens also had a window opening accounting for 17% of the infill area. The capacity of the hydraulic actuator used to apply the cyclic loading is 100 kN. The two specimens

were thus weakened with both interfacial gap and infill opening to ensure they can be tested to failure within the actuator's capacity. In addition, similar specimen design parameters were also used in the experimental study conducted by Steeves (2017) on masonry infilled RC frames. The parameters were thus kept the same to aid later comparisons. Figures 3.1 to 3.3 illustrate the geometry, dimension, and design parameters for these specimens.

Table 3.1 Summary of test specimens

| Specimen ID | Aspect ratio (H/L) | Window opening | Gap | Type of load |
|---|---|---|---|---|
| IF-LA-80 | 0.73 | - | - | Lateral and 80 kN axial |
| IF-LA-160 | 0.73 | - | - | Lateral and 160 kN axial |
| IF-AS-0.5 | 0.5 | - | - | Lateral static |
| IF-AS-1.3 | 1.3 | - | - | Lateral static |
| IF-W-TG-C | 0.73 | 17% | 12mm Top gap | Lateral cyclic |
| IF-W-SG-C | 0.73 | 17% | 12mm Side gap (6mm each side) | Lateral cyclic |

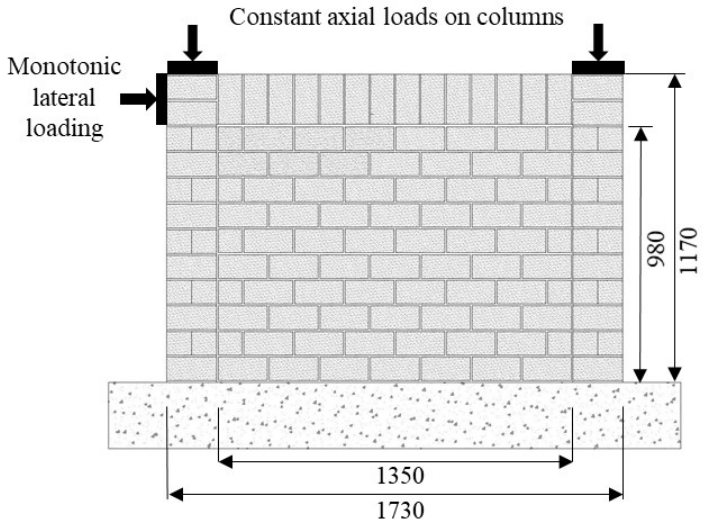


Figure 3.1 Geometry and applied load on specimens IF-LA-80 and IF-LA-160 (unit:mm)

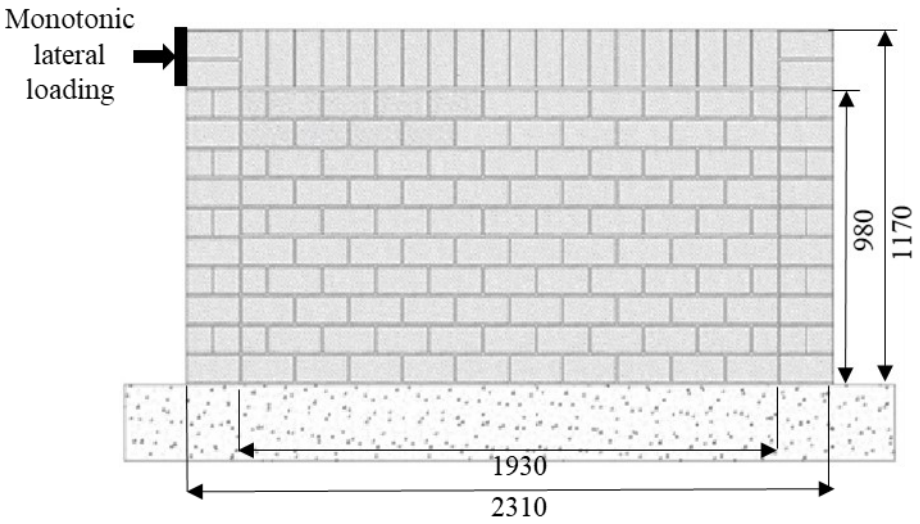


(a)

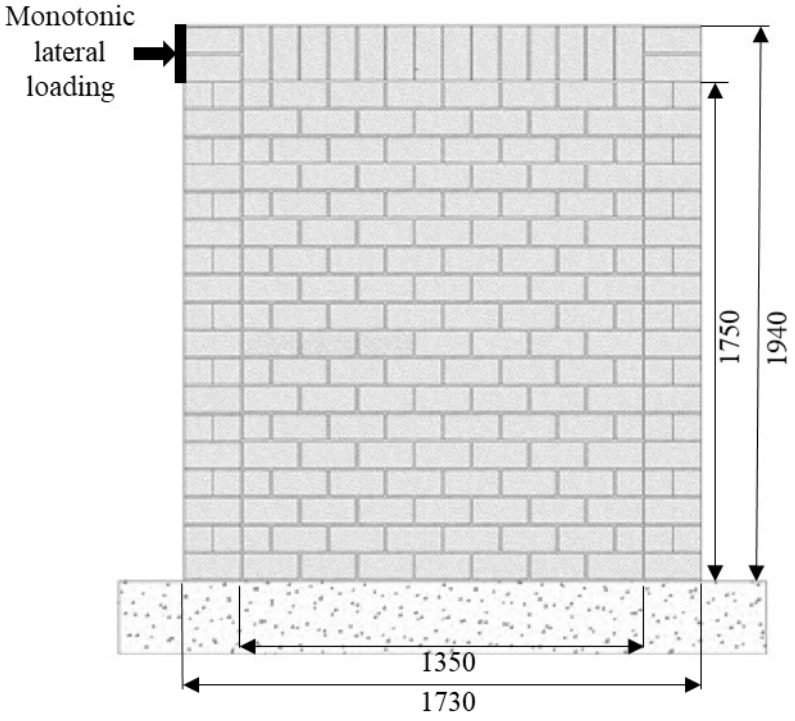


(b)

Figure 3.2 Geometry and applied load on specimens (a) IF-AS-0.5 and (b) IF-AS-1.3 (unit:mm)

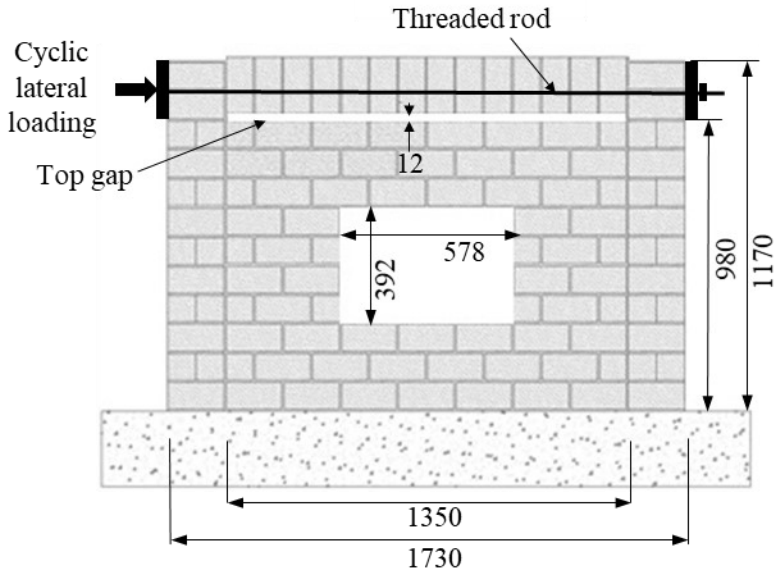


(a)

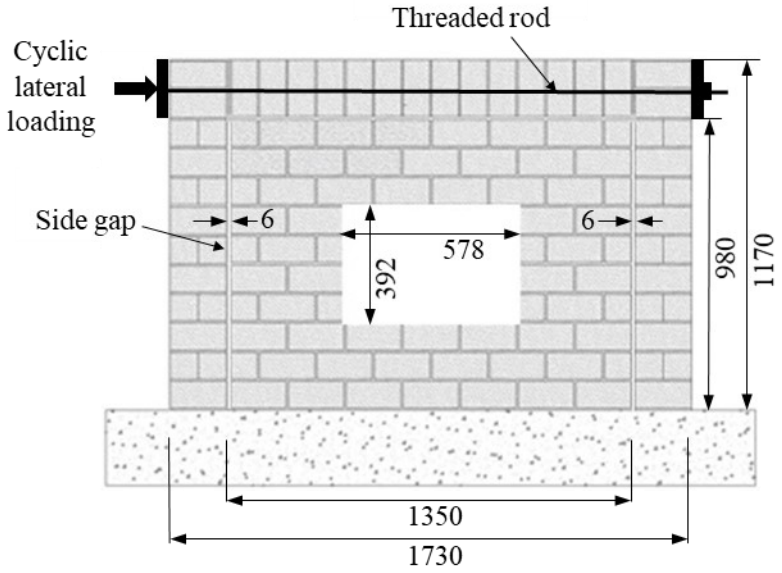


(b)

Figure 3.3 Geometry and applied load on specimens (a) IF-W-TG-C and (b) IF-W-SG-C (unit:mm)

All the masonry infills were constructed as unreinforced and un-grouted using the custom-made, half-scale standard 200 *mm* CMUs. Figure 3.4 shows the nominal dimensions of the CMUs used for the infill and boundary frame. The boundary frame cross-sections (including the top beam and

columns) of all specimens measured 190 x190 mm. As the custom-made boundary element masonry blocks of 390 x190 mm were used to construct the boundary frame (Figure 3.4) they were cut to desired geometry on site.

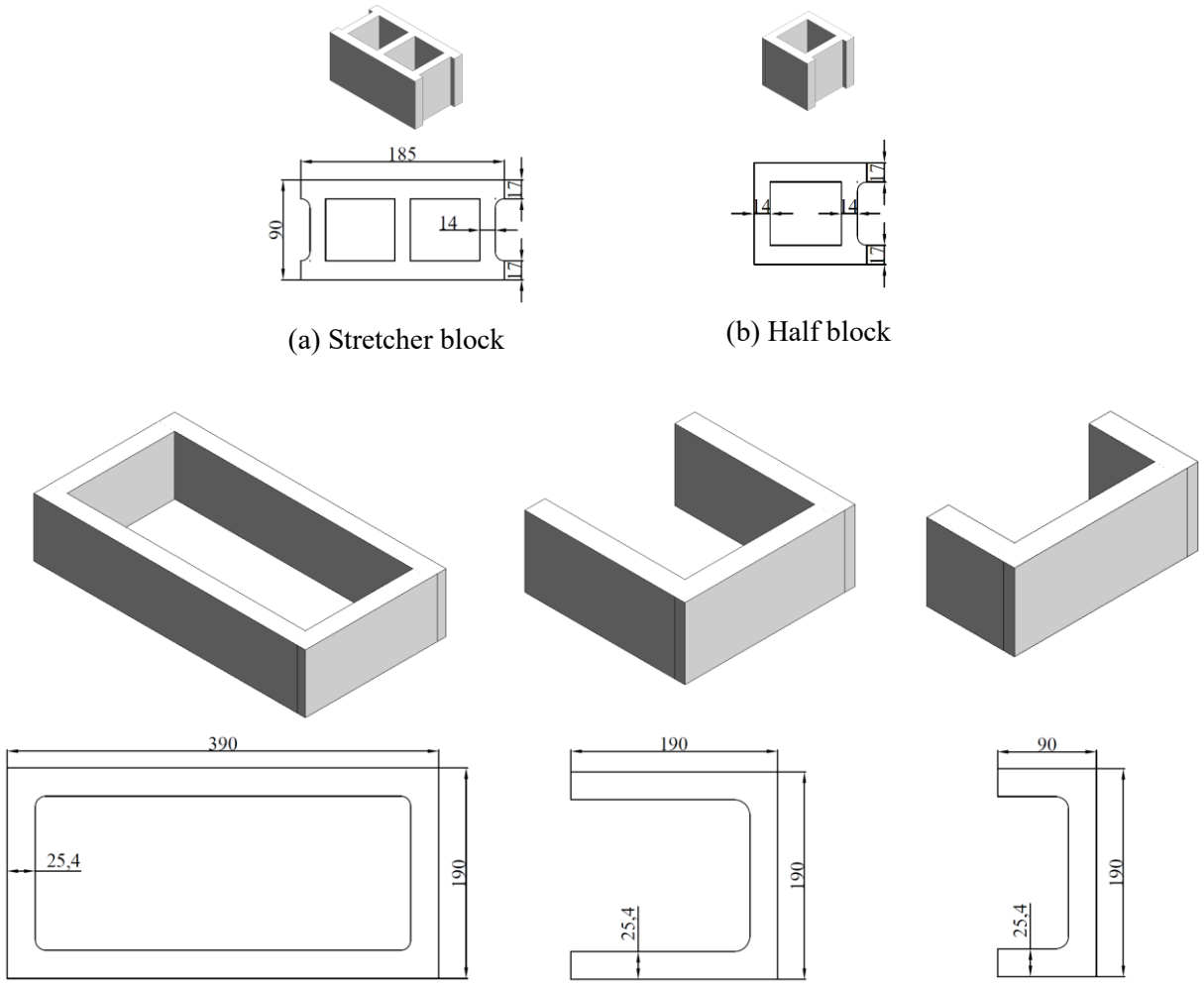


(a) Stretcher block (b) Half block

(c) Boundary block (d) Top beam block (e) Boundary half block

Figure 3.4 Geometry and dimensions of the CMUs used for infills and boundary frames (unit:mm)

The masonry infill and masonry boundary frame were constructed on top of a 250 x 250 mm reinforced concrete base beam. Figure 3.5 shows the reinforcing details for the boundary frame and the base beam using IF-LA-80 as an example. The masonry boundary frame for all specimens

was reinforced with four 10M deformed rebars and 10M stirrups, spaced at 100 mm centre-to-centre. The RC base beam was reinforced with four 15M deformed rebars and 10M stirrups spaced at 130 mm centre-to-centre. The regions of beam-column connection were reinforced with two additional 300 by 300 mm L-shaped 10M rebar at each top corner.

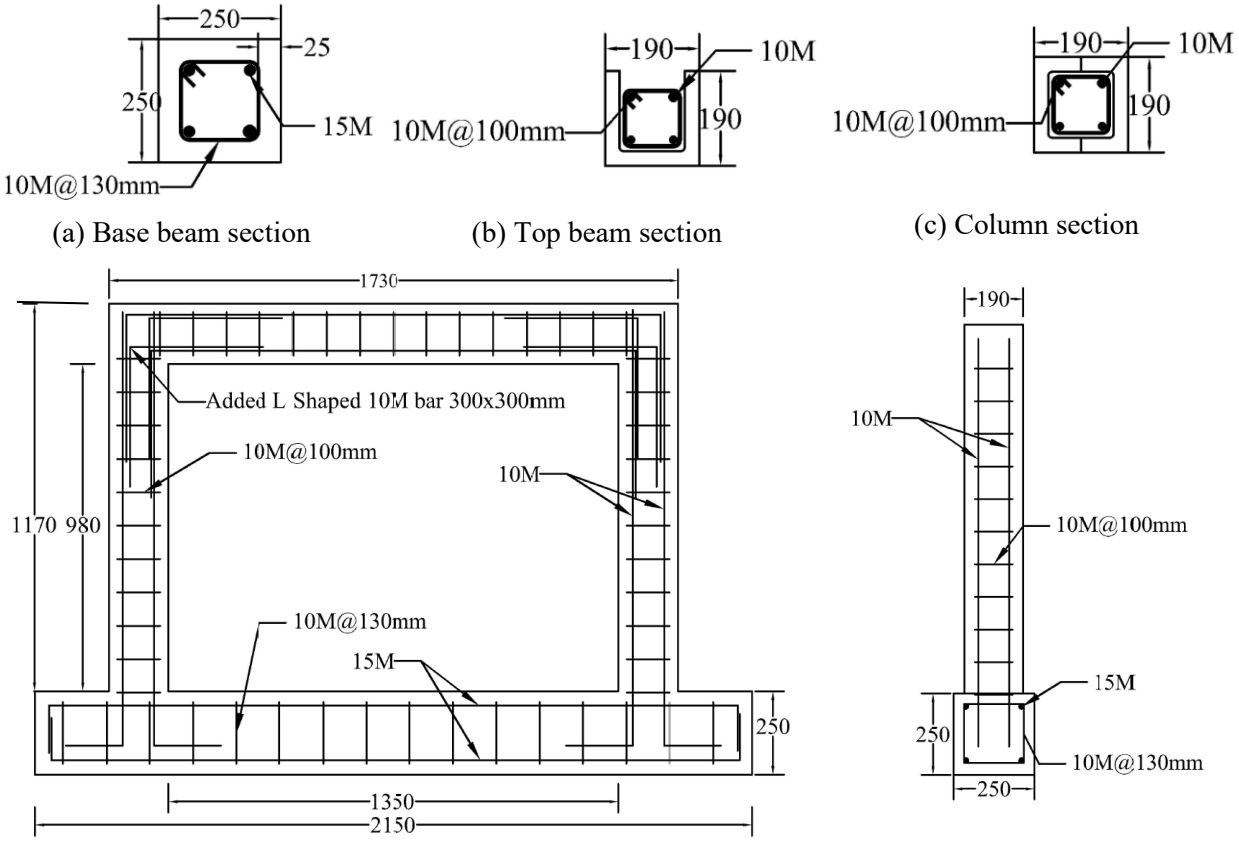


(a) Base beam section (b) Top beam section (c) Column section

(d) Frame reinforcement detail (e) Side view section

Figure 3.5 Boundary frame section reinforcement details (unit: mm)

The reinforcement scheme was maintained to be consistent with previous tests on infilled RC frames (Steeves 2017) and all-masonry infilled frames (Foroushani 2019) in the same research group for comparison purposes. In the case of the RC frame, the reinforcement detail including size, spacing, arrangement of longitudinal bars and stirrups were complied with requirements to

achieve ductility and avoid brittle shear failure in accordance with the Canadian concrete design code CSA A23-3 (2014). This reinforcing scheme was then consistently used for masonry frames.

## 3.3 CONSTRUCTION OF SPECIMENS

Construction of specimens began with the construction of the RC base beams. After the concrete curing of base beams for 28 days, the masonry boundary frame and masonry infill were constructed simultaneously by a certified mason to the industry standard of practice. The following sections describe the procedures performed for the construction of specimens.

### 3.3.1 Base beam construction

Construction of the RC base beam began with building the concrete formwork and forming steel rebar cage. As shown in Figure 3.6, plywood boards were first cut onsite to required geometry to form concrete formwork. The base beam reinforcement was formed as a steel cage and then placed into the formwork with a 40 mm cover. Lastly, the vertical rebars of the frame columns were tied into the base beam rebar cage before pouring the concrete.

Figure 3.6 Construction of base beam concrete formwork and rebar cage

The ready-mix concrete with a maximum aggregate size of 12 mm and a specified compressive strength of 25 MPa was used for the concrete base beam construction. All six base beams were poured on October 24, 2019. After casting each base beam, concrete was adequately vibrated to minimize potential air pockets and voids (Figure 3.7 (a)). Then the surface was smoothed using concrete trowels (Figure 3.7 (b)). Slump test was also conducted at each pour in accordance with ASTM C143/143M (2015) Standard Test Method for Slump of Hydraulic-Cement Concrete (Figure 3.8 (a)). The results showed an average of 156 mm falling height which satisfied the required 150 mm based on the standard. During concrete pouring, six 100 by 200 mm and three 150 by 300 mm concrete cylinders were also constructed as part of the auxiliary test in accordance with ASTM C39/C39M (2016) (Figure 3.8 (b)).

(a) Concrete vibration

(b) Smoothing concrete surface

Figure 3.7 Concrete casting of RC base beams

(a) (b)

Figure 3.8 In-Situ slump test and pouring cylinders

The base beams were moist cured under burlaps within the formwork for 48 hours before demolding. This was followed by moist curing for another 28 days and then air curing until the day of the test (Figure 3.9).

Figure 3.9 Air curing of RC base beams

### 3.3.2 Construction of masonry frame and infill

Before masonry construction, the column vertical rebars were tied with stirrups, and reinforcement cages for top beams were made (Figure 3.10 and Figure 3.11). The masonry frame and infill for all specimens were constructed between December 16 and December 19, 2019 by a certified mason.

Figure 3.10 Tying stirrups on the column vertical rebars

Figure 3.11 Top beam rebar cage fabrication

The masonry columns were constructed first which was followed by the masonry infill. The masonry top beam was completed last to tie the system together. For each course, the mortar was applied only on the face shell of blocks for both the bed joints and the head joints (Figure 3.12). To ensure the levelness and plumbness of the wall, each course was checked using a level and plumb before continuing to the next course. The U-shape blocks used to form the top beam were placed above the last infill course (Figure 3.13(a)). The reinforcement steel cage was carefully placed into the course with vertical rebars inserted into the cavity of columns (Figure 3.13 (b)). The cavities of both columns and beam were completely grouted and sufficiently vibrated to ensure that the concrete flowed to the bottom of the columns and also to remove air pockets (Figure 3.13 (c)). After grouting the frame, the whole specimen was wrapped with plastic sheets and kept moist-cured for 28 days followed by air-curing until the day of testing (Figure 3.13 (d)).

Figure 3.12 Applying mortar to bed joint and head joint

(a) U-shape blocks for top beam

(b) Positioning top beam cage

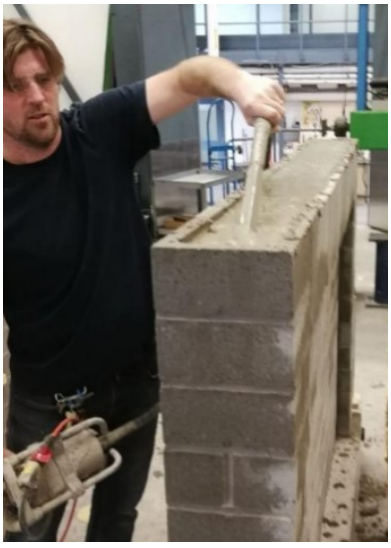

(c) Grout vibration

(d) Moist curing

Figure 3.13 Construction of top beam

### 3.3.3 Construction of specimens IF-W-TG-C and IF-W-SG-C

Specimens IF-W-TG-C and IF-W-SG-C had a window opening and infill-to-frame gaps. A shoring system consisting of wooden planks was installed during construction and curing, as illustrated in Figure 3.14. In order to make the required gaps, plywood strips with thickness of 6 mm and 12 mm were used at the gap location during the construction and were removed afterwards. Also, to

facilitate cyclic loading, a threaded rod running the full length of the frame top beam was used and anchored as shown in Figure 3.15. The rod was positioned along the neutral axis of the beam so their effect to the frame in-plane resistance is negligible.

Figure 3.14 The shoring system to form a window opening

Figure 3.15 Threaded rod in the top beam

## 3.4 TEST SETUP

### 3.4.1 Lateral loading setup – Monotonic loading

The overall setup and details of loading application are shown in Figure 3.16 and Figure 3.17, respectively. A hydraulic actuator reacted against the column of an independent reaction frame was used to apply the monotonic lateral load. The load was monitored throughout the loading history using a load cell attached to the head of the actuator. To prevent masonry local crushing, a steel plate was mounted between the load cell and the frame top beam to distribute load uniformly.

Figure 3.16 Lateral loading setup

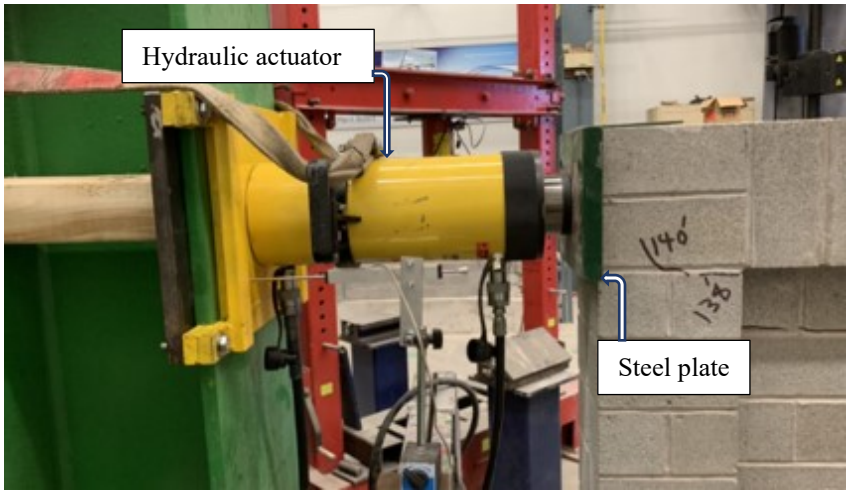


Figure 3.17 Actuator to top beam detail

All specimens had the same setup for providing the fixity of the frame base beam to the strong floor. The base beam of the frame was clamped down to the floor with two W steel beams through 40 mm threaded rods (Figure 3.18 (a)). To avoid any potential sliding the base beam was further braced using a hydraulic jack on each end against the column of the reaction frame, as shown in Figure 3.18 (b) and (c).


(a) Beam to floor clamping connection

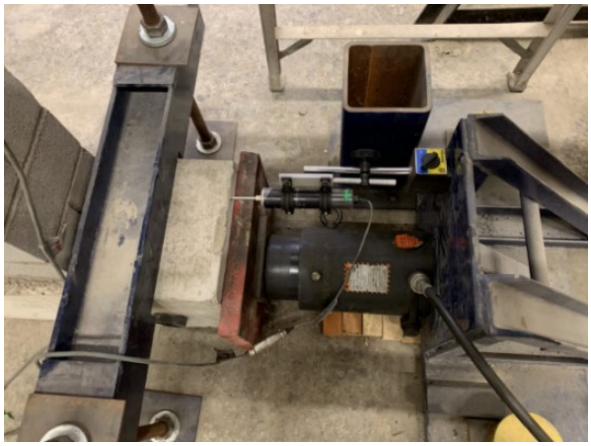

(b) Top view of hydraulic actuator

(c) Side view of hydraulic actuator

Figure 3.18 Lateral brace support for the base beam

### 3.4.2 Lateral loading setup – Cyclic loading

A hydraulic actuator with a capacity of 100 kN was used to apply the quasi-static cyclic loading. The actuator was housed in an independent frame which was then attached to the column of a reaction frame as shown in Figure 3.19. The threaded rod running the full length of the frame top beam was used to transfer the pulling and pushing actions on the specimen. The actuator head was connected to the specimen through a steel plate, one side of which received the threaded rod through threaded bolt hole whereas the other side was connected to the actuator head through two threaded rod as depicted in Figure 3.20.

Figure 3.19 Cyclic loading setup

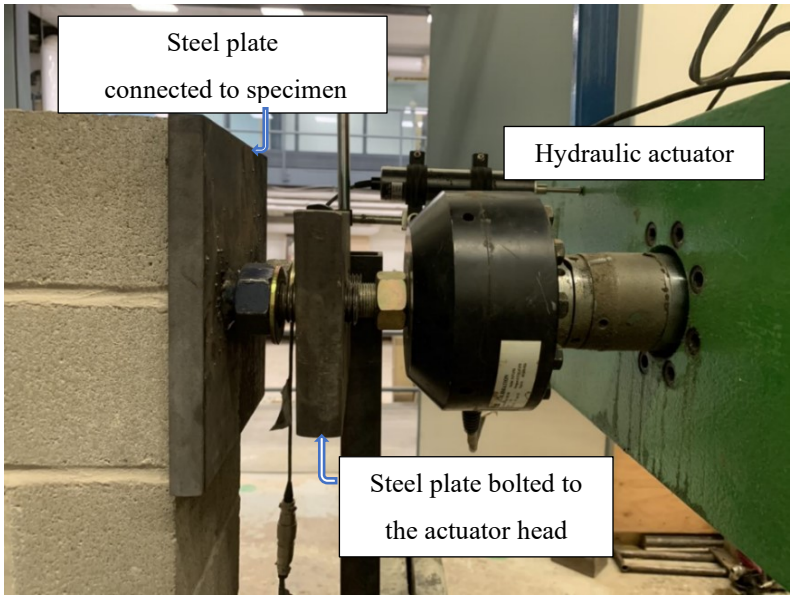

Figure 3.20 Cyclic loading application detail

The cyclic loading protocol in this study adopted ATC-24 (Applied Technology Council-24 1991) loading protocol specified for cyclic testing of steel structures. Although specified for steel structures, ATC-24 has been used for the loading instructions of concrete masonry infill RC frames in several experimental programs (Mehrabi et al. 1994, Mosalam 1996, El-Dakhakhni 2002, Al-Nimry 2014). The ATC loading protocol references yield deformation $\Delta_y$ for each set of cycles. As shown in Figure 3.21 Figure 3.21, testing begins with three elastic cycles each at $0.5\Delta_y$, and $0.75\Delta_y$ levels. This is followed by three cycles each at $\Delta_y$, $2\Delta_y$, and $3\Delta_y$ levels to induce yielding and failure. If failure of specimen has not happened by $3\Delta_y$ cycles, the loading would continue with sets of two cycles beginning at $4\Delta_y$ and increase by an increment of $\Delta_y$ until failure. The $\Delta_y$ used in the experimental study by Steeves (2017) on masonry infilled RC frames was 7 mm and this value was also adopted in this study given similar geometry and dimensions used for the two systems.

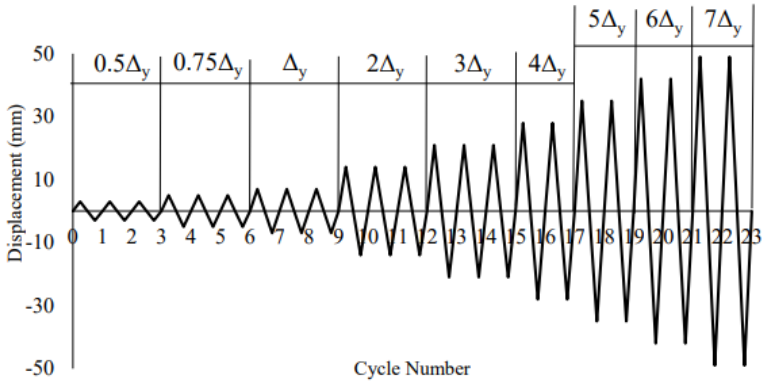


Figure 3.21 Loading protocol for the quasi-static loading

### 3.4.3 Vertical loading setup

Figure 3.22 shows the overall vertical load setup. The vertical load was applied through the frame columns. To achieve this loading scheme, a hydraulic jack was reacted between the crosshead of the independent frame and a steel spreader beam. The spreader beam was rested on a roller assembly at the top of the columns. The roller assembly can accommodate rotations of the steel beam and relative lateral movement between the spreader beam and the masonry specimen when the in-plane loading was applied. Figure 3.23 shows a close-up of the vertical loading arrangement.

Figure 3.22 Combined vertical and lateral loading setup

### 3.4.4 Displacement transducer arrangement

A total of six linear variable differential transformers (LVDTs) were used to measure deflections for each specimen. Two LVDTs were used to monitor the lateral displacements of the specimen, where LVDT 1 and 2 were positioned to measure the top frame beam and base beam lateral displacements, respectively. Two LVDTs were used to measure potential out-of-plane displacements of the specimen where LVDTs 3 and 4 were placed at the mid-point of the top frame beam and the center of infill, respectively. LVDT 5 was positioned on top of the base beam at the loading side of the specimen to monitor the potential uplift of the specimen. To measure any potential lateral movement of the independent steel frame in which the specimens were tested, the LVDT 6 was installed on steel frame column. Figure 3.24 illustrate the schematic of LVDTs arrangement.

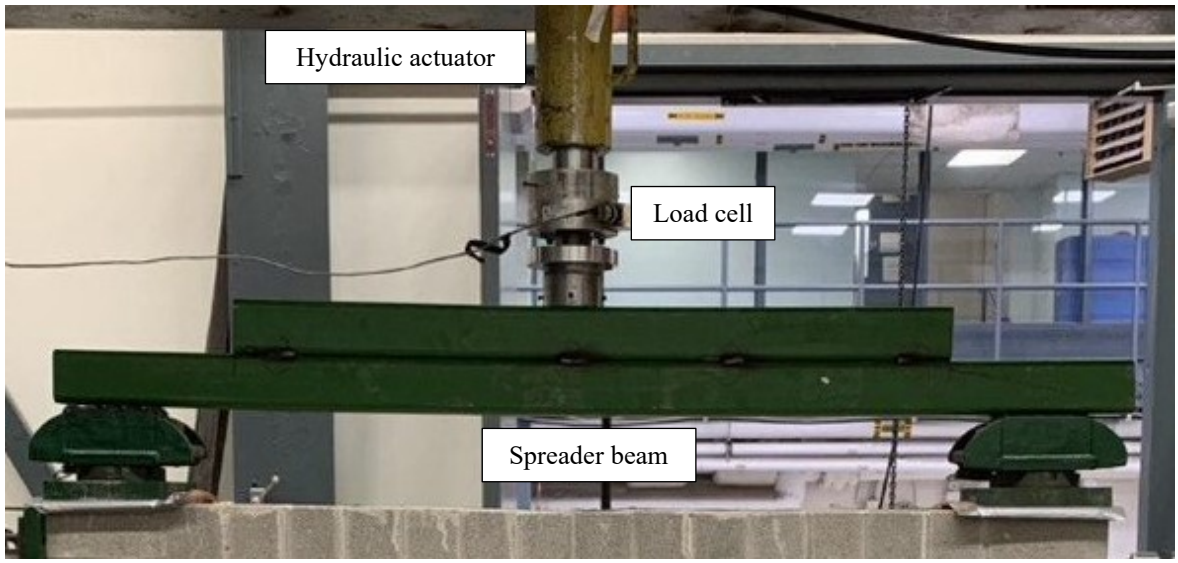


(a)

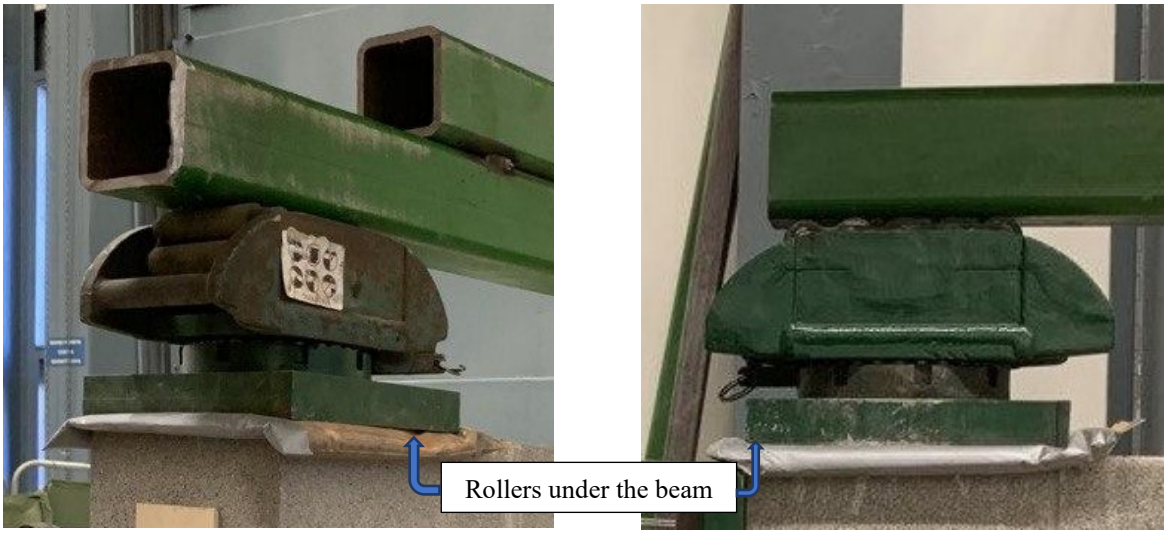


(b) (c)

Figure 3.23 Vertical load arrangement detail

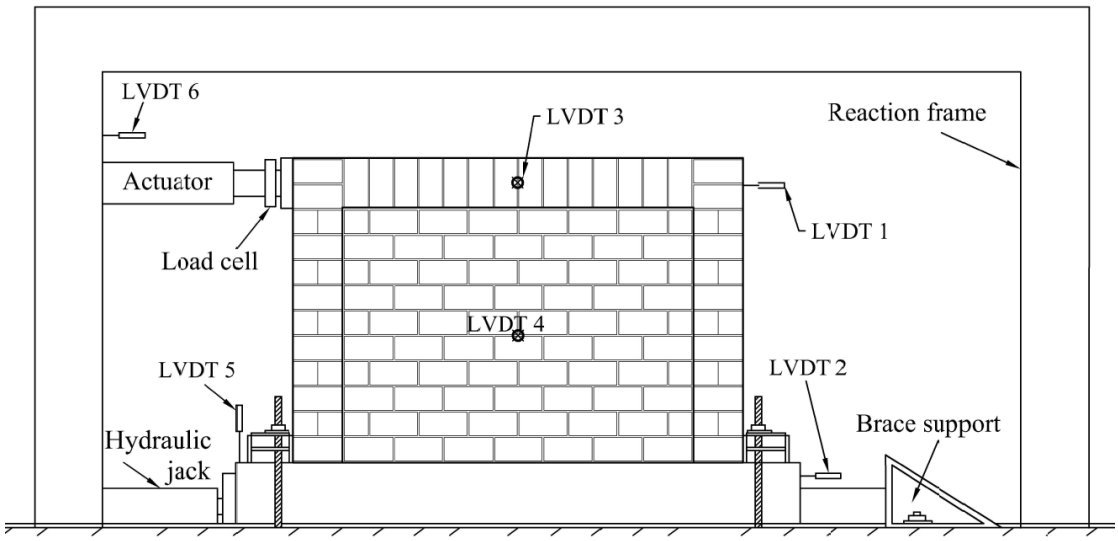


Figure 3.24 Schematic of LVDTs arrangement

### 3.4.5 Testing procedure

The specimens were first placed into the testing position and aligned properly in both in-plane and out-of-plane directions. Prior to each test, the load cell(s) and displacement transducers were checked to ensure that they worked properly and zeroed at the beginning of the test. For monotonic test, the in-plane lateral loading rate was set at 1 mm per minute. For cyclic loading test, the loading protocol was followed, and the loading rate was set at 3 mm per minute. The load cell and all LVDTs were adjusted to record data at a 0.1 second interval using an electronic data acquisition system. For specimens IF-LA80 and IF-LA160 under combined lateral and vertical loading, the vertical load was first applied to the specified level and held while the monotonic lateral load was applied in the manner as described above. For each test, the cracking pattern, ultimate load, and failure mode were recorded and noted throughout the testing history.

# CHAPTER 4 EXPERIMENTAL RESULTS

## 4.1 INTRODUCTION

This chapter presents results of the masonry infilled frame specimens in terms of lateral strength, stiffness, ductility, load vs. displacement response and failure mode. The effects of axial load, infill aspect ratio, and interfacial gap are also discussed as appropriate. A detailed description of results of auxiliary tests on masonry components is included in Appendix B.

## 4.2 INFILLED FRAME SPECIMENS

### 4.2.1 Failure mode

The observed failure modes for all specimens are summarised in Table 4.1 where the failure initiation mode, and final failure mode for each specimen are provided. Note that the pulling action is labelled as (+) whereas pushing action is labelled as (-). The experimentally obtained masonry compressive strengths, $f'_m$, for the infill and the masonry frame for each specimen are also included in the table.

Table 4.1 Summary of failure modes for specimens

| Specimen ID | $f'_{m-infill}$ (MPa) | $f'_{m-bound.frame}$ (MPa) | Failure initiation mode | Final failure mode (+) | Final failure mode (-) |
|---|---|---|---|---|---|
| IF-LA-80 | 16.8 | 10.8 | DC | - | DC |
| IF-LA-160 | 14.1 | 10.8 | DC | - | DC |
| IF-AS-0.5 | 16.0 | 14.8 | DC | - | DC |
| IF-AS-1.3 | 16.8 | 14.8 | DC | - | DC |
| IF-W-TG-C | 16.8 | 18.4 | DC | DC | DC |
| IF-W-SG-C | 16.8 | 18.4 | DC | CC | CC |

For all specimens, diagonal tension cracking (DC) was observed to be the failure initiation mode. This is in line with masonry infilled RC frames. As for the final failure, except for specimen IF-W-SG-C (cyclic loading) which failed by corner crushing in both directions, diagonal tension cracking (DC) remained to be the mode for most specimens. This observation is different from masonry infilled RC frames where corner crushing is widely recognized as the predominantly final failure mode.

### 4.2.2 General behaviour – lateral load vs. displacement response

A typical lateral load vs. displacement response curve is illustrated in Figure 4.1 using specimen IF-AS-0.5 as an example. Several performance indicators used in the later discussion are defined using the curve. The initial stiffness, $K_{ini}$, is defined as the slope of the initial linear portion of the response curve, and the cracking stiffness, $K_{cr}$, is defined as the slope of the line connecting the origin and the load where the first visible crack occurred ($P_{cr}, \Delta_{cr}$). The response curve began to show non-linearity before the first visible crack indicating some initial cracking formed in either masonry infill or frame which may not be visible. The first visible crack was commonly accompanied by a noticeable load drop on the curve with an immediate thereafter load recovering and was also corroborated by the experimental observation. The ultimate lateral load, $P_{ult}$, is defined as the maximum lateral load attained by the specimen and the corresponding lateral displacement is defined as $\Delta_{ult}$. $P_{fail}$ indicates the final failure load when either the lateral load dropped more than 20% of the ultimate load or the test was discontinued, and the corresponding lateral displacement is labelled as $\Delta_{fail}$.

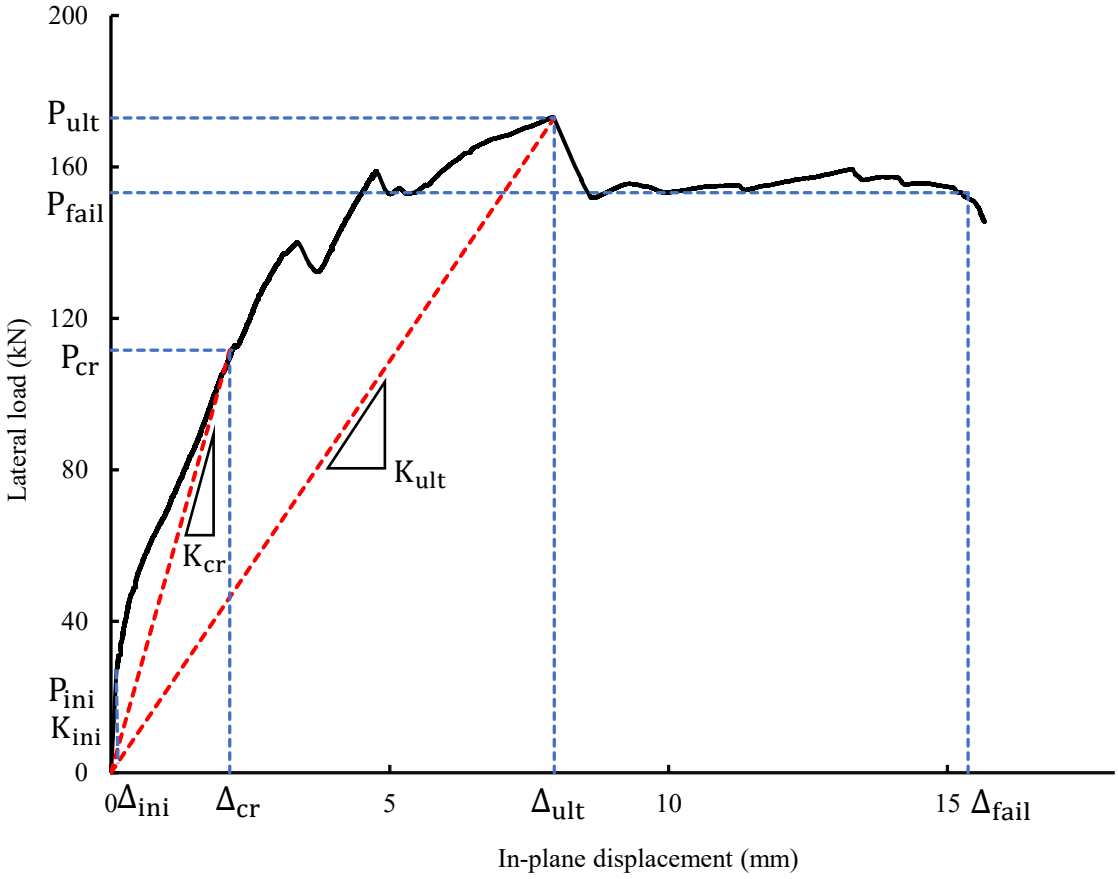


Figure 4.1 Typical lateral load vs. in-plane displacement curve of specimens (IF-AS-0.5)

### 4.2.3 Specimen IF-LA-80

Figure 4.2 illustrates the lateral load vs. in-plane displacement response and Figure 4.3 shows the failure mode of this specimen where blue line indicates the first significant crack and red lines indicate the development of cracking. Figure 4.2

Figure 4.2 shows that up to 30.7 kN, the response is more or less linear, after which point, the outset of non-linearity began to develop, although no visible cracks were observed experimentally in the specimen. It is believed that small cracks might have occurred in the specimen to cause non-linearity, but their occurrence was difficult to detect visually. When the load increased to 147 kN, a noticeable load drop is seen in Figure 4.2 which coincided with the first significant crack formed

in the central region of the specimen. As the load continued to increase, the cracks progressed and developed in the diagonal direction connecting the loaded corners (marked in red). The response curve showed a series of load drops accompanied by immediate load increases thereafter, indicating that the specimen finds alternative paths to transfer load as cracking occurred. At around 164 kN, the cracks widened and progressed into the bottom corner of the right column suddenly, causing face shell spalling, at which point, the specimen reached the ultimate load. The response showed a relatively ductile falling branch as load dropped and the test discontinued. As can be seen in Figure 4.3, final failure mode for the specimen was identified by diagonal cracking.

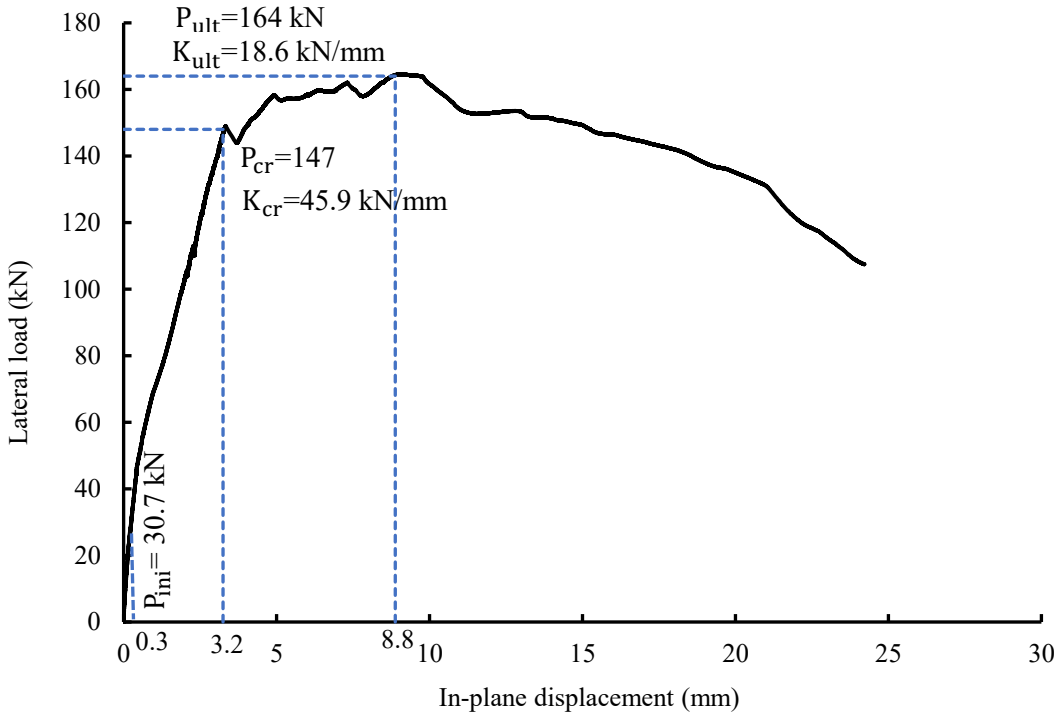


Figure 4.2 Lateral load vs. in-plane displacement curve of IF-LA-80

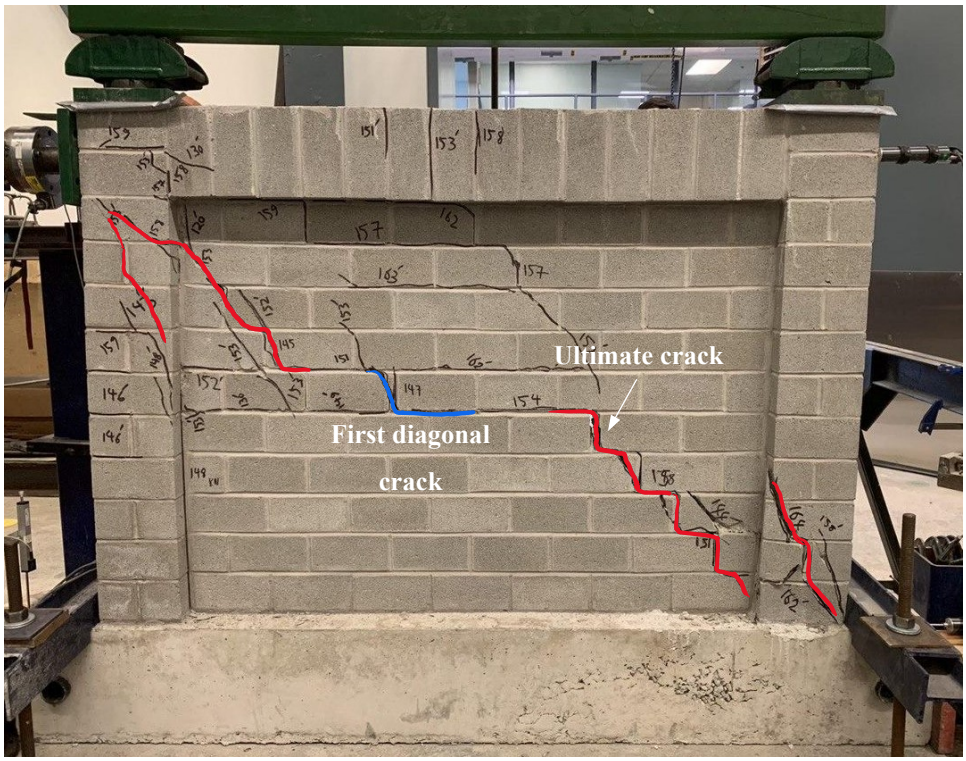

Figure 4.3 Final failure pattern of IF-LA-80

### 4.2.4 Specimen IF-LA-160

The lateral load vs. in-plane displacement responses of the specimen IF-LA-160 is illustrated in Figure 4.4 and Figure 4.5 shows the final failure mode. The response curve showed an initial linear stage up to a load of 41 kN. After the initial stage, the curve began the onset of non-linearity. Similar to specimen IF-LA-80, no visible cracks were observed on the specimen while this non-linearity developed. The first significant crack occurred around 130 kN and as the load increased, more cracks began to form and develop, again, in the diagonal direction in the infill. Cracks also appeared at the loaded corner (left corner) of the masonry frame and along the length of the frame beam. At the load of around 164 kN (the ultimate load of IF-LA-80), the specimen continued to resist load without losing too much stiffness. Similar to specimen IF-LA-80 when the specimen

reached a load at 293.8 kN, a sudden significant diagonal crack appeared and connected through the entire width of the specimen and the top corner of the left column (where the load was applied).

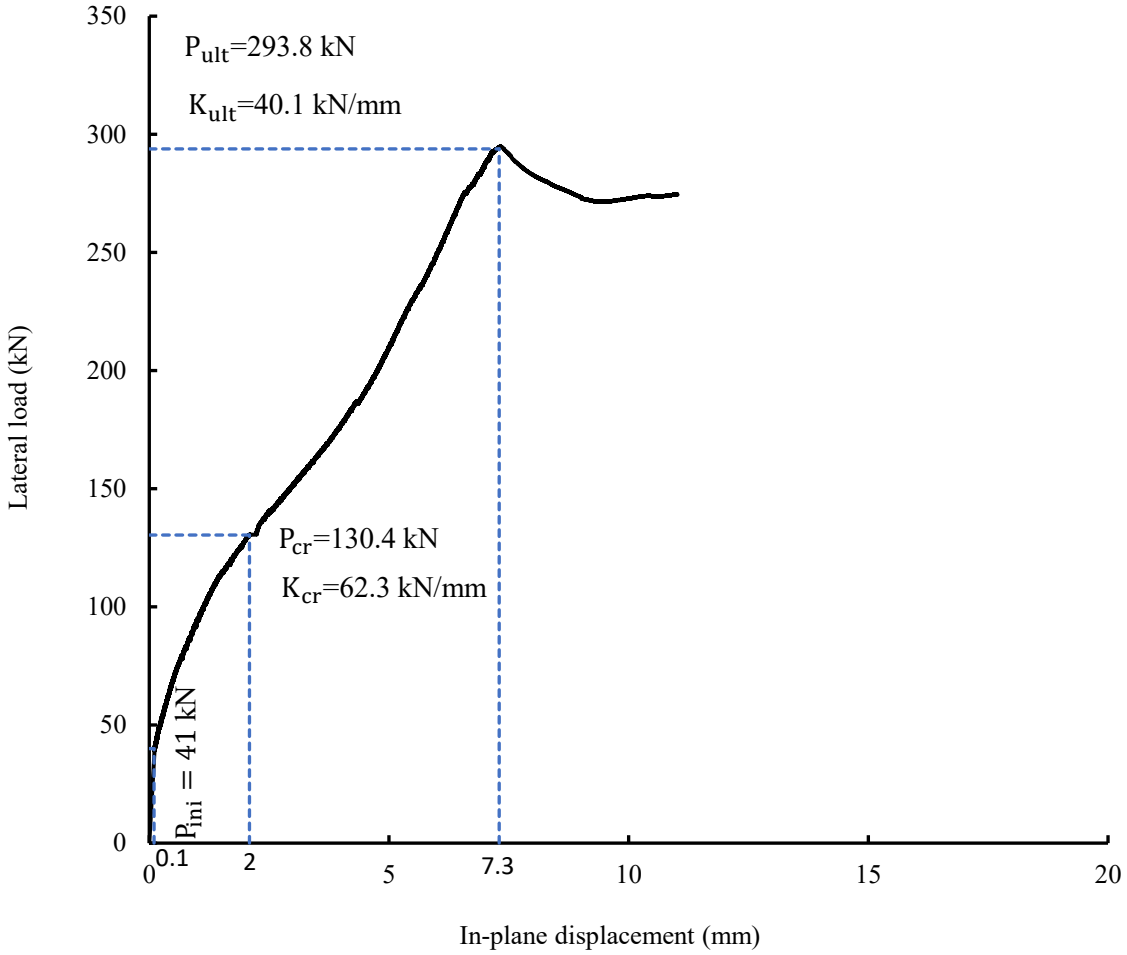


Figure 4.4 Lateral load vs. in-plane displacement curve of IF-LA-160

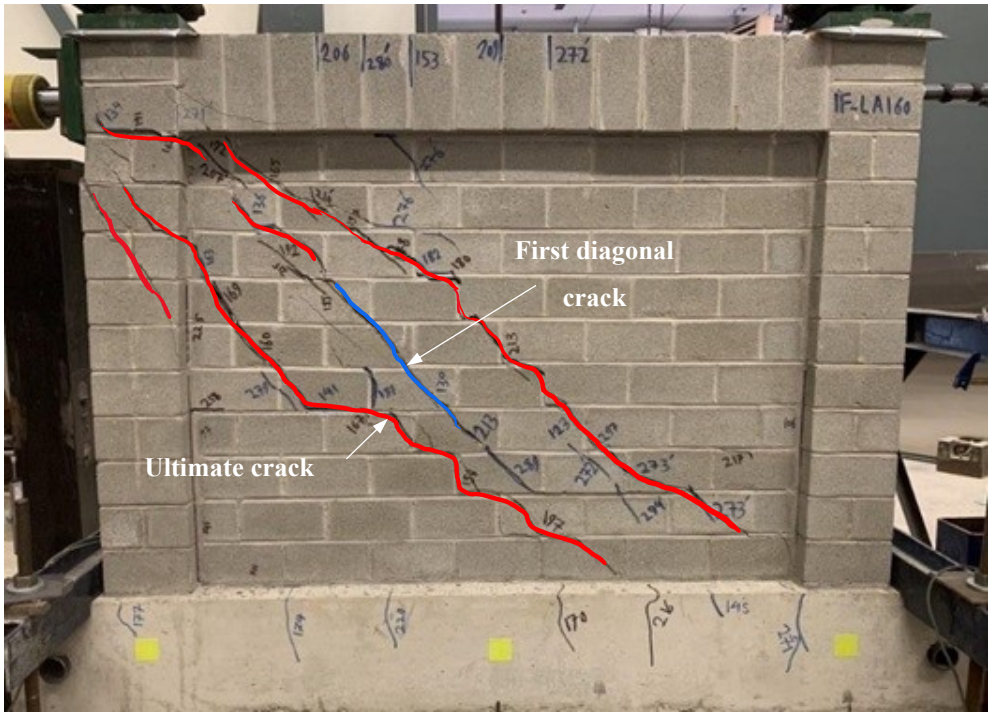

Figure 4.5 Final failure pattern of IF-LA-160

### 4.2.5 Comparison of specimens IF-LA-80 and IF-LA-160

The effect of axial load is shown in Figure 4.6 where the lateral load vs. in-plane displacement curves of specimens IF-LA-80 and IF-LA-160 are compared, and in Table 4.2 where the performance indicator values are summarized. It can be seen that a higher axial load resulted in higher stiffness and strength but lower ductility of the infilled specimen. More specifically, as the applied axial load doubled, specimen IF-LA-160 showed a 35% greater cracking stiffness than specimen IF-LA-80 and more than doubled the latter's ultimate stiffness. In the case of strength, the ultimate load increased by about 80%. It is believed that stiffer frame resulted in greater contact area and subsequently greater struth width causing more strength in IF-LA-160specimen. Specimen IF-LA-160 reached the ultimate load at a smaller displacement (7.3 mm vs. 8.8 mm). The post-ultimate behaviour of IF-LA-160 showed a more brittle failure with a significant load drop immediately following the ultimate load.

Figure 4.6 also shows that the response curve of specimen IF-LA-160 does not appear to have a pronounced "plateau" stage, rather, it continues to increase after cracking at a similar stiffness until reaching the ultimate.

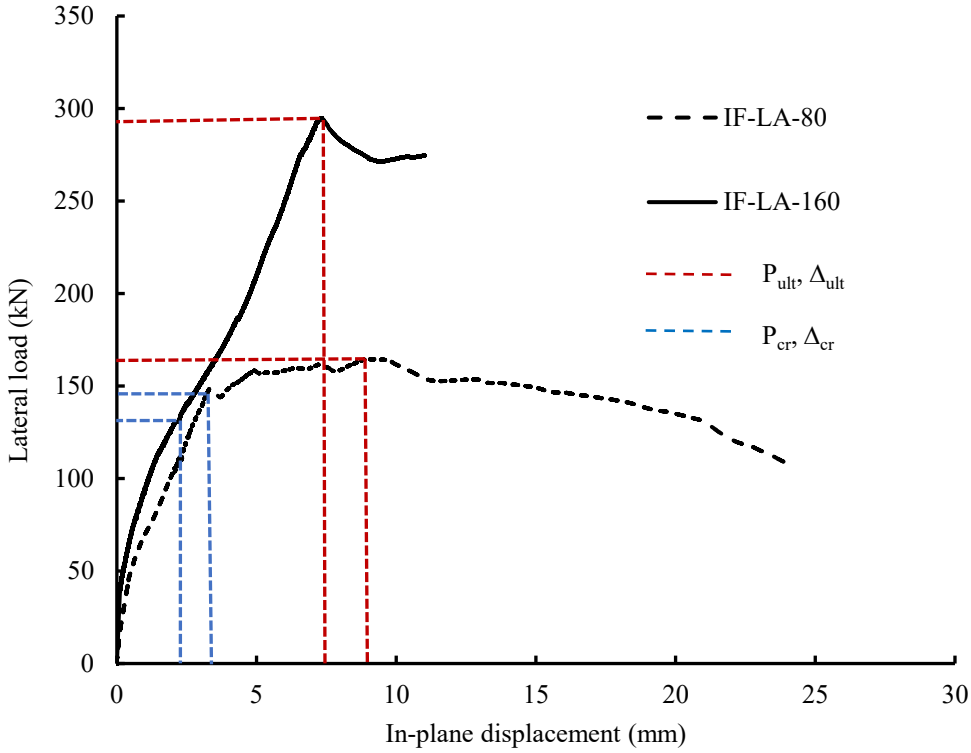


Figure 4.6 Lateral load vs. in-plane displacement curve for vertical load study

Table 4.2 Test result comparison of IF-LA80 and IF-LA160

| Specimen ID | $k_{in}$ (kN/mm) | $k_{cr}$ (kN/mm) | $k_{ult}$ (kN/mm) | $P_{cr}$ (kN) | $\Delta_{cr}$ $(mm)$ | $P_{ult}$ (kN) | $\Delta_{ult}$ $(mm)$ |
|---|---|---|---|---|---|---|---|
| IF-LA-80 | 102.4 | 45.9 | 18.6 | 147.0 | 3.2 | 164.0 | 8.8 |
| IF-LA-160 | 410.0 | 62.3 | 40.1 | 130.4 | 2.0 | 293.8 | 7.3 |

As shown in Figure 4.3 and Figure 4.5, the failure modes between the two specimens are similar, all sustaining severe diagonal cracking and boundary column cracking. However, diagonal cracking in specimen IF-LA-160 appears to be more extensive.

The uplift recorded at the base beam of specimen IF-LA-160 at ultimate was about 4 mm, which is about twice that recorded for specimen IF-LA-80. Relative to the dimensions of the specimens, a 4 mm uplift can be considered negligible. Similarly, out-of-plane displacements of both specimens were in the order of less than 1 mm and thus deemed negligible.

### 4.2.6 Specimen IF-AS-0.5

Figure 4.7 shows the lateral load vs. in-plane displacement response and Figure 4.8 shows the failure mode of this specimen. The linear stage of this specimens was relatively short only up to 28 kN. The first significant crack occurred at 139 kN in the upper left region of the infill, although small hairline cracks were observed over the specimen starting around 60 kN which may contribute to the non-linearity of the curve between then and 139 kN. Between the first crack and the ultimate load of 173 kN, the response curve exhibited the typical “plateau” behaviour indicating that the cracks were mostly developed and progressed during this stage. After reaching the ultimate load of 173 kN, a notable load drop was observed. As shown in Figure 4.8, at ultimate, diagonal cracks developed and widened and also extended into the frame columns at two loaded corners which caused the loss of specimen’s ability to sustain more load. But no evident corner crushing was observed.

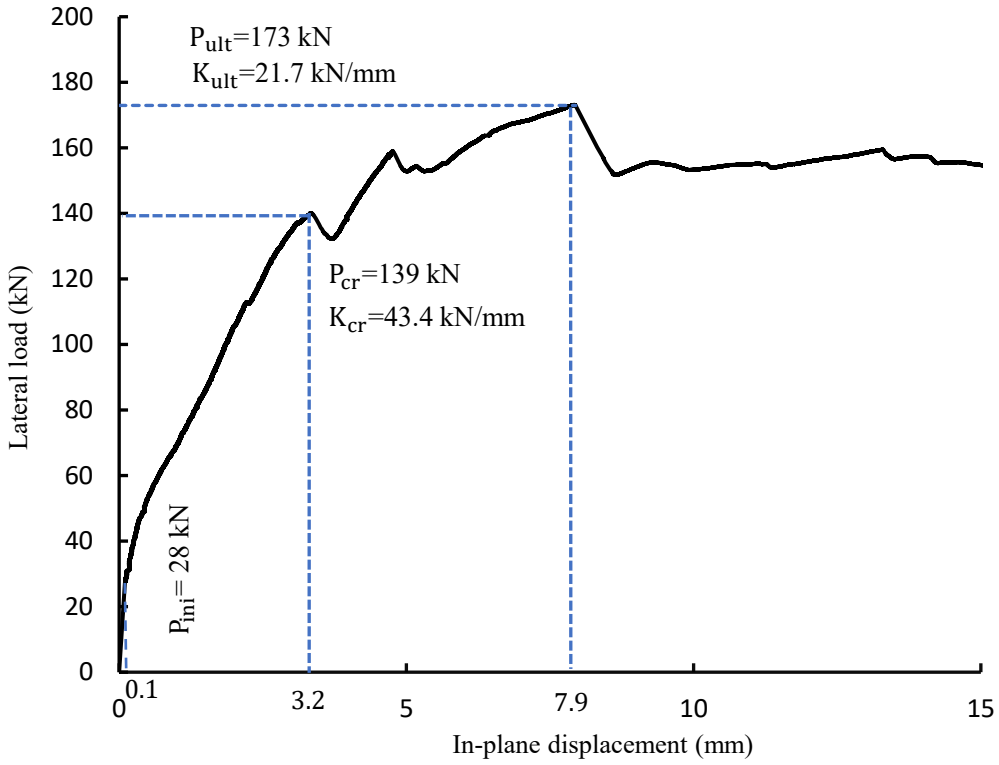


Figure 4.7 Lateral load vs. in-plane displacement curve of IF-AS-0.5

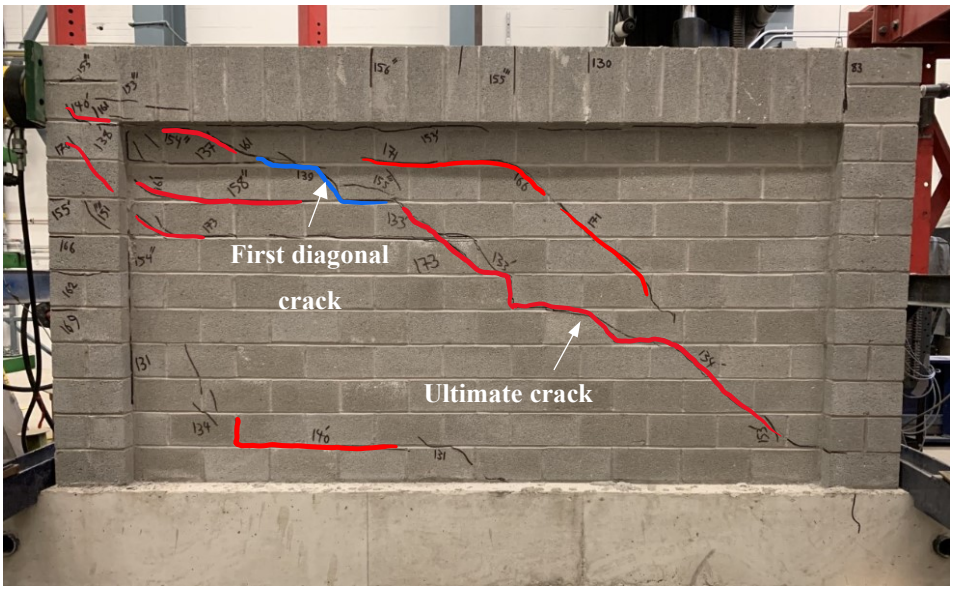


Figure 4.8 Final failure pattern of IF-AS-0.5

### 4.2.7 Specimen IF-AS-1.3

Figure 4.9 shows the lateral load vs. in-plane displacement response and Figure 4.10 shows the failure mode of this specimen. The response of this specimen showed non-linearity almost immediately after loading, at 13 kN. The overall response is ductile and smooth and did not exhibit the typical "zig-zag" behaviour of previous specimens. From the first noticeable crack formed at 127 kN to the ultimate load of 165 kN, there was a reduction in stiffness but the difference from previous specimens is that this reduction was continuous. At ultimate, the central diagonal cracks suddenly widened and developed over the specimen as shown in Figure 4.10. This behaviour is believed to be attributed to a more pronounced frame flexural behaviour due to the greater height of the specimen in combination with the frame-to-infill shear behaviour. The former resulted in a more ductile behaviour whereas latter still resulted in diagonal cracking.

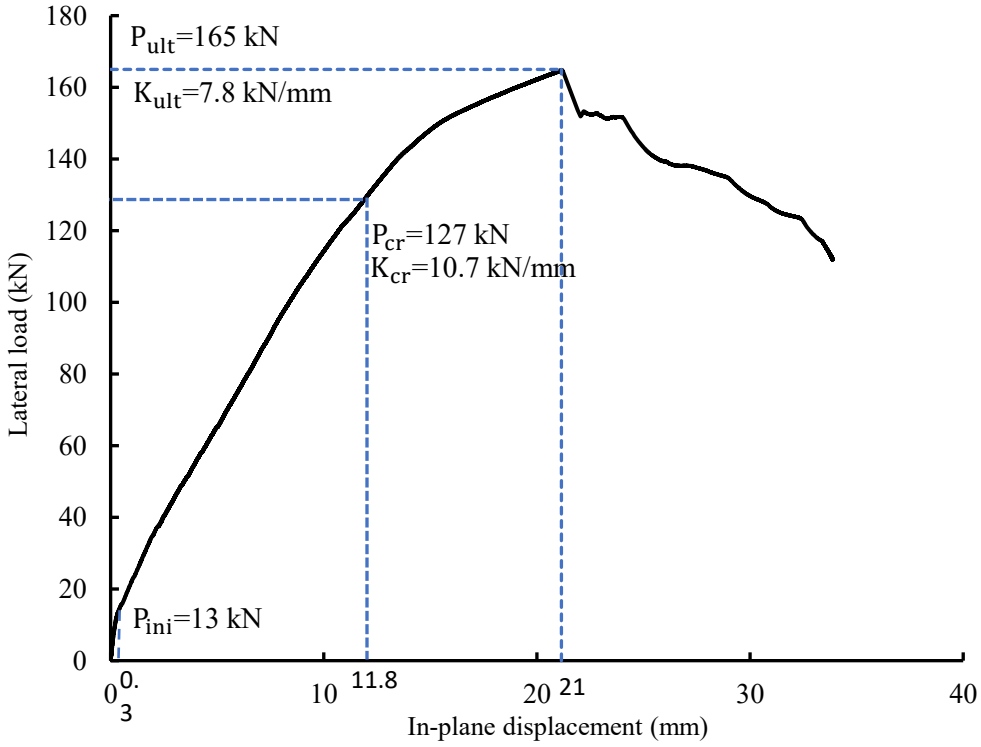


Figure 4.9 Lateral load vs. in-plane displacement curve of IF-AS-1.3

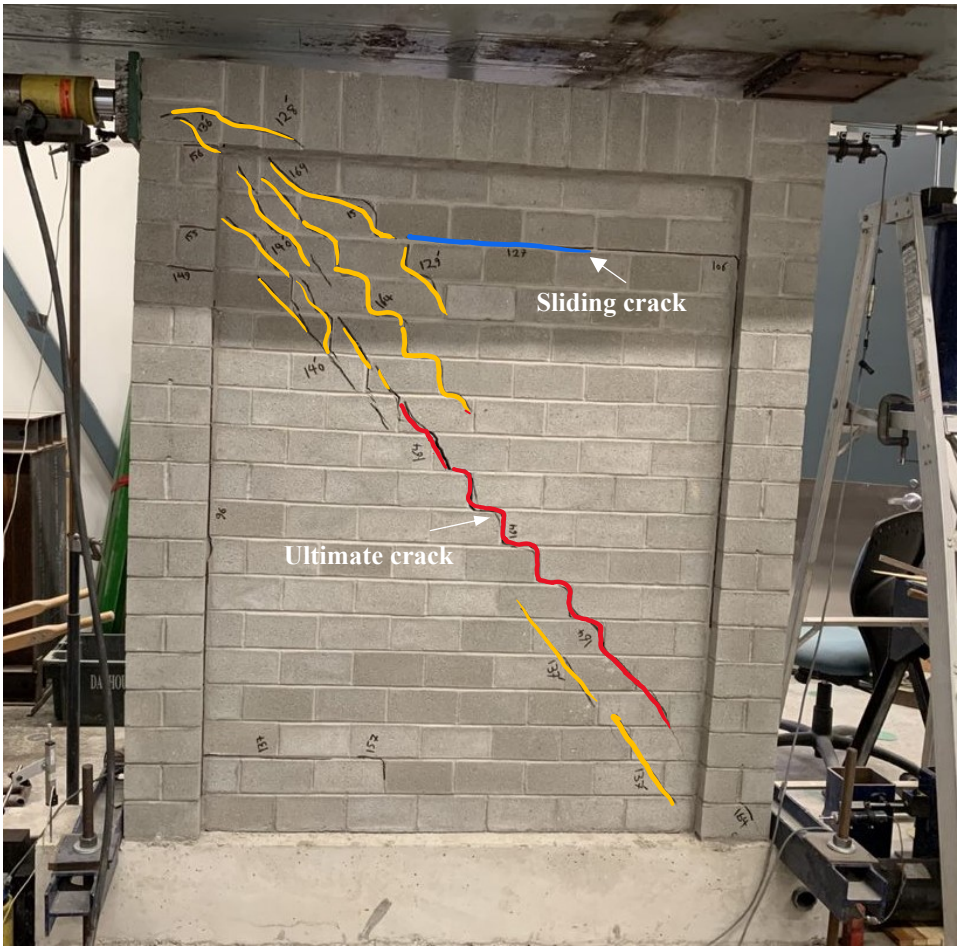

Figure 4.10 Final failure pattern of IF-AS-1.3

### 4.2.8 Comparison of specimens IF-AS-0.5 and IF-AS-1.3

The effect of infill aspect ratio is shown in Figure 4.11 where the lateral load vs displacement curves of specimens IF-AS-0.5 and IF-AS-1.3 are plotted and all performance indicator values are compared in Table 4.3. It is evident that as the aspect ratio increased, stiffness decreased, and ductility increased. Specifically, the cracking stiffness of specimen IF-AS-1.3 was about ¼ that of specimen IF-AS-0.5 and IF-AS-1.3 reached the ultimate load at a greater displacement (21 mm vs. 7.9 mm). However, two specimens attained similar ultimate loads with specimen IF-AS-0.5 showing a less than 5% higher value. Noting that both specimen failed by diagonal cracking which indicates the formation of diagonal strut, the geometry and dimension of both specimens would

yield a similar length of the diagonal strut which may provide an explanation on the similar ultimate loads of two specimens. Further, the aspect ratio appears to exert more influence on the behaviour in terms of stiffness and ductility but has less effect on the ultimate load, provided that the failure is governed by diagonal cracking. However, more aspect ratios need to be studied to support this observation. As expected, the uplift of specimen IF-AS-1.3 reached a higher value than specimen IF-AS-0.5 (12 mm vs. 3 mm). The effect of the uplift on the lateral displacement was accounted for in the calculation of the values presented in the figure and table. A higher uplift value confirmed that more moment was generated in specimen IF-AS-1.3. The out-of-plane displacements were similar as previous specimens and deemed negligible in both cases.

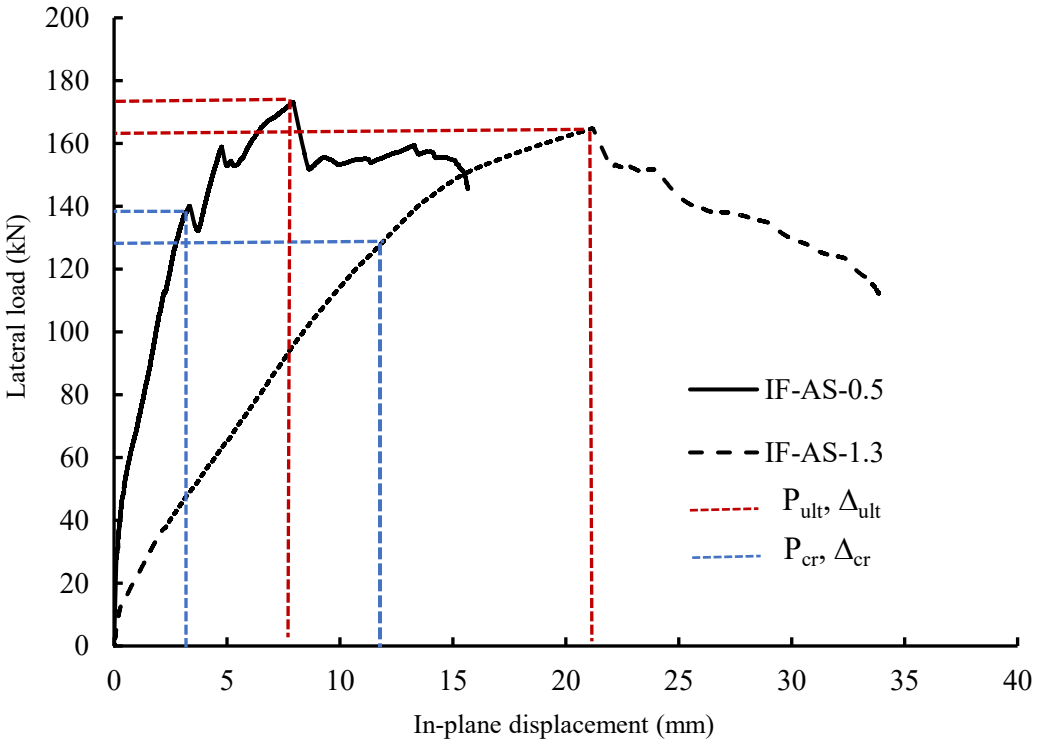


Figure 4.11 Lateral load vs. in-plane displacement curve for aspect ratio study

Table 4.3 Test result comparison of IF-AS-0.5 and IF-AS-1.3

| Specimen ID | $k_{in}$ (kN/mm) | $k_{cr}$ (kN/mm) | $k_{ult}$ (kN/mm) | $\Delta_{cr}$ $(mm)$ | $P_{cr}$ (kN) | $P_{ult}$ (kN) | $\Delta_{ult}$ $(mm)$ |
|---|---|---|---|---|---|---|---|
| IF-AS-0.5 | 280.0 | 43.4 | 21.7 | 3.2 | 139 | 173 | 7.9 |
| IF-AS-1.3 | 43.3 | 10.7 | 7.8 | 11.8 | 127 | 165 | 21.0 |

### 4.2.9 Specimen IF-W-TG-C

Figure 4.12 shows the failure pattern of this specimen. Cracks began to form around the opening along the diagonal direction of the infill at 2.9 mm in the pulling action of the 3.5 mm ($0.5\Delta_y$) cycle at a recorded load of 35 kN. In the pushing action, diagonal cracks formed at 1.4 mm of 3.5 mm ($0.5\Delta_y$) cycle at a recorded load of 24 kN. As displacement continued to increase for the next cycles, cracks developed and extended, connecting opening corners to infill corners (Figure 4.12). The ultimate load was reached during the pushing action of the 21.2 mm ($3\Delta_y$) cycle at a recorded load of 69.4 kN while in the pulling action, the ultimate load was reached at 62.3 kN with a displacement of 21.6 mm.

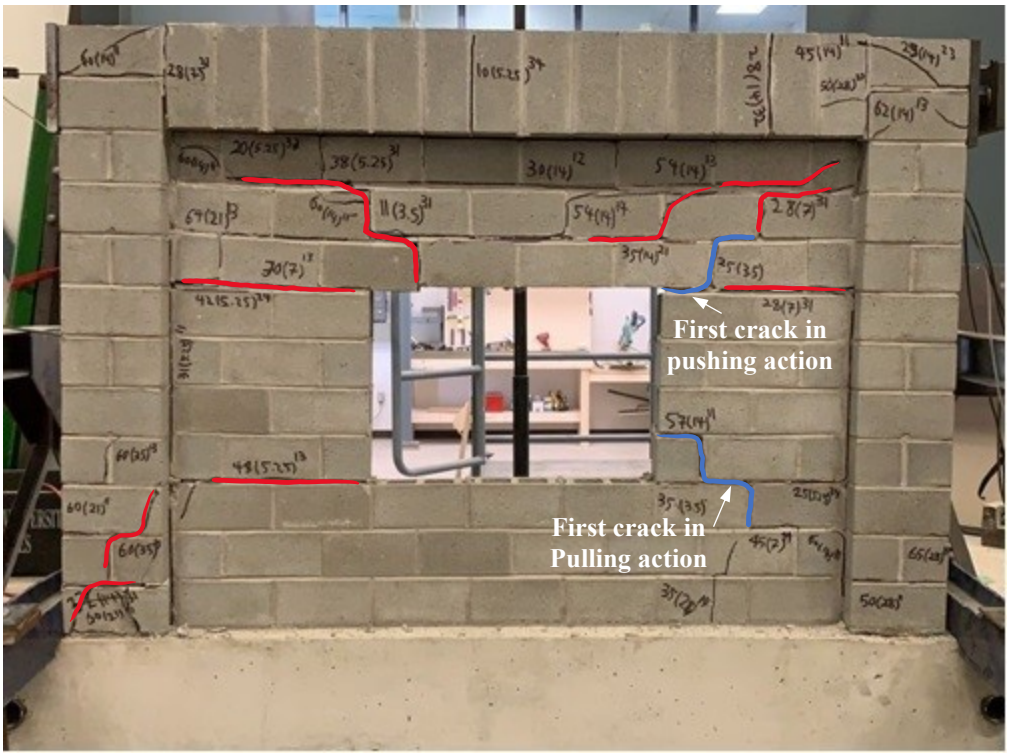


Figure 4.12 Final failure pattern of IF-W-TG-C

The lateral load vs. displacement hysteric response for specimen IF-W-TG-C is shown in Figure 4.13 with specific cycles identified when the cracking load and ultimate load were observed.

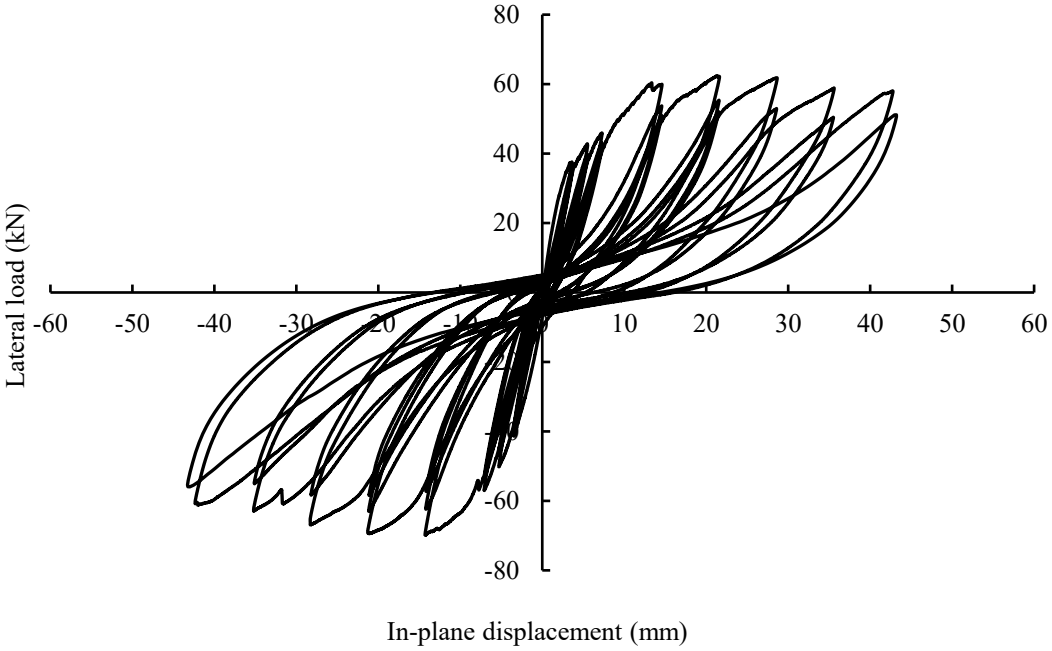


(a) Lateral load vs. in-plane displacement hysteric curve

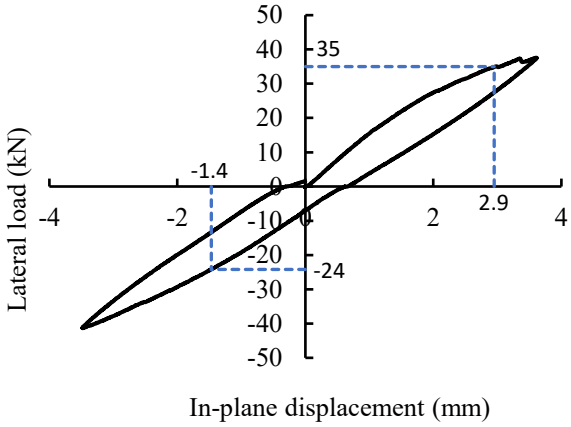


(b) Cracking load and displacement cycle 1, 3.5mm

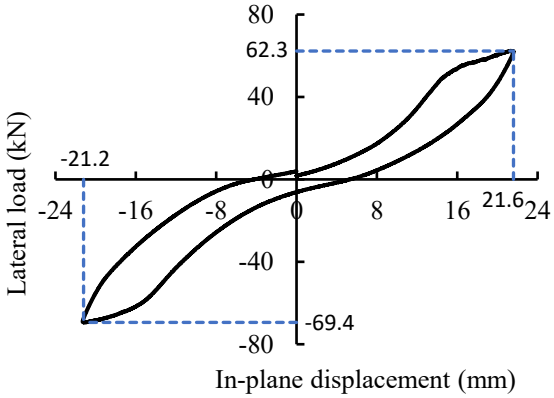


(c) Ultimate load and displacement cycle 13, 21mm

Figure 4.13 Hysteric response curve of IF-W-TG-C

### 4.2.10 Specimen IF-W-SG-C

Figure 4.14 depicts the overall and close-up views of the failure pattern. Failure of specimen IF-W-SG-C was initiated by diagonal cracking during the 5.25 mm ($0.75\Delta_y$) cycle at 40 kN in pulling

action and 33 kN in pushing action. Since the specimen had 6 mm infill-to-column side gaps on both sides, the infill was not fully engaged with the frame during the previous cycles. As the loading continued, diagonal cracks propagated in a manner similar as specimen IF-W-TG-C from the opening corners diagonally to the infill corners. The ultimate loads in pulling and pushing actions were obtained to be 77.5 kN and 90 kN respectively. The final failure was extensive and crushing of masonry at both top corners of the infill was observed. This is the only specimen which showed evident crushing.

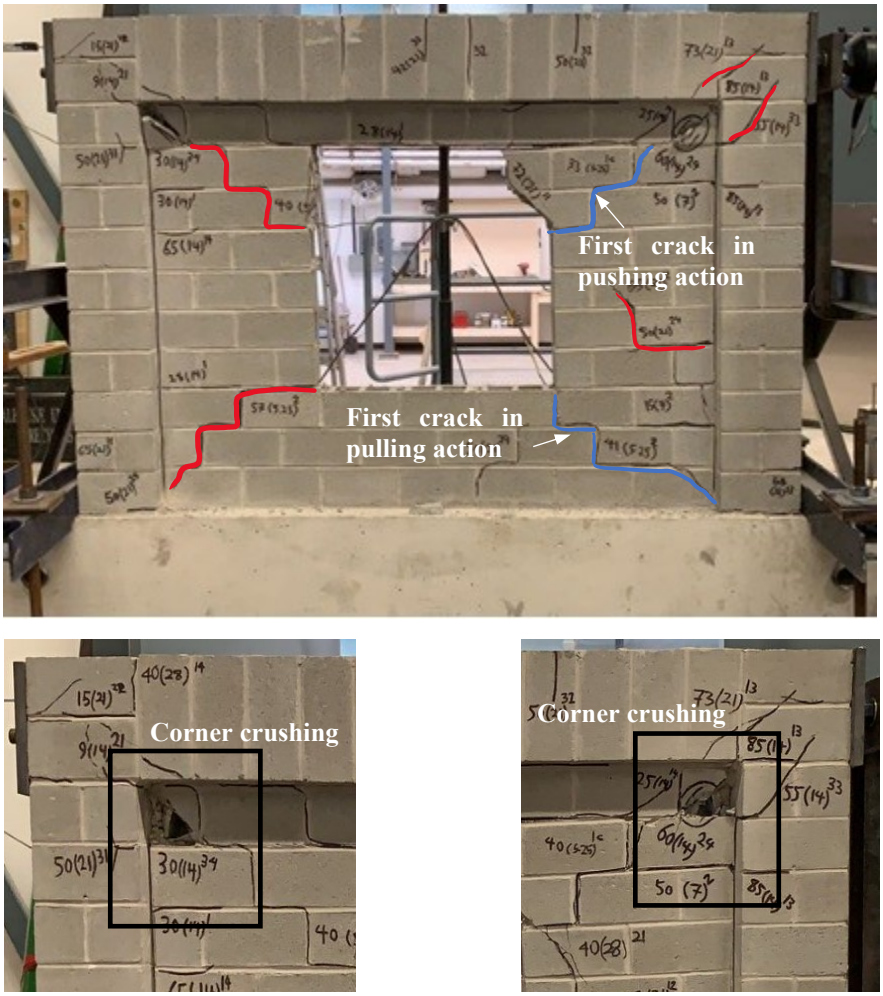


Figure 4.14 Failure pattern of IF-W-SG-C

The lateral load vs. displacement hysteric response for specimen IF-W-SG-C are shown in Figure 4.15 Figure 4.15 with specific cycles separated showing the cracking load and ultimate load cycles.

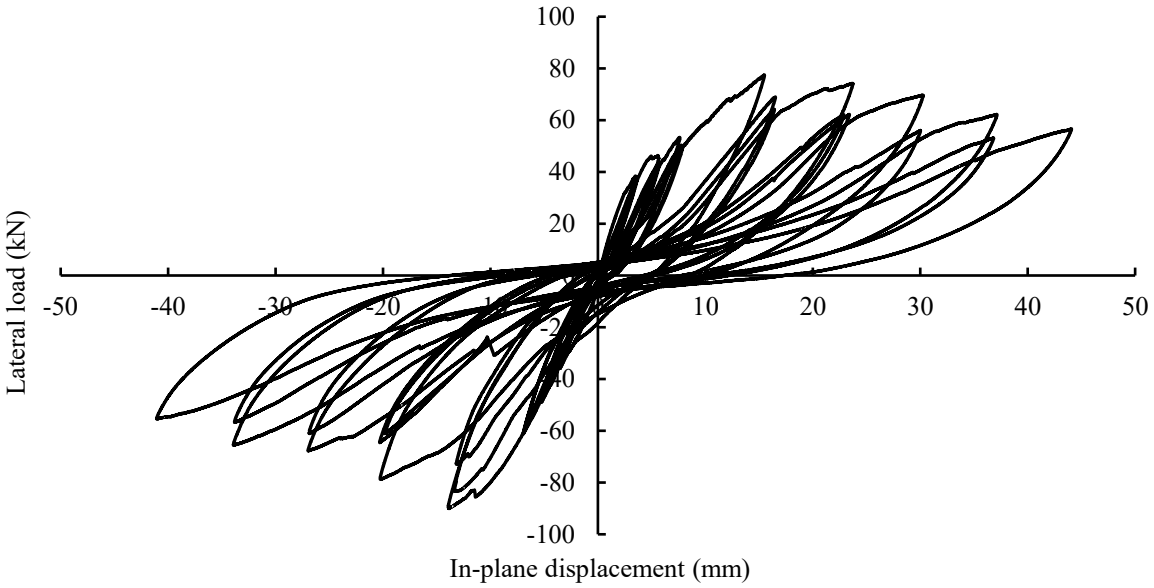


(a) Lateral load vs. in-plane displacemen hysteric curve

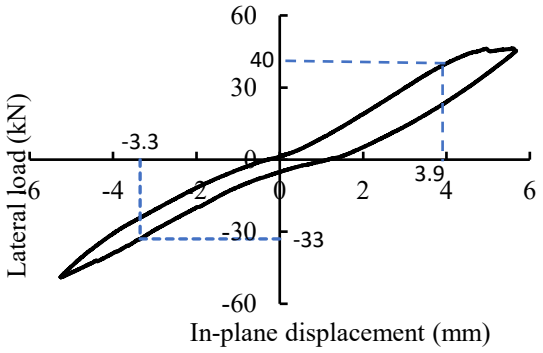


(b) Cracking load and displacement cycle 4, 5.25mm

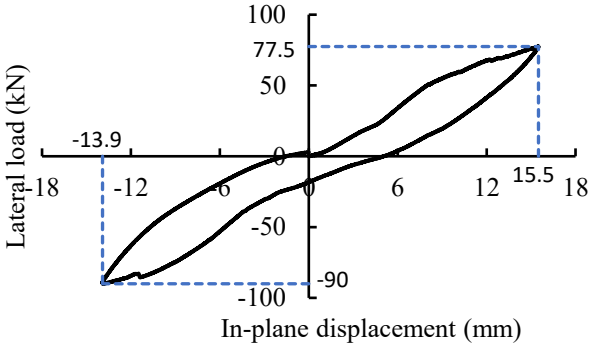


(c) Ultimate load and displacement cycle 10, 14mm

Figure 4.15 Hysteric responcecurve of IF-W-SG-C

### 4.2.11 Pinching

The hysteric curves of both specimens exhibited similar pinching characteristics which are typical of masonry infilled RC frames subjected to cyclic loading. Pinching characteristics of masonry infilled frames are largely attributed to the opening and closing of cracks (Klinger and Bertero 1976). For instance, hysteric curves of specimens IF-W-TG-C and IF-W-SG-C can be considered as two sections illustrated in Figure 4.16 and Figure 4.17. The behaviour of the first section which occurs before cracking cycle without pinching, is almost linear. The second section occurs after cracking point with pinching characteristic.

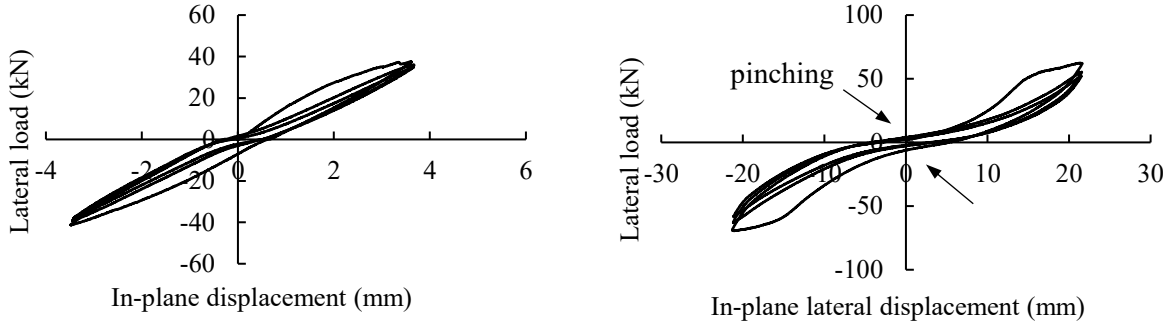


(a) Cycle No. 1 (At cracking) (b) Cycle No. 3 (After cracking)

Figure 4.16 Cyclic load vs. displacement curves of specimen IF-W-TG-C

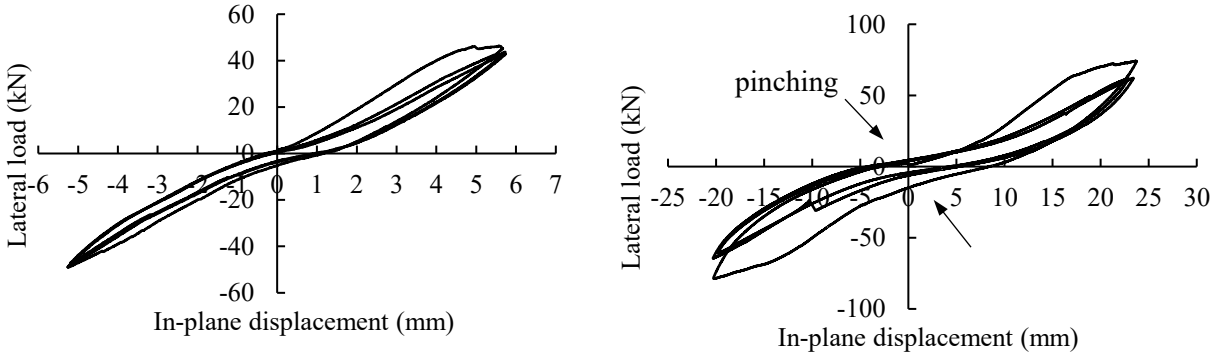


(a) Cycle No. 4 (At cracking) (b) Cycle No. 5 (After cracking)

Figure 4.17 Cyclic load vs. displacement curves of specimen IF-W-SG-C

A comparison of hysteric response curves of both specimens in Figure 4.13 and Figure 4.15 shows that specimen IF-W-SG-C exhibited pinching characteristics more pronounced than specimen IF-W-TG-C with the loops are narrower and stiffness is lower due to the presence of side gaps. The failure mode comparison also shows that cracking in IF-W-SG-C appeared to be more extensive than IF-W-TG-C.

### 4.2.12 Comparison of IF-W-TG-C and IF-W-SG-C

A summary of cracking and ultimate loads and associated displacements in the pulling and pushing actions for both IF-W-TG-C and IF-W-SG-C are presented in Table 4.4. It shows that specimen IF-W-SG-C (side gap) attained higher ultimate loads by 24% and 30% in the pulling and pushing actions, respectively, than specimen IF-W-TG-C (top gap). Similar observation can be made for cracking load albeit with a lower degree of difference.

Table 4.4 Cracking and ultimate load and deflections from hysteric load-displacement curves of IF-W-TG-C and IF-W-SG-C

| Specimen ID | $P_{cr}^{+}$ (kN) | $\Delta_{cr}^{+}$ (mm) | $P_{cr}^{-}$ (kN) | $\Delta_{cr}^{-}$ (mm) | $P_{ult}^{+}$ (kN) | $\Delta_{ult}^{+}$ (mm) | $P_{ult}^{-}$ (kN) | $\Delta_{ult}^{-}$ (mm) |
|---|---|---|---|---|---|---|---|---|
| IF-W-TG-C | 35.0 | 2.9 | -24.0 | -1.4 | 62.3 | 21.6 | -69.4 | -21.2 |
| IF-W-SG-C | 40.0 | 3.9 | -33.0 | -3.3 | 77.5 | 15.5 | -90.0 | -13.9 |

To compare the stiffness of specimens, the following terms are defined, and they are $k_{ini}$ (the initial stiffness), $k_{ini\,sec}$ (the average secant initial stiffness), $k_{cr\,sec}$ (the average secant cracking stiffness), $k_{ult\,sec}$ (the average secant ultimate stiffness). It is suggested (Moslam 1996, Al-Nimry 2014) that the slope of the tangent of the initial linear portion (up to 5% of the ultimate load level) of the first cycle of the load vs. displacement curve be considered as the initial stiffness. The

average secant initial stiffness, $k_{ini\ sec}$, is defined as the slope of the line connecting two extreme points of a cycle where approximately 50% of the ultimate load is obtained. The cracking stiffness, $k_{cr\ sec}$, and ultimate stiffness, $k_{ult\ sec}$, are the slope of the line connecting two extreme points of respective cycles where cracking point ( $P_{cr}$ and $\Delta_{cr}$) and ultimate point ($P_{ult}$ and $\Delta_{ult}$) are obtained. As illustrated in Figure 4.18, Figure 4.19, and Figure 4.20, all three secant stiffnesses can be calculated using Eq. (4-1).

$$K_{sec}=\frac{P_{max}+P_{min}}{\Delta_{max}+\Delta_{min}} \qquad (4\text{-}1)$$

where $P_{max}$ and $\Delta_{max}$, and $P_{min}$ and $\Delta_{min}$, represent the force and corresponding displacement in the positive action and the negative action of a cycle, respectively where the stiffness is sought.

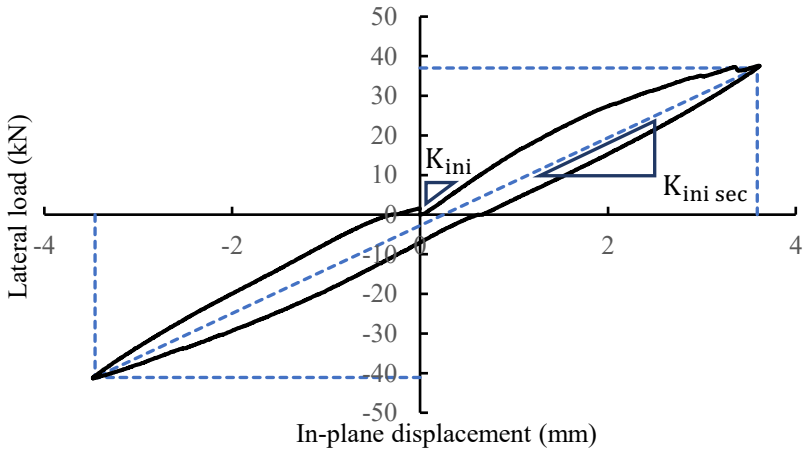


Figure 4.18 Lateral load vs. in-plane displacement of IF-W-TG-C cycle 1, 3.5mm

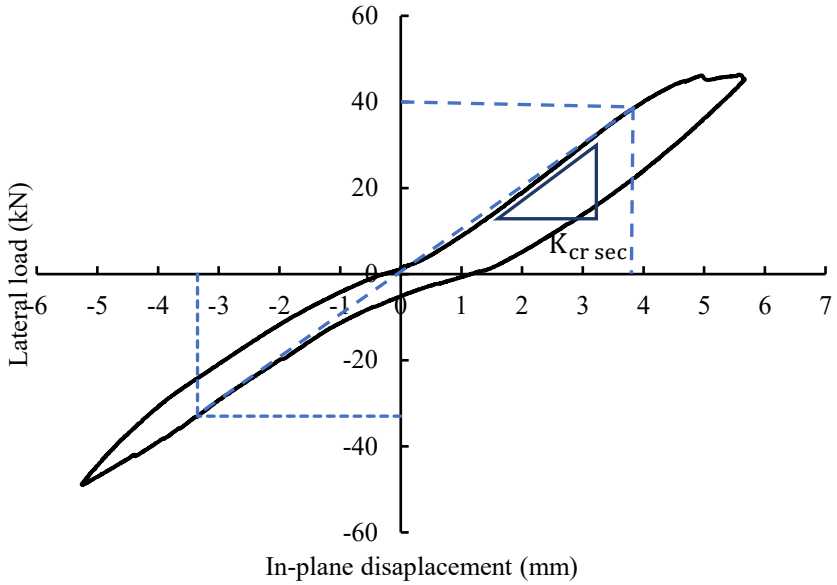


Figure 4.19 Lateral load vs. in-plane displacement of IF-W-SG-C cycle 4, 5.25mm

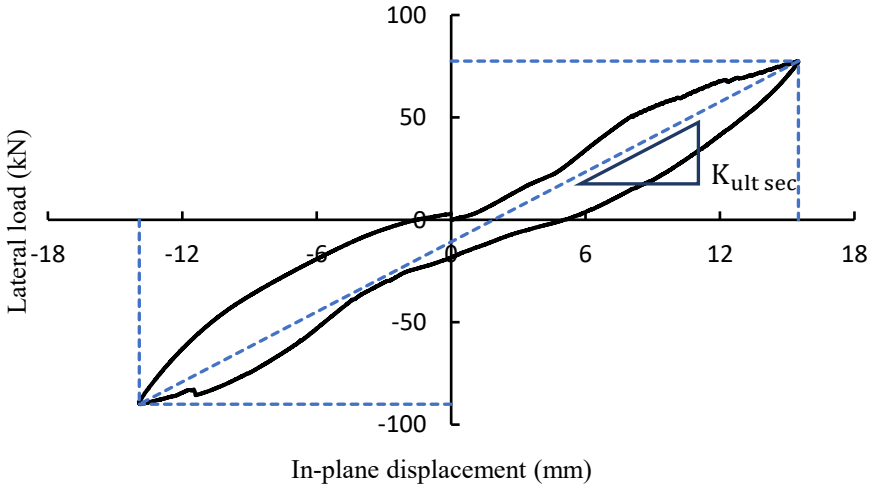


Figure 4.20 Lateral load vs. in-plane displacement of IF-W-SG-C cycle 10, 14mm

Table 4.5 gives a summary of all average secant stiffness and the initial stiffness of IF-W-TG-C and IF-W-SG-C. As shown in Table 4.5, $K_{ini}$ and $K_{ini\ sec}$ of specimens IF-W-TG-C and IF-W-SG-C are close. However, the average secant cracking stiffness ($K_{cr\ sec}$), is greater for specimen IF-W-

TG-C. Lower $K_{cr\,sec}$ for specimen IF-W-SG-C indicates that more deformation was required to close the side gaps at columns and infill before the infill is engaged in the load sharing. On the other hand, IF-W-SG-C showed a greater average secant ultimate stiffness ($K_{ult\,sec}$) than IF-W-TG-C. It suggests that once the side gaps are closed and infill became engaged, the ultimate stiffness is less affected by side gaps than top gaps.

Table 4.5 Average secant stiffness results of IF-W-TG-C and IF-W-SG-C

| ID | Average secant stiffness (kN/mm) | | | |
|---|---|---|---|---|
| | $k_{ini}$ (kN/mm) | $k_{ini\,sec}$ (kN/mm) | $k_{cr\,sec}$ (kN/mm) | $k_{ult\,sec}$ (kN/mm) |
| IF-W-TG-C | 15.2 | 11 | 13.3 | 3 |
| IF-W-SG-C | 12.6 | 10.5 | 9.3 | 5.7 |

As a cyclic behaviour indicator, loading and unloading stiffness degradation of each successive cycle of both specimens is also compared. The loading and unloading stiffness were obtained using the secant stiffness of the positive and negative portions of each cycle, as defined in Figure 4.21. Figure 4.22 and Figure 4.23 illustrate the average loading and unloading stiffness from the positive and negative cycles vs. the drift for each specimen. Both specimens showed similar stiffness degradation trend as drift increased. This trend is approximately exponential with a higher rate of reduction of stiffness in the low range of drift and the rate diminishes as the drift increases into the high range. The degradation is more or less symmetrical on the pull and pushing actions.

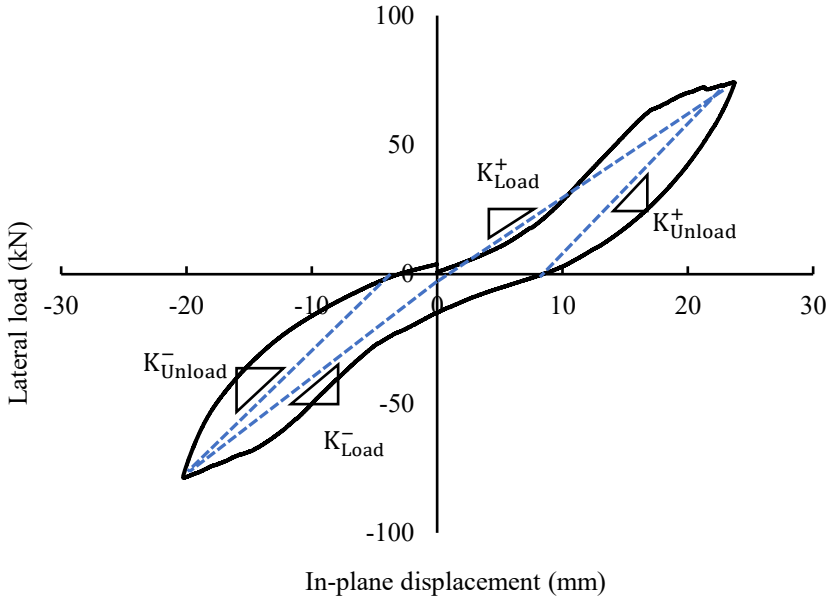


Figure 4.21 Lateral load vs. in-plane displacement a single cycle of IF-W-SG-C

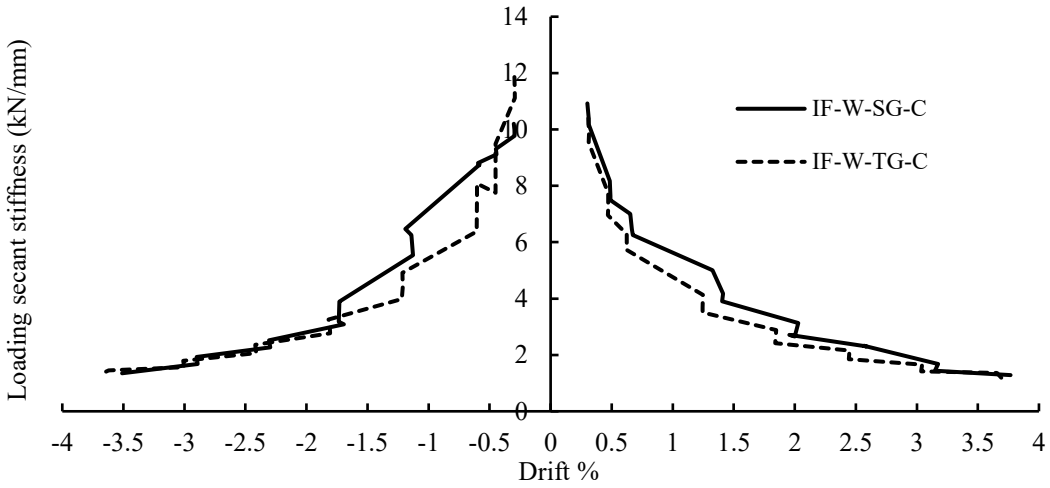


Figure 4.22 Loading secant stiffness vs. drift of IF-W-TG-C and IF-W-SG-C

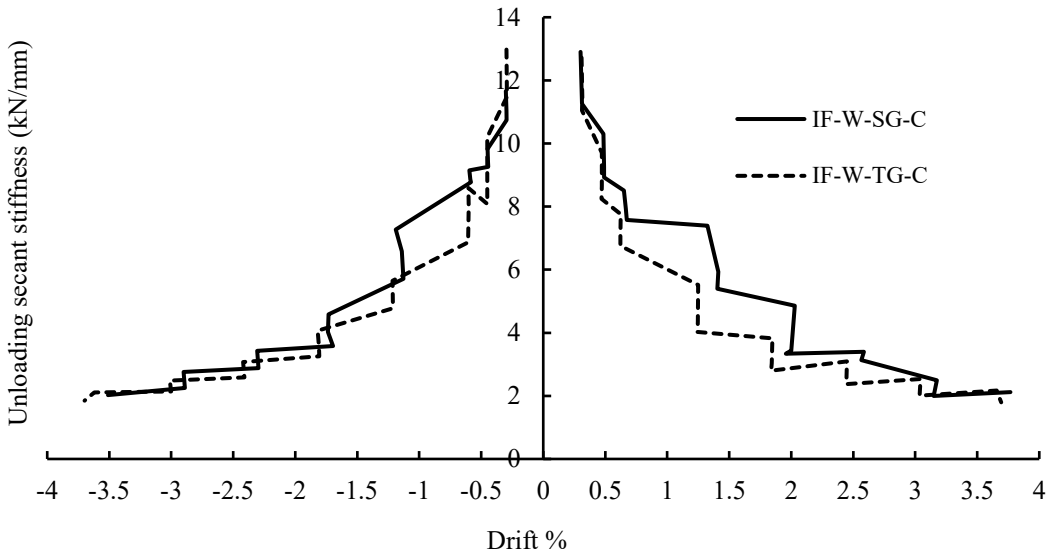


Figure 4.23 Unloading secant stiffness vs. drift of IF-W-TG-C and IF-W-SG-C

From the hysteric curves, backbone curves of the two specimens were generated by connecting the peak points of each successive cycle of the hysteric curves. For cycles with same displacement amplitudes, the higher load values are utilised in generating the backbone curve. Backbone curves for IF-W-TG-C and IF-W-SG-C are depicted in Figure 4.24. The backbone curve presents an equivalent monotonic load vs displacement relationship of a cyclically loaded specimen. Although monotonically loaded specimens typically have a higher ultimate load than cyclically loaded counterparts, backbone curves are a good indicator of characteristics of cyclically loaded specimens using familiar monotonic-like curves. Figure 4.24 shows higher strength and higher stiffness for IF-W-SG-C as side gaps were closed at cycles with higher amplitudes.

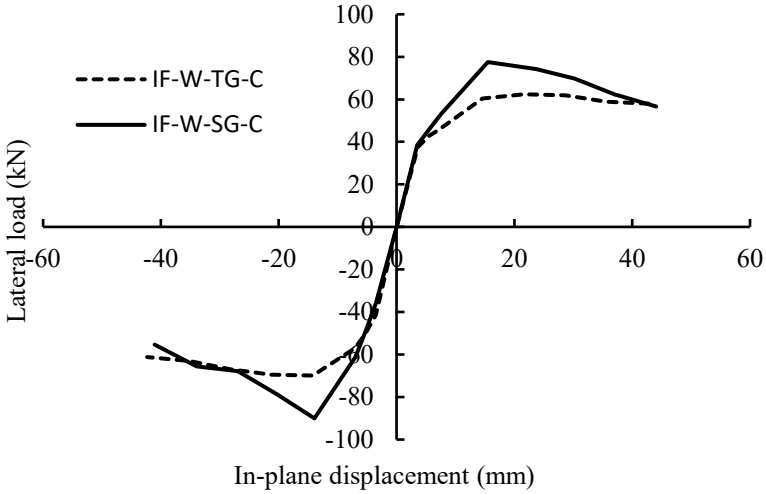


Figure 4.24 Hysteretic backbone curves of IF-W-TG-C and IF-W-SG-C

### 4.2.13 Ductility

Ductility is defined as how much a structure or a member can tolerate deformation after the yield point while maintaining most of its load-carrying capacity. As ductility of masonry structures depends on a wide range of factors, including structural geometry, reinforcement ratio and axial load ratio, ductility factor may be calculated using ASCE 41 (2017). According to ASCE 41 (2017), to calculate the ductility ratio ($R_d$) in nonlinear static analyses, an actual force displacement curve can be replaced by an idealized three-line segment curve defined by $P_y$, $P_{ult}$, and $P_{fail}$ as shown in Figure 4.25. On the three-line segment curve, $P_{ult}$ corresponds the ultimate strength (maximum) whereas $P_{fail}$ corresponds the point where 20% of the ultimate strength is lost on the actual force-displacement curve. The first line segment connects the origin to a point on the actual force-displacement curve at a load equal to 60% of yield point $P_y$. The yield point of the system, $P_y$, must be less than the maximum point, $P_{ult}$, and can be found through an iterative process considering that the area under the actual and idealized curves are equal. The ductility ratio

is calculated as the ratio of the ultimate displacement to yield displacement as illustrated in Eq. (4-2). The idealized and actual curves of IF-LA-80 as an example is shown in Figure 4.25.

$$R_d = \frac{\Delta_{fail}}{\Delta_y} \quad (4\text{-}2)$$

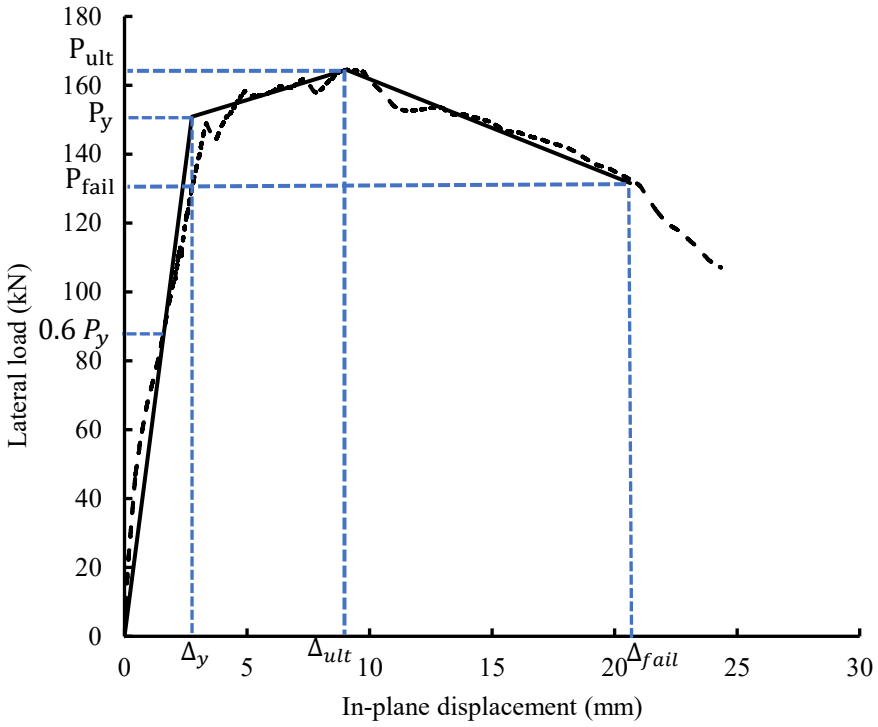


Figure 4.25 Idealized force-displacement curve of IF-LA-80

In this study, a 20% reduction in the load after reaching $P_{ult}$ (or a significant sudden load drop after ultimate point) was chosen to determine $P_{fail}$ and $\Delta_{fail}$. In the case where the test was discontinued before this point (specimen IF-LA-160), the last point of the curve was used to determine $P_{fail}$ and $\Delta_{fail}$. Idealized curves of specimens under monotonic lateral loading are shown in Figure 4.26.

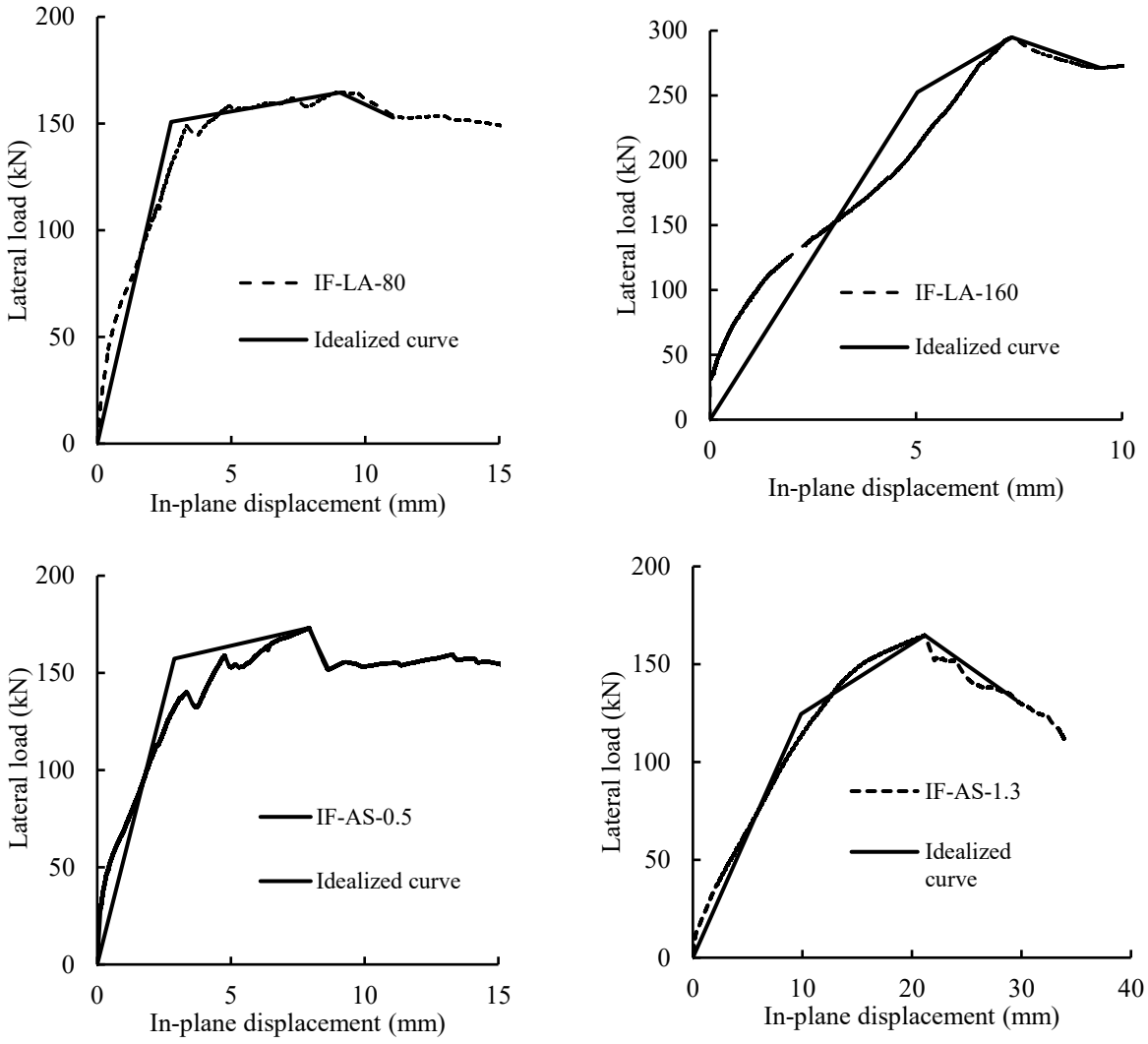


Figure 4.26 Idealized curve for specimens under monotonic lateral loading

Table 4.6 provides a summary of the ductility factor of all specimens. For specimens IF-W-TG-C and IF-W-SG-C under cyclic lateral loading, the ductility factor was calculated according to ASCE 41 (2017) method, using the backbone curve for both pushing and pulling actions, as indicated in Figure 4.27.

Table 4.6 Summary of ductility factors of specimens

| Specimen ID | $P_y$ (kN) | $P_{ult}$ (kN) | $P_{fail}$ (kN) | $\Delta_y$ $(mm)$ | $\Delta_{fail}$ $(mm)$ | $R_d$ |
|---|---|---|---|---|---|---|
| IF-LA-80 | 150.7 | 164.5 | 152.7 | 2.7 | 11.0 | 4.0 |
| IF-LA-160 | 252.5 | 294.8 | 271.3 | 5.0 | 9.4 | 1.9 |
| IF-AS-0.5 | 157.3 | 173.1 | 151.7 | 2.9 | 8.6 | 3.0 |
| IF-AS-1.3 | 113.3 | 165.0 | 131.8 | 8.8 | 29.5 | 3.4 |
| IF-W-TG-C | 46.8 | 62.4 | 58.0 | 4.5 | 42.1 | 9.3 |
| | -53.4 | -69.9 | -61.2 | -4.5 | -42.0 | 9.3 |
| IF-W-SG-C | 49.1 | 77.5 | 62.0 | 4.5 | 37.3 | 8.3 |
| | -40.8 | -90.0 | -67.0 | -4.0 | -24.4 | 7.4 |

Overall, all specimens attained ductility ratios well above 1.0, ranging from 1.9 to 9.3. In the current National Building Code of Canada (NBCC 2015), masonry infilled frames are not a recognized category of lateral load resisting system and thus their ductility ratios are assigned to be 1.0 for design. The table shows that the all-masonry infilled frames are capable of attaining more ductility than what are specified in design. Despite the infill openings and interfacial gaps, the specimens under cyclic loading conditions had the highest ductility ratio.

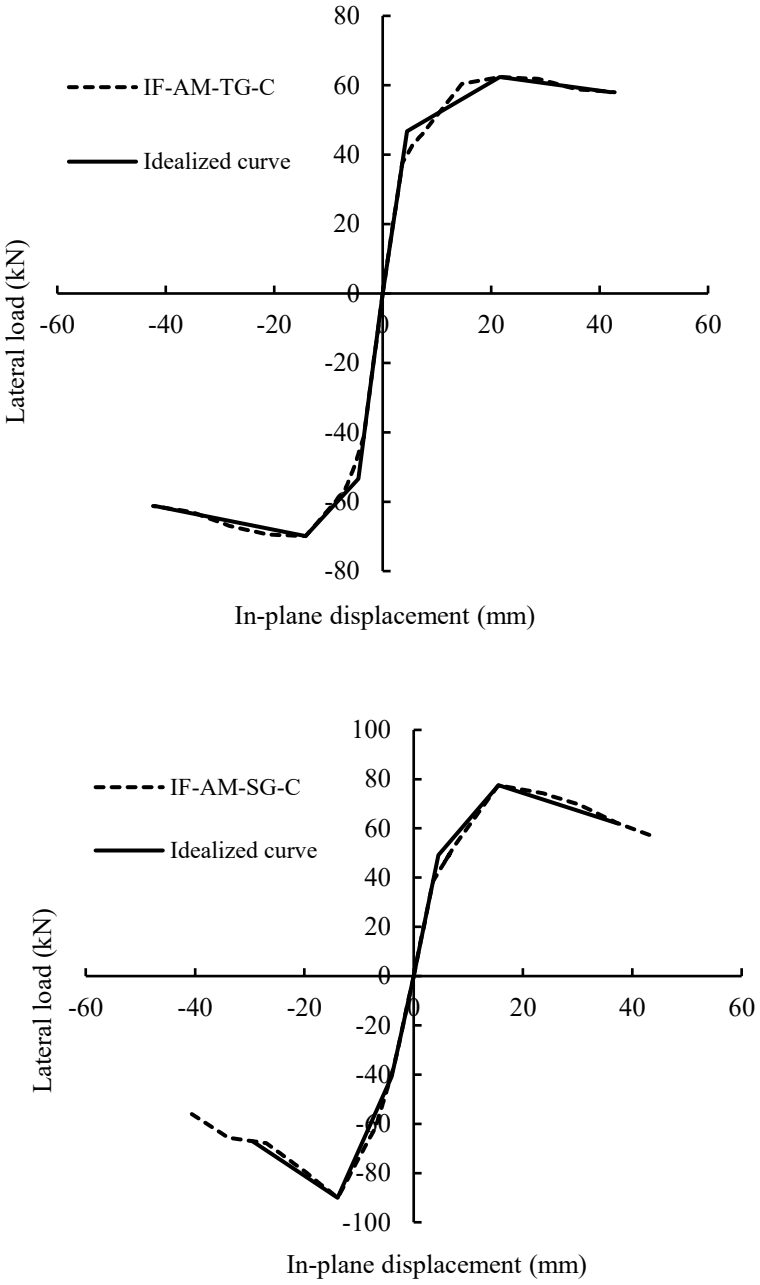


Figure 4.27 Idealized backbone curve for specimens under cyclic lateral loading

# CHAPTER 5 COMPARATIVE STUDY OF EXPERIMENTAL RESULTS AND EVALUATION OF ANALYTICAL METHODS

## 5.1 INTRODUCTION

This chapter first presents comparisons of the experimental results obtained from this study and studies conducted in the same research group (Foroushani, 2019; Steeves, 2017) on all-masonry infilled frames and masonry infilled RC frames. Secondly, the applicability of analytical methods for calculation of infill in-plane stiffness and strength suggested in the Canadian and American masonry design standards on all-masonry infilled frames is investigated.

## 5.2 Comparison with experimental results of Foroushani (2019)

Foroushani (2019) conducted an experimental study on the in-plane behaviour of all masonry infilled frames under monotonic lateral loading with a similar specimen geometry and dimensions and test setup and procedure. Included in the comparison were two specimens from Foroushani's study: 1) control specimen (IF-RS), and 2) masonry infilled specimen with an axial load (80 kN) applied to the frame top beam (IF-RS-A). They were compared with specimen IF-LA-80 from this study for axial load study and specimens IF-AS-0.5 and IF-AS-1.3 for aspect ratio study.

(a) Vertical load study

Specimens IF-RS-A (Foroushani 2019) and IF-LA-80 (current study) were all tested under combined lateral and axial loading. The only difference between these two specimens was the manner in which how the axial load was applied. While for specimen IF-LA-80, the axial load (80 kN) was applied through the frame columns when the lateral load was increased to specimen failure, for specimen IF-RS, the same level of axial load was applied but on the frame top beam at

the one-third of the infill length from each side. The lateral load vs. in-plane displacement curves of specimens are compared in Figure 5.1. The summary of test results is illustrated in Table 5.1 Table 5.1.

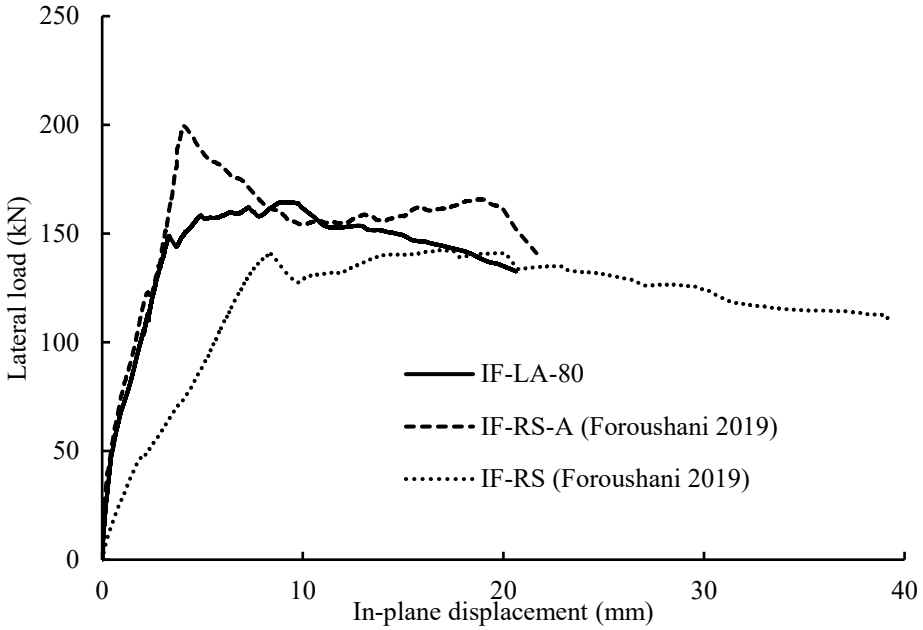


Figure 5.1 Comparison of load vs. displacement curves of current and Foroushani's study (2019) for vertical load effect

Table 5.1 Comparison of test result of current and Foroushani's study (2019) for vertical load effect

| | Specimen ID | $f'_m$ (MPa) | $k_{in}$ (kN/mm) | $k_{cr}$ (kN/mm) | $k_{ult}$ (kN/mm) | $P_{cr}$ (kN) | $P_{ult}$ (kN) |
|---|---|---|---|---|---|---|---|
| Current Studdy | IF-LA-80 | 16.8 | 101.4 | 45.9 | 18.6 | 147.0 | 164.0 |
| Foroushani (2019) | IF-RS-A | 18.9 | 175.0 | 51.8 | 48.7 | 124.5 | 199.6 |
| | IF-RS | 18.9 | 26.6 | 17.9 | 8.1 | 93.4 | 142.5 |

The comparison shows that the presence of vertical load, whether applied through the frame columns or frame top beam, increased the lateral strength of the masonry infilled frames.

Comparing with the control specimen (IF-RS), specimen IF-RS-A with 80 kN applied on the top beam attained about 40% greater lateral capacity whereas specimen IF-LA-80 with 80 kN applied through frame columns attained about 13% greater lateral capacity. In other words, the axial load applied through the top beam resulted in a greater lateral capacity of infilled frames than when the axial load applied through the frame columns. Table 5.1 shows that the crack stiffnesses for specimens IF-LA-80 and IF-RS-A were more or less in the same range and significantly higher than the crack stiffness for IF-RS, indicating a stiffer system as a result of the vertical load. However, the ultimate stiffness of IF-RS-A was much higher than IF-LA-80, indicating an even stiffer system at failure when the vertical load is applied through the frame beam than when applied to the frame columns. Figure 5.1 shows the failure of IF-RS-A was sudden as indicated by a significnt load drop with no evident "plateau" developed in the response curve before failure whereas IF-LA-80 seemed to show a more ductile failure with a gentler load drop and an evident "plateau". The final failure modes for all three specimens are illustrated in Figure 5.2. All three specimens were failed by diagonal cracking extending into the boundary column region. While IF-RS and IF-LA-80 attained more extensive diagonal cracking at failure, IF-RS-A attained only one significant diagonal crack and a more severe boundary column cracking shear failure.

Based on ASCE 41 ductility definition, the ductility factors for these specimens were calculated and compared in Table 5.2. It indicates that specimen IF-RS-A had the lowest ductility factor among these three specimens. Therefore, it can be concluded that applying vertical load on frame top beam (above infill) causes a significant decrease (40%) in ductility.

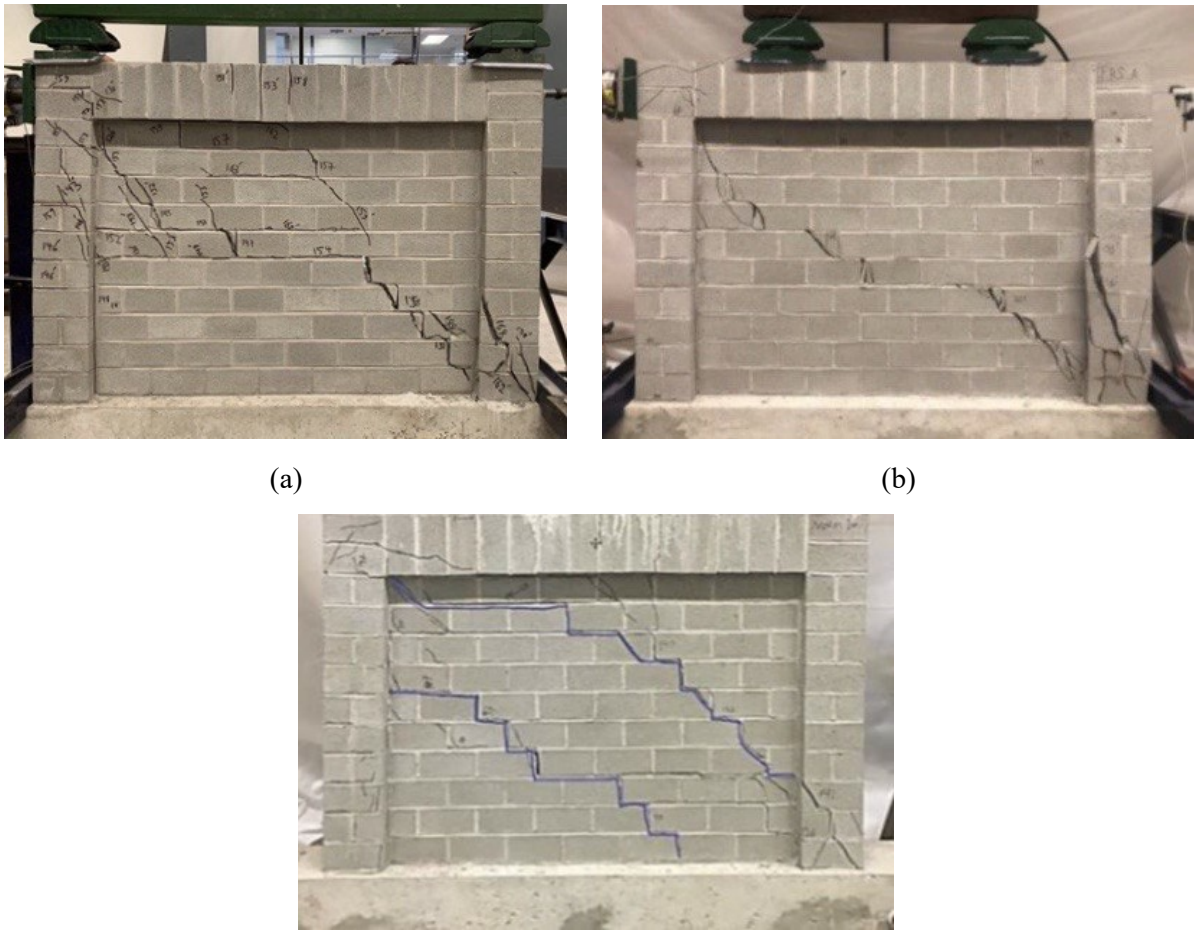

(a) (b)

(c)

Figure 5.2 Comparison of failure modes of (a) IF-LA-80, (b) IF-RS-A and (c) IF-RS

Table 5.2 Ductility comparison of current and Foroushani (2019)'s study for vertical load effect

| | Specimen ID | $\Delta_y$ $(mm)$ | $\Delta_{fail}$ $(mm)$ | Ductility R | Final failure mode |
|---|---|---|---|---|---|
| Current Studdy | IF-LA-80 | 2.7 | 11.0 | 4.0 | DC |
| Foroushani (2019) | IF-RS-A | 3.5 | 8.7 | 2.5 | DC |
| | IF-RS | 8.0 | 32.4 | 4.0 | DC |

(b) Aspect ratio study

Specimens IF-AS-0.5 and IF-AS-1.3 (current study) and IF-RS (Foroushani's study) were used in this comparison. Lateral load vs. in-plane displacement curve of these specimens are illustrated in Figure 5.3 and the summary of test results is shown in Table 5.3. It can be seen that as the aspect ratio increases, i.e., the infill becomes more slender, the crack stiffness and ultimate stiffness decrease, indicating a more ductile behaviour. As the infill changes from squat (low aspect ratio) to slender (high aspect ratio), it is reasonable to deduce that the system behaviour shifts to a more flexural behaviour (bending) and less shear behaviour which is reflected through an overall more ductile response. However, the lateral strength does not suggest the same correlation. While the

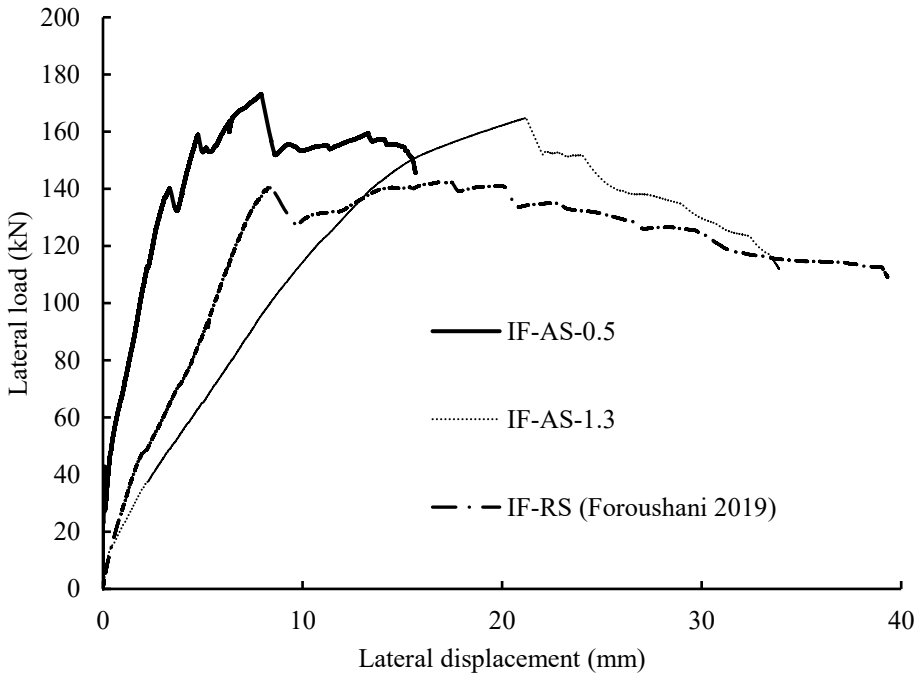


Figure 5.3 Comparison of load vs. displacement curves of current and Foroushani (2019)'s study for aspect ratio effect

squat and slender infilled specimens attained similar lateral strength, the infill with the intermediate aspect ratio showed the lowest strength. It suggests that the lateral strength might be more relied upon the overall geometry of the infill, i.e., the diagonal length of the infill.

Table 5.3 Comparison of test result of current and Foroushani (2019)'s study for aspect ratio effect

| | Specimen ID | Aspect ratio | $f'_m$ (MPa) | $k_{in}$ (kN/mm) | $k_{cr}$ (kN/mm) | $k_{ult}$ (kN/mm) | $P_{cr}$ (kN) | $P_{ult}$ (kN) |
|---|---|---|---|---|---|---|---|---|
| Current Study | IF-AS-0.5 | 0.5 | 16.0 | 280.0 | 43.4 | 21.7 | 139 | 173 |
| | IF-AS-1.3 | 1.3 | 16.8 | 43.3 | 10.7 | 7.8 | 127 | 165 |
| Foroushani (2019) | IF-RS | 0.73 | 18.9 | 26.6 | 17.9 | 8.1 | 93.4 | 142.5 |

Figure 5.4 shows the final failure modes of the three specimens. Diagonal cracking is the control failure mode for three, indicating the formation of the diagonal strut for resisting the lateral load. The slender infilled specimen showed the most pronounced in-plane bending while the other two specimens showed more extensive diagonal cracking in the infill.

Table 5.4 summarizes ductility factors of the specimens. While a correlation between the ductility factor and infill aspect ratio is not evident, one observation is that all specimens showed a ratio greater than 1.0, indicating that their ability to sustain deflection after yielding is greater than the specified value by the current design practice (NBCC 2015). Specimen IF-AS-0.5 with the lowest aspect ratio showed less ductility comparing the other two specimens.

(a)

(b)

(c)

Figure 5.4 Comparison of failure modes of (a) IF-AS-0.5, (b) IF-AS-1.3 and (c) IF-RS

Table 5.4 Ductility comparison of current and Foroushani (2019)'s study for aspect ratio effect

| | Specimen ID | Aspect ratio (h/l) | $\Delta_y$ $(mm)$ | $\Delta_{fail}$ $(mm)$ | Ductility R | Fainal failure mode |
|---|---|---|---|---|---|---|
| Current Studdy | IF-AS-0.5 | 0.5 | 2.9 | 8.6 | 3.0 | DC |
| | IF-AS-1.3 | 1.3 | 8.8 | 29.5 | 3.4 | DC |
| Foroushani (2019) | IF-RS | 0.73 | 8.0 | 32.4 | 4.0 | DC |

## 5.3 Comparison with experimental results of Steeves (2017)

Steeves (2017) conducted an experimental study on masonry infilled RC frames subjected to cyclic lateral loading. Included in the comparison were specimens from the current study IF-W-TG-C (top gap 12 mm) and IF-W-SG-C (side gap with 6 mm on each frame-column side) and two masonry infilled RC frame counterparts from Steeves (2017)'s study. The specimen geometry and dimensions, gap size and location, test setup, loading protocol and procedures were kept identical between the specimens. Table 5.5 provides a summary of cracking and ultimate loads and displacements in the pulling and pushing actions for all specimens and the average secant stiffness results are shown in Table 5.6. A general review of the tables indicates that both sets of specimens behaved comparably with similar values of all performance indicators.

Table 5.5 Cracking and ultimate load and deflections from hysteric load-displacement curves of current and Steeves (2017)'s study

| | Specimen ID | $P_{cr}^{+}$ (kN) | $\Delta_{cr}^{+}$ (mm) | $P_{cr}^{-}$ (kN) | $\Delta_{cr}^{-}$ (mm) | $P_{ult}^{+}$ (kN) | $\Delta_{ult}^{+}$ (mm) | $P_{ult}^{-}$ (kN) | $\Delta_{ult}^{-}$ (mm) |
|---|---|---|---|---|---|---|---|---|---|
| Current Study | IF-W-TG-C | 35.0 | 2.9 | -24.0 | -1.4 | 62.3 | 21.6 | -69.4 | -21.2 |
| | IF-W-SG-C | 40.0 | 3.9 | -33.0 | -3.3 | 77.5 | 15.5 | -90.0 | -13.9 |
| Steeves (2017) | IF-W-TG12 | 19.4 | 3.4 | -19.3 | -2.7 | 64.8 | 28.2 | -71.8 | -26.8 |
| | IF-W-SG12 | 31.8 | 8.3 | -25.1 | -4.4 | 64.2 | 27.3 | -66.9 | -31.4 |

Table 5.6 Average secant stiffness results for selected specimens of current and Steeves (2017)'s study

| | SpecimenID | Average secant stiffness (kN/mm) | | | |
|---|---|---|---|---|---|
| | | $k_{ini}$ (kN/mm) | $k_{ini\ sec}$ (kN/mm) | $k_{cr\ sec}$ (kN/mm) | $k_{ult\ sec}$ (kN/mm) |
| Current Study | IF-W-TG-C | 15.2 | 11.0 | 13.3 | 3.0 |
| | IF-W-SG-C | 12.6 | 10.5 | 9.3 | 5.7 |
| Steeves (2017) | IF-W-TG12 | 24.7 | 9.1 | 6.3 | 2.5 |
| | IF-W-SG12 | 19.1 | 8.8 | 4.5 | 2.2 |

Table 5.7 summarizes failure modes for these four specimens whereas Figure 5.5 and Figure 5.6 illustrate the experimentally observed failure mode of specimens. The observed failure patterns appear to be similar where diagonal cracking extending from the opening corners to infill corners. Similarly, both specimens with side gaps showed some corner crushing.

Table 5.7 Summary of failure modes for specimens of current and Steeves (2017)'s study

| | Specimen ID | $f'_m$ (MPa) | Final failure mode (+) | Final failure mode (-) |
|---|---|---|---|---|
| Current Study | IF-W-TG-C | 16.8 | DC | DC |
| | IF-W-SG-C | 16.8 | CC | CC |
| Steeves (2017) | IF-W-TG12 | 10.5 | DC | DC |
| | IF-W-SG12 | 10.5 | CC | DC |

(a)

(b)

Figure 5.5 Comparison of failure modes of (a) IF-W-TG-C (b) IF-W-TG12

(a)

(b)

Figure 5.6 Comparison of failure modes of (a) IF-W-SG-C (b) IF-W-SG12

The backbone curves for the specimens are compared in Figure 5.7. It can be seen that all specimens showed similar behavioural trend. However, it is noted that the infill compressive strength between the two sets of specimens were quite different. To have a more valid comparison

of strength, the backbone curves were normalized by dividing the lateral strength by the masonry strength $f'_m$ and the normalized curves are shown in Figure 5.8. The normalized curves showed

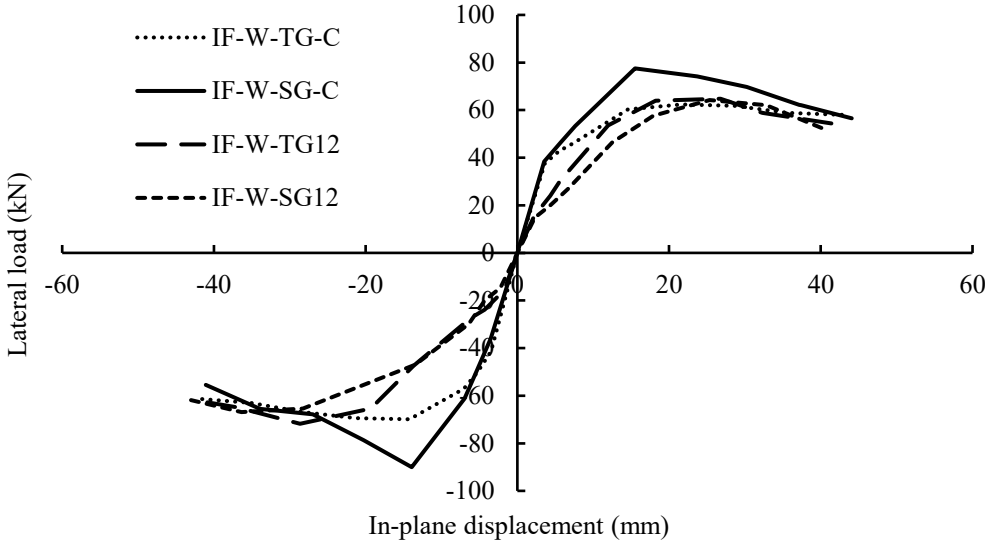


Figure 5.7 Hysteretic backbone curves of current and Steeves (2017)'s study

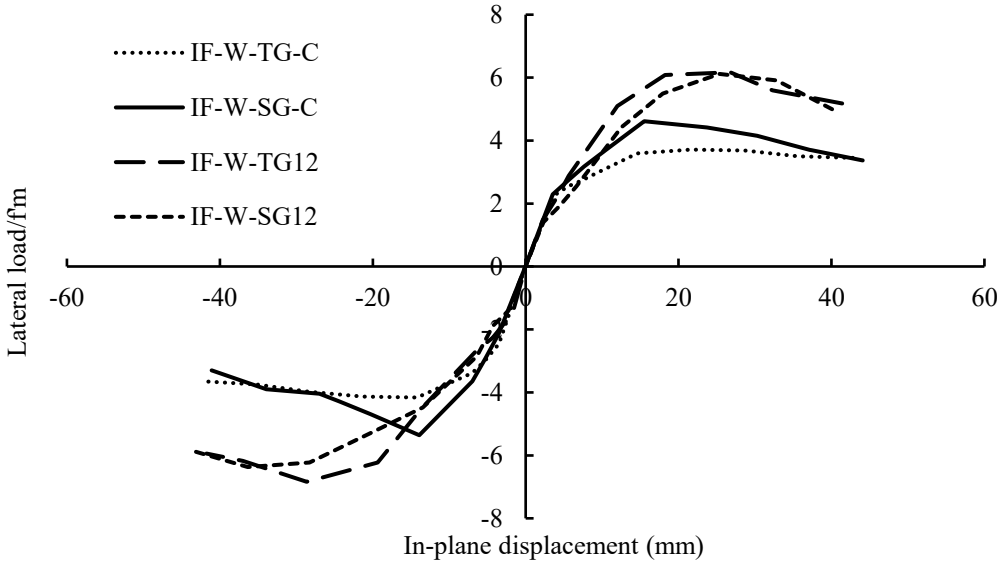


Figure 5.8 Normalized backbone curves of current and Steeves (2017)'s study

that the masonry infilled RC frames attained greater strength in both pulling and pushing actions under the assumption that the lateral strength of the infilled frame system is linearly correlated with the masonry infill strength, a simplification that the infilled frame derives its lateral strength mainly from the infill strength. It is not exactly accurate as the frame strength is ignored in this assumption. Hence, it is cautioned that the degree of difference in lateral strength between two systems may not be as large as suggested.

Table 5.8 illustrates the ductility factors for the specimens under cyclic loading. As can be seen, all-masonry infilled frame specimens have higher ductility ratios in comparison with masonry infilled RC frames under cyclic loading. For both kind of systems, specimens with side gaps had lower ductility in comparison with specimens with top gaps.

Table 5.8 Ductility comparison of current and Steeves (2017)'s study for cyclic study

| | Specimen ID | $\Delta_y$ $(mm)$ | $\Delta_{fail}$ $(mm)$ | Ductility R |
|---|---|---|---|---|
| Current Study | IF-W-TG-C | 4.5 | 42.1 | 9.3 |
| | IF-W-SG-C | 4.5 | 37.3 | 8.3 |
| Steeve (2017) | IF-W-TG12 | 10.8 | 41.4 | 3.8 |
| | IF-W-SG12 | 15.8 | 40.0 | 2.5 |

## 5.4 EVALUATION OF CSA S304.14 AND TMS 402/602-16

Since the all-masonry infilled frame is a new form of infilled frames, the current standard equations in CSA S304.14 and TMS402/602 do not strictly apply. However, the above discussions indicate that its behaviour is comparable to the infilled RC frames, it is thus a useful exercise to evaluate the applicability of the code equations (intended for steel or RC framed infills) to this form of infilled frames. Also noted is that the code equations do not address the effect of combined vertical

and lateral load, and infills with opening and gaps, thus the evaluation was conducted using only two specimens (IF-AS-0.5 and IF-AS-1.3).

### 5.4.1 CSA S304.14 stiffness evaluation

For ease of reference, the equations contained in CSA S304-14 for design of infills are summarized in the following. Using the single diagonal strut concept, the strut width is expressed as:

$$w_{eff} = \frac{1}{2}\sqrt{{\alpha_h}^2 + {\alpha_l}^2} \quad (5\text{-}1)$$

where $\alpha_h$ and $\alpha_l$ are the contact length between the infill and top beam and column, respectively, and are calculated as follows:

$$\alpha_h = \frac{\pi}{2}\sqrt[4]{\frac{4E_f I_c h_m}{E_m t_e \sin(2\theta)}} \quad (5\text{-}2)$$

$$\alpha_l = \pi\sqrt[4]{\frac{4E_f I_b l_m}{E_m t_e \sin(2\theta)}} \quad (5\text{-}3)$$

For stiffness calculation, CSA applies a reduction factor of 0.5 for $w_{eff}$, and then compared with quarter of the diagonal length, whichever is less would be considered as the effective width. Table 5.9 shows the calculated strut width values for specimens IF-AS-0.5 and IF-AS-1.3.

Table 5.9 Strut width values of IF-AS-0.5 and IF-AS-1.3 according to CSA S304-14

| Specimen ID | $\alpha_h$ (mm) | $\alpha_l$ (mm) | $w_{eff}$ (mm) |
|---|---|---|---|
| IF-AS-0.5 | 571.2 | 1353.2 | 734.4 |
| IF-AS-1.3 | 631.1 | 1182.9 | 670.4 |

A simple frame analysis can then be performed to determine the system stiffness with the infill replaced by a diagonal strut of a width $w_{eff}$, and thickness $t_e$, and material properties of the infill.

Table 5.10 presents the comparison of the experimental crack stiffness and the stiffness values based on CSA S304 equation. A sample stiffness calculation for specimen IF-AS-0.5 is provided in Appendix C. Note that the S304 equation is developed based on the diagonal strut concept which implies that the frame has deformed and separation between the infill and the frame at unloaded corners has occurred. It is therefore reasonable to assume that the infill has sustained some level of cracking. It is believed that the crack stiffness is more appropriate in the comparison with the code values. Tucker (2007) and Manesh (2013) also supported this observation.

Table 5.10 Summary of comparison of CSA S304.14 and experimental crack stiffness

| Specimen ID | Test result | CSA S304-14 | $(k_{CSA}/k_{cr})$ |
|---|---|---|---|
| | $k_{cr}(kN/mm)$ | $k_{CSA}(kN/mm)$ | |
| IF-AS-0.5 | 43.4 | 83.3 | 1.9 |
| IF-AS-1.3 | 10.7 | 34.5 | 3.2 |

As can be seen, the code-to-experimental stiffness ratio for IF-AS-0.5 and IF-AS-1.3 are 1.9 and 3.2, respectively, indicating that CSA S304.14 overestimates the stiffness of all-masonry infilled frames. This is in line with observations reported for masonry infilled RC frames from previous studies.

### 5.4.2 TMS 402/602 stiffness evaluation

Also based on single diagonal strut concept, TMS 402/602 standard, however, suggests a different equation for the strut width as follows:

$$w = \frac{0.3}{\lambda \cos\theta} \qquad (5\text{-}4)$$

where $\lambda$ is the stiffness parameter, defined as below (Smith and Carter 1969):

$$\lambda = \sqrt[4]{\frac{E_m t_e \sin\theta}{4E_f I_c h_m}} \qquad (5\text{-}5)$$

Table 5.11 presents the strut width values for specimens IF-AS-0.5 and IF-AS-1.3 based on TMS 402/602 equations.

Table 5.11 Strut width values of IF-AS-0.5 and IF-AS-1.3 according to TMS 402/602

| Specimen ID | $\lambda$ | $w$ (mm) |
|---|---|---|
| IF-AS-0.5 | 0.0027 | 122.3 |
| IF-AS-1.3 | 0.0025 | 197.3 |

The comparison results between experimental crack stiffness values and the stiffnesses obtained by TMS 402/602 are shown in Table 5.12. The code-to-experimental stiffness ratio is 0.8 and 2.0 for IF-AS-0.5 and IF-AS-1.3, respectively. The TMS 402/602 stiffness compares better with the experimental results than S304 values. This was attributed to the fact that TMS strut width was about ¼ of the S304 strut width and thus there was less overestimation in the stiffness prediction overall.

Table 5.12 Summary of comparison of TMS 402/602 and experimental crack stiffness

| Specimen ID | Test result | TMS 402/602 | $(k_{TMS}/k_{cr})$ |
|---|---|---|---|
| | $k_{cr}(kN/mm)$ | $k_{TMS}(kN/mm)$ | |
| IF-AS-0.5 | 43.4 | 38.5 | 0.8 |
| IF-AS-1.3 | 10.7 | 21.7 | 2.0 |

### 5.4.3 CSA S304.14 strength evaluation

Diagonal cracking, shear sliding, and corner crushing failure modes are considered by CSA S304.14 for infill strength calculation and the minimum of these three failure modes would be the masonry infill lateral strength. CSA S304.14 suggests the following equations for strength calculation of each mode:

(a) Diagonal cracking failure mode

$$V_r = \phi_m(v_m b_w d_v + 0.25P_d)\gamma_g \quad (5\text{-}6)$$

where $v_m$ is the resistance factor and is obtained from the below equation:

$$v_m = 0.16\sqrt{f'_m}\left(2 - \frac{M_f}{v_f d_v}\right) \quad (5\text{-}7)$$

The maximum value obtained from Eq. (5-6), must be less than the following equation.

$$0.4\,\phi_m\sqrt{f'_m}b_w d_v \gamma_g \quad (5\text{-}8)$$

where $V_r$ is the ultimate load; $\phi_m$ and $b_w$ are the resistance factor and the actual thickness of the web of the infill; $d_v$ is the effective depth of the infill; $P_d$ is the axial compressive load on the section under consideration; $\gamma_g$ is the factor to account for partially grouted or un-grouted walls constructed of hollow or semi-solid units; $M_f$ and $v_f$ are the factored moment and shear at the section considered.

(b) Sliding shear failure mode

Sliding shear capacity along bed joint is calculated as:

$$\mathrm{V}_r = 0.16\phi_m\sqrt{f'_m}A_{uc} + \phi_m\mu P_1 \quad (5\text{-}9)$$

where $A_{uc}$ is the un-cracked portion of the effective cross-sectional area providing shear bond capacity; μ is the coefficient of friction on the interface between the frame and infill (here taken 1 as is for masonry-to-masonry interaction); $P_1$ is the minimum compressive force acting normal to the sliding plane taken as $\frac{\mathrm{V}_r}{2}$ due to vertical component of compressive force of the diagonal strut.

(c) Corner crushing failure mode

The lateral strength corresponding to the corner crushing failure mode is calculated as follows:

$$V_r = \frac{l_m}{l_d} P_r \quad (5\text{-}10)$$

where $P_r$ is the factored compressive axial strength of strut:

$$P_r = \phi_m \chi \left(0.85 f'_m\right) w (t_e - r) \quad (5\text{-}11)$$

$$r = \left(\frac{t}{2} + e\right) - \frac{1}{2}\sqrt{t^2 + 4\,t\,e + 4e^2 - 16 e t_f} \quad (5\text{-}12)$$

$\chi$ is the factor to account for direction of compressive stress in a masonry member relative to the direction used for the determination of $f'_m$; $t_f$ is the thickness of the flange of the concrete masonry unit; $r$ is the radius of gyration; and e is the eccentricity of the load.

Table 5.13 summarizes the code-to-experiment strength ratio for IF-AS-0.5 and IF-AS-1.3 where analytical strengths for all three failure modes were calculated based on CSA S304. A sample calculation for specimen IF-AS-0.5 is included in Appendix C. It should be noted that the code equations calculate infill strength, not the infilled frame strength. Therefore, experimental results of the infill strength were calculated using CSI ETABS and considered in comparison with the code values. For infill strength, a braced model, created in CSI ETABS, was used for analysis where the experimental ultimate load of the infilled frame was applied to the model and the horizontal component of the axial load in the diagonal strut was taken as the experimental infill strength.

It can be seen in Table 5.13 the code equation performed differently for the two specimens. For IF-AS-0.5, the sliding shear equation provides the best strength estimate with a code-to-experiment strength ratio of 0.7 which is followed by the diagonal cracking value with a code-to-experiment strength ratio of 0.6. The corner crushing value overestimates the infill strength by 40%. These values seem to agree with the experimental observation where failure was governed by diagonal

cracking and shear failure and no corner crushing was observed. However, for IF-AS-1.3, all code equations seem to underestimate the strength at a much greater degree. The code-to-experiment strength ratios were determined to be 0.3 for both sliding shear and diagonal cracking. Noting that IF-AS-1.3 showed more flexural behaviour, it raises questions that whether the code equations developed mainly based on shear behaviour can be effective in a combined flexural and shear behaviour model for infilled frames.

Table 5.13 Comparison of experimental results and CSA S304.14 predicted ultimate strengths

| | Experimental results | | | CSA S304.14 | | | | | |
|---|---|---|---|---|---|---|---|---|---|
| Specimen ID | $P_{ult}$ (kN) | $P_{frame}$ (kN) | $P_{infill}$ (kN) | $P_{CSA-DC}$ (kN) | $P_{CSA-SS}$ (kN) | $P_{CSA-CC}$ (kN) | $P_{CSA-DC}/P_{infill}$ | $P_{CSA-SS}/P_{infill}$ | $P_{CSA-CC}/P_{infill}$ |
| IF-AS-0.5 | 173.1 | 82.6 | 90.5 | 60.2 | 68.9 | 129.0 | 0.6 | 0.7 | 1.4 |
| IF-AS-1.3 | 165.0 | 38.1 | 126.9 | 42.1 | 48.2 | 78.1 | 0.3 | 0.3 | 0.6 |
| | | | | | | Avg. | 0.4 | 0.5 | 1.0 |

### 5.4.4 TMS 402/602 strength evaluation

The lateral strength of masonry infills, according to TMS 402/602, is the minimum of three failure modes and they are corner crushing, sliding shear failure, and lateral drift at 25 mm.

For strength calculation based on corner crushing mode, TMS 402/602 proposed following equation:

$$V_r = (6.0\ inches) t_e f'_m \qquad (5\text{-}13)$$

And for strength calculation, by considering sliding shear failure mode, the bellow equations are suggested

$$V_r = \frac{V_n}{1.5}. \qquad (5\text{-}14)$$

$$V_n = min \begin{cases} 3.8\, A_{nv}\sqrt{f'_m} \\ 300\, A_{nv} \\ 56\, A_{nv} + 0.4 N_u \; if \; not \; fully \; grouted \\ 90\, A_{nv} + 0.45 N_u \; if \; fully \; grouted \end{cases} \quad (5\text{-}15)$$

where, $V_n$ is the nominal shear strength, and $N_u$ is the compressive force acting normal to shear surface.

For infill strength corresponding to 25 mm horizontal displacement of the frame, a braced model, with the specified strut width (calculated in Table 5.11), created in CSI ETABS, was used and analyzed under an in-plane lateral load which led to 25 mm frame lateral displacement and the horizontal component of the axial load in the diagonal strut was taken as the infill strength. A sample calculation is provided in Appendix C.

Table 5.14 summarizes the code-to-experiment strength ratio for IF-AS-0.5 and IF-AS-1.3 based on TMS. It shows that corner crushing failure mode provides the best strength estimate with a code-to-experiment strength ratio of 0.7 and a gross underestimation or overestimation of the specimen capacity if sliding shear or 25 mm lateral drift criteria are used.

Table 5.14 Comparison of experimental results and TMS 402/602 predicted ultimate strengths

| Specimen ID | Experimental results | | | TMS 402/602 | | | | | |
|---|---|---|---|---|---|---|---|---|---|
| | $P_{ult}$ (kN) | $P_{frame}$ (kN) | $P_{infill}$ (kN) | $P_{TMS-CC}$ (kN) | $P_{TMS-SS}$ (kN) | $P_{TMS-25}$ (kN) | $P_{CSA-CC}/P_{infill}$ | $P_{TMS-SS}/P_{infill}$ | $P_{TMS-25}/P_{infill}$ |
| IF-AS-0.5 | 173.1 | 82.6 | 90.5 | 87.1 | 20.0 | 486.2 | 0.9 | 0.2 | 5.3 |
| IF-AS-1.3 | 165.0 | 38.1 | 126.9 | 87.1 | 14.0 | 359.1 | 0.6 | 0.1 | 2.8 |
| | | | | | | Avg. | 0.7 | 0.1 | 4.0 |

# CHAPTER 6 SUMMARY AND CONCLUSIONS

## 6.1 SUMMARY

This experimental research was conducted to further investigate the in-plane behaviour of all-masonry infilled frames under lateral loading. The objective of the study was to augment the database of experimental results of all-masonry infilled frames and further assess their performance against masonry infilled RC frames. The parameters considered in the experimental program included infill aspect ratio, presence of vertical loading, and cyclic lateral loading. A total of six specimens were constructed and tested to failure, reflecting these parameters. All specimens were constructed of custom-made half-scale 200 mm concrete blocks for infills and the reinforced masonry frames consisted of 190x190 mm sections for the top beam and columns and a 250x250 mm section for the RC base beam.

For all specimens, load vs. lateral displacement response, cracking pattern, failure mode, and crack and ultimate loads were obtained and presented. The stiffness and ductility were calculated and discussed. These performance indicators of all-masonry infilled frames were also compared with those obtained in previous studies on all-masonry infilled frames and masonry infilled RC frames. Finally, the experimental results were used to evaluate the applicability of the analytical methods provided by CSA S304.14 and TMS 402/602-16 on all-masonry infilled frames.

## 6.2 CONCLUSIONS

The following conclusions were drawn from this study:

Effect of vertical loading

Presence of vertical loading resulted in a significant increase in both cracking and ultimate loads as well as the stiffness including initial and cracking stiffness of all-masonry infilled specimens. However, less displacement was sustained at ultimate, indicating a lower ductility than the control specimen. For a given vertical load level, the application methods seemed to impact the lateral behaviour and the degree of the strength increase. When applied through the frame top beam, the vertical load resulted in a greater increase in the lateral strength of the specimen than when applied through the frame columns. However, the former application method led to a more brittle failure accompanied by a sudden load drop while the latter application maintained more or less ductile behaviour, albeit at a lesser degree than the control specimen. In both cases, the failure was governed by diagonal cracking while the specimen with vertical load applied through frame columns showed more extensive cracking.

Effect of aspect ratio

As the infill aspect ratio increased, i.e., the infill became increasingly slender, the stiffness of infilled frames decreased, and the specimens exhibited an increasingly ductile behaviour. In terms of lateral strength, the overall geometry of the specimen was a more deciding factor than the aspect ratio alone. If the overall geometry and dimensions of specimens yield a similar diagonal strut length, the lateral strength of these specimens remained similar despite their aspect ratios were very different. It is cautioned that this was only valid if the failure was controlled by diagonal cracking. The specimen with the high aspect ratio (slender) showed more flexural behaviour while

the specimen with the low aspect ratio (squat) showed more shear behaviour. The difference in behaviour affected more in stiffness but less in lateral strength. It suggests that in the case of infilled frame, the lateral strength is predominately controlled by shear behaviour.

Effect of interfacial gap and cyclic loading

For a given gap size, the gap location also played an important role in the lateral behaviour and strength of all-masonry infilled frames. When comparing infill-to-column gap (side gap) and infill-to-beam gap (top gap), the former resulted in lower stiffness but greater lateral strength than the latter. It seems to suggest that the side gap has a greater impact on stiffness and thus displacement than strength while the top gap is more detrimental to the lateral strength. A comparison with their infilled RC frame counterparts showed all-masonry infilled frame behaved similarly under cyclic loading. The stiffness degradation, ductility and backbone characteristics of all-masonry infilled frames were all comparable to the infilled RC frames.

CSA S304.14 and TMS 402/602 evaluation

In general, the applicability of the code equations to the all-masonry infilled frames is similar to the infilled RC frames. For the stiffness prediction, it was observed that CSA S304-14 overestimates the stiffness while TMS 402/602-16 seems to provide a better estimate. However, for the specimen of a high aspect ratio, neither code values compared well with the experimental result. It seems to suggest that when the flexural behaviour is becoming pronounced in the overall behaviour, the validity of the stiffness equation based on a braced frame analogy needs to be evaluated. For the strength prediction, the CSA S304.14 provided reasonably conservatism estimates for a shear-behaviour dominated specimen but does not perform well for a system failed by combined flexural and shear behaviour. TMS 402/602 does not have diagonal cracking as a failure mode but its corner crushing equation yielded the values closet to the experimental results.

Overall, both standards seem to be inadequate in providing strength estimate that reflects the test results.

## 6.3 RECOMMENDATIONS FOR FUTURE RESEARCH

Since the all-masonry infilled frame is a new form of the infilled frame, more tests need to be conducted to include material, geometric, and loading parameters to have a thorough evaluation of the performance of the system. The following recommendations are provided for future work.

Loading parameters

In the case of presence of vertical loading, more vertical load levels and application methods should be investigated to establish a correlation between the level of the load and the frame strength and failure mode.

The in-plane lateral loading behaviour has been established to some degree. It is also important to investigate the out-of-plane loading behaviour of this type of infilled frames.

Cyclic loading studies on more specimens are also in need to fully assess the performance of all-masonry infilled frames against other type of infilled frames.

Geometric parameters

More tests should be carried out to investigate the relative stiffness effect of the lateral behaviour of all-masonry infilled frames. These can include more variations in aspect ratio to introduce higher degree of flexural behaviour, and different cross-sectional properties of both the infill and the frame.

Construction parameters

Under construction parameter consideration, the simultaneous construction of the infill and frame lend to possibility of grouting and reinforcing (vertical) the infill. This aspect of infill construction can be included in the further study.

# REFERENCES


Al-Chaar, G. (2002). Evaluating Strength and Stiffness of Unreinforced Masonry Infill Structures. *Journal of Structural Engineering*, ASCE, 128(8):1055-1063.

Al-Nimry, H. (2014). Quasi-Static Testing of RC Infilled Frames and Confined Stone-Concrete Bearing Walls. *Journal of Earthquake Engineering*, 18(1):1-23.

American Society of Civil Engineers (ASCE) (2017). Seismic Evaluation and Retrofit of Existing Buildings. ASCE/SEI 41-17, Reston, Virginia.

Asteris, P.G., Cotsovos, D.M., Chrysostomou, C.Z., Mohebkhah, A., and Al-Chaar, G.K. (2013). Mathematical Micro modeling of Infilled Frames: State of the Art. *Engineering Structures,* 56:1905-1921.

ASTM A951/A951M-16e1 (2016). Standard Specification for Steel Wire for Masonry Joint Reinforcement. West Conshohocken, PA.

ASTM C1019-18e1 (2018). Standard Test Method for Sampling and Testing Grout. West Conshohocken, PA.

ASTM C1314-16 (2016). Standard Test Method for Compressive Strength of Masonry Prisms. West Conshohocken, PA.

ASTM C140/C140M-18a (2018). Standard Test Methods for Sampling and Testing Concrete Masonry Units and Related Units. West Conshohocken, PA.

ASTM C143/C143M-15a (2015). Standard Test Method for Slump of Hydraulic-Cement Concrete. West Conshohocken, PA.

ASTM C270-14 (2014). Standard Specification for Mortar for Unit Masonry. West Conshohocken, PA.

ASTM C39/C39M-16a (2016). Standard Test Method for Compressive Strength of Cylindrical Concrete Specimens. West Conshohocken, PA.

ASTM C39/C39M-18 (2018). Standard Test Method for Compressive Strength of Cylindrical Concrete Specimens. West Conshohocken, PA.

ASTM C476-18 (2018). Standard Specification for Grout for Masonry. West Conshohocken, PA.

ASTM E8/E8M-16a (2016). Standard Test Methods for Tension Testing of Metallic Materials. West Conshohocken, PA.

ATC-24 (1994). Guidelines for Cyclic Seismic Testing of Components of Steel Structures. *Applied Technology Council.* Redwood City, CA.

Burton, H., Deierlein, G. (2014). Simulation of Seismic Collapse in Non-Ductile Reinforced Concrete Frame Buildings with Masonry Infills. *Journal of Structural Engineering*, 40(8).

CSA S304-14 (2014). Design of Masonry Structures. *Canadian Standard Association*. Mississauga, ON, Canada.

Crisafulli, F.J., and Carr, A.J. (2007). Proposed Macro-Model for the Analysis of Infilled Frame Structures. Bulletin of the New Zealand Society for Earthquake Engineering. 40(2): 69-77.

Dawe, J., and Seah, C. (1989a). Behaviour of Masonry Infilled Steel Frames. *Canadian Journal of Civil Engineering*, 16(6): 865-876.

Dawe, J.L., and Seah, C.K. (1989). Behaviour of Masonry Infilled Steel Frames. *Canadian Journal of Civil Engineering*, 16(6): 865–876.

Drysdale, R.G., and Hamid, A.A. (2005). Masonry Structures: Behavior and Design. *Canadian Masonry Design Centre,* Mississauga, Ontario.

El-Dakhakhni, W.W. (2002). Experimental and Analytical Seismic Evaluation of Concrete Masonry-Infilled Steel Frames Retrofitted Using GFRP Laminates. Ph.D. Dissertation, Drexel University.

El-Dakhakhni, W.W., Elgaaly, M. and Hamid, A.A. (2003). Three-Strut Model for Concrete Masonry-Infilled Steel Frames. *ASCE Journal of Structural Engineering*, 129(2):177–185.

Flanagan, R. D., and Bennett, R. M. (1999). In-Plane Behavior of Structural Clay Tile Infilled Frames. *Journal of Structural Engineering*, ASCE, 125(6):590-599.

Flanagan, R.D. (1994). Behavior of Structural Clay Tile Infilled Frames. *Oak Ridge National Lab.*, TN (United States).

Foroushani, S.A. (2019). Experimental Investigation of the In-Plane Behaviour of Concrete Masonry Infills Bounded by Masonry Frames. Civil and Resource Engineering, Dalhousie University, Halifax, N.S.

Hendry, A.W. (1998). Structural Masonry. 2nd ed. Macmillan Press, London.

Holmes, M. (1961). Steel Frames with Brickwork and Concrete Infilling. *Proceedings of the Institution of Civil Engineers,* 19(4): 473-478.

Hu C. (2015). Experimental Study of the Effect of Interfacial Gaps on the In-Plane Behaviour of Masonry Infilled RC Frames. MASc thesis, Dalhousie University, Halifax, Canada.

Kakaletsis, D., and Karayannis, C. (2007). Experimental Investigation of Infilled R/C Frames with Eccentric Openings. *Structural Engineering and Mechanics*, 26(3): 231-250.

Klinger, R.E. and Bertero, V.V. (1976). Infilled Frames in Earthquake-Resistant Construction. EERC Report UBC/EERC-76/32, UC Berkley, Berkley, CA.

Klingner, R., Rubiano, N., Bashandy, T., and Sweeney, S. (1996). Evaluation and Analytical Verification of Shaking Table Data from Infilled Frames. Part 2: Out-of-Plane Behavior, 521-532.

Mainstone, R. J. (1971). On the Stiffness and Strengths of Infilled Frames. *Proceedings of the Institute of Civil Engineers*, Suppl. (4):57–90.

Mallick, D., and Garg, R. (1971). Effect of Openings on the Lateral Stiffness of Infilled Frames. *Proceedings of the Institution of Civil Engineers,* 49(2): 193-209.

Mehrabi, A. B., Shing, P. B., Schuller, M. P., and Noland, J. L. (1996). Experimental Evaluation of Masonry-Infilled RC Frames. *Journal of Structural Engineering*, ASCE, 122(3):228-237.

Mehrabi, A. B., Shing, P. B., Schuller, M. P., and Noland, J. L. (1994). Performance of Masonry Infilled Frames R/C Frames Under In-Plane Lateral Loads. *Report CU/SR-94/6*. University of Colorado, Boulder.

Mehrabi, A.B., Benson Shing, P., Schuller, M.P., and Noland, J.L. (1996). Experimental Evaluation of Masonry-Infilled RC Frames. *Journal of Structural Engineering*, 122(3): 228-237.

Mosalam, K. H. (1996). Experimental and Computational Strategies for the Seismic Behaviour Evaluation of Frames with Infill Walls. Ph.D. dissertation, Cornell University, Ithaca, New York.

NBCC (2015). National building code of Canada. Institute for Research in Construction, NRCC, Ottawa, Ontario.

Paulay, T., and Priestley, M. J. N. (1992). Seismic Design of Reinforced Concrete and Masonry Buildings, Wiley New York.

Polyakov, S. V. (1956). Masonry in Framed Buildings (An investigation into the strength and stiffness of masonry infilling). Gosudarstvennoe izdatel'stvo Literatury po stroitel'stvu iarkhitekture, Moscow. (English translation by G. L. Cairns, National Lending Library for Science and Technology, Boston, Yorkshire, England, 1963).

Pujol, S., and Fick, D. (2010). The Test of a Full-Scale Three-Story RC Structure with Masonry Infill Walls. *Engineering Structures***,** 32(10): 3112-3121.

Rosenblueth, E. (1980). Design of Earthquake Resistant Structures. *Pentech Press Limited*, 195-222.

Saneinejad, A., and Hobbs, B. (1995). Inelastic Design of Infilled Frames. *Journal of Structural Engineering*, 121(4), 634-650.

Soon, S. (2011). In-Plane Behaviour and Capacity of Concrete Masonry Infills Bounded by Steel Frames, *Civil and resource engineering*, Dalhousie university, Halifax.

Stafford-Smith, B., and Carter, C. (1969). A Method of Analysis for Infilled Frames. *Proceedings of the Institution of Civil Engineers*, 44(1):31-48.

Stafford-Smith, B., and Coull, A. (1991). Tall Building Structures: Analysis and Design. Wiley-Inter science.

Steeves, R. (2017). In-Plane Behaviour of Masonry Infilled RC Frames with Interfacial Gaps Subjected to Quasi-Static Loading. MASc Thesis, Civil and Resource Engineering Department, Dalhousie University, Halifax, Canada.

TMS 402/602 (2016). Building Code Requirements and Specifications for Masonry Structures. *Concrete International*.

Yong, T.C. (1984). Shear Strength of Masonry Infilled Panel in Steel Frames. MSc thesis, University of New Brunswick, Fredericton, Canada.

# APPENDIX A AUXILIARY TESTS

The auxiliary tests were performed to obtain the material properties of CMUs, mortar, grout, masonry prisms, concrete, and reinforcing steel. The test setup and procedures of above-mentioned tests are described in the following sections.

## A.1 CMUs

Compressive strength and physical properties of masonry infill CMUs obtained in accordance with ASTM C140/C1140M (2018) “Standard Test Methods for Sampling and Testing Concrete Masonry Units and Related Units”. To indicate the compressive strength of masonry infill CMUs properly, a random selection from the CMUs batch was made. Moisture content, density and 24-hour percentage absorption were achieved for physical properties. To obtain Compressive strength the block was placed in Instron Universal testing machine as shown in Figure A.1.

(a)

(b)

Figure A.1 Compression test setup for CMUs., (a) Boundary block (b) Infills block

## A.2 Mortar

For all specimens, one mortar mix was used. The mortar mix was Type S, where Portland cement, Type N masonry cement, and sand were mixed with a weight ratio of 1:4:15 in accordance with ASTM C270 (2014) Standard Specification for Mortar for Unit Masonry. During the construction

of specimens, a total of 8 mortar cubes were cast from different batches. The samples were moist-cured for 14 days and then air-cured until the day that the corresponding specimen was tested (Figure A.2).

Figure A.2 Mortar samples under compression test

## A.3 Grout

Grout mix design was 1:3 for Portland cement and sand, respectively. This mix design was according to ASTM C476 (2018) Standard Specification for Grout for Masonry. To obtain the compressive strength of specimens a total of 15 samples were randomly cast from different batches in accordance with ASTM C1019 (2018) Standard Test Method for Sampling and Testing Grout, as illustrated in Figure A.3. All samples were moist-cured for seven days and then were air-cured

before the testing. Compressive strength of grout samples was tested by Instron universal testing machine as seen in Figure A.4.

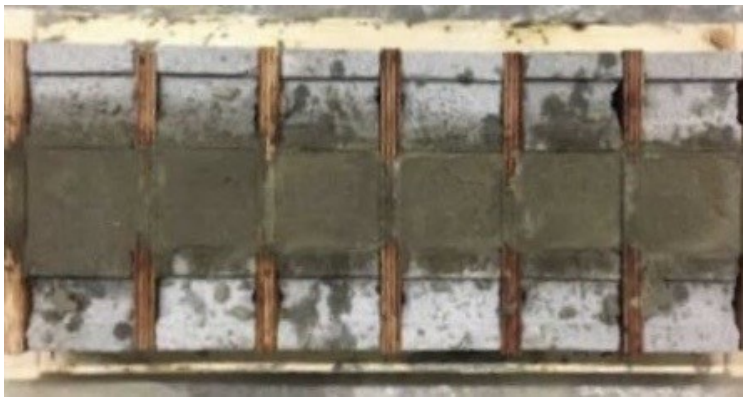

Figure A.3 Grout sampling

Figure A.4 Grout samples for compression test

## A.4 Masonry prism

Column and infilled masonry prisms were constructed according to ASTM C1314 (2016) Standard Test Method for Masonry Prisms. Three column and five infilled masonry prisms were constructed in total. All prisms were 5-course high and constructed in the same manner as the specimen. After construction of prisms, they were cured in the same condition as the specimen until the day of testing. In order to obtain the compressive strength, the prisms were tested in Instron Universal machine while the prisms were capped with fiberboard on loading surfaces (Figure A.5).

(a) Column prism (b)Infilled prism

Figure A.5 Column and infilled capped prism samples in the Instron machine

## A.5 Concrete cylinders

To determine the modulus of elasticity and compressive strength of concrete six 100 by 200 mm and three 150 by 300 mm concrete cylinders were cast besides casting the base beams of all specimens (Figure A.6). To obtain the 28-day compressive strength of the concrete, the smaller samples were tested after curing for 28 days in a moisture room. The large cylinders were moist-cured in the moisture room for 28 days and after being air-cured in the same condition as the specimens, they were tested at the day of specimen testing (Figure A.7). All the testing procedures including sampling, curing, and testing procedure were in accordance with ASTM C39/C39M (2018) Standard Test Method for Compressive Strength of Cylindrical Concrete Specimens.

Figure A.6 Concrete cylinder

Figure A.7 Compression test setup for concrete cylinder

## A.6 Reinforcement

The reinforcement used in this project was from the same batch as used by a previous colleague in our research group (Hu 2015), therefore, the material properties of steel reinforcement was obtained from that study. To determine modulus of elasticity and strength, three 10M longitudinal rebars were randomly selected and three coupons were cut. For testing the reinforcing coupons, Instron Universal testing machine was used. Details of the used coupons are shown in Figure A.8. To determine the stress-strain relationship an extensometer was installed on the coupon to obtain the strain during the loading history (Figure A.9). All the testing procedures were conducted in

accordance with ASTM E8 (2008) Standard Test Methods for Tension Testing of Metallic Materials.

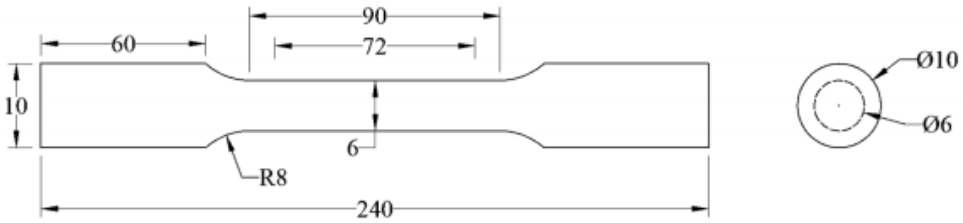


Figure A.8 Steel coupon detailing (Hu 2015)


Figure A.9 Tension test set-up for steel coupons (Hu 2015)

# APPENDIX B RESULTS OF AUXILLARY TESTS

## B.1 CMUs

Since CMUs used in this study was from the same batch as used in a previous experimental study by Foroushani (2019), the physical properties of CMUs were collected from that study. However, the compressive strength of the CMUs was determined in this study. All the testing procedures were according to ASTM C140/C140M (2018).

## B.2 Physical properties of CMUs

To determine the physical properties of CMUs including the density, net, and gross area, 24-hour absorption rate, and moisture content a random selection of 12 CMUs from different batches was conducted by Forushani (2019). From the total of 12 CMUs tested by Forushani (2019) at least 9 of them were from the same batch as used in this study. At the beginning, the weight of each block was determined. Then the CMU block was submerged in the water and the immersed weight was measured afterwards. The specimen was kept in the water and was removed from the water in 24 hours. After being surface dried using a towel, the saturated weight was measured. Next, the CMU block was oven dried at 100°C for 24 hours and the dry weight was recorded. CAN/CSA A165 Standard for Masonry Units indicates that a standard 200 mm hollow blocks shall have a "density greater than 2000 kg/m3 , moisture content below 45% at a relative humidity of above 75%, the CV of sample results less than 15%, and an absorption less than 175 kg/m3". Table B.1 summarizes the physical properties measured for the concrete blocks by Foroushani (2019). Except the density of blocks which was less than 2000 kg/m3, other physical properties satisfied the requirement of the code for a standard 200 mm block. According to Foroushani (2019), the lower density of CMUs had no effect on the strength results of the previous project.

Table B.1 CMUs physical properties

| CMUs | Absorption % | | Moisture content % | | Density Kg/m$^3$ | |
|---|---|---|---|---|---|---|
| | Avg. | CV (%) | Avg. | CV (%) | Avg. | CV (%) |
| Standard stretcher | 6.3 | 6.7 | 13.5 | 14.2 | 1657.6 | 0.4 |
| Half blocks | 5.2 | 11.4 | 21.7 | 8.5 | 1639.3 | 0.8 |
| Boundary | 6.2 | 5.5 | 23 | 13.3 | 1651.5 | 0.1 |

## B.3 Mechanical properties of CMUs

The net area of infill block and boundary block are considered as 8390 mm2 and 26883 mm2, respectively to calculate the compressive strength. Table B.2 illustrates compressive strength of stretcher and boundary CMUs and Figure B.1 exhibit typical failure modes of both infill block and boundary block.

Table B.2 Mechanical properties of CMUs

| CMUs | ID | Net area (mm$^2$) | Compressive capacity | | Avg. (MPa) | CV (%) |
|---|---|---|---|---|---|---|
| | | | Load (kN) | Strength (MPa) | | |
| Standard Stretcher | S1 | 8390 | 177.3 | 21.1 | 17.9 | 27 |
| | S2 | 8390 | 140.1 | 16.7 | | |
| | S3 | 8390 | 134.1 | 16.0 | | |
| Boundary | B1 | 26883 | 414.4 | 15.4 | 17.7 | 10.2 |
| | B2 | 26883 | 533.1 | 19.8 | | |
| | B3 | 26883 | 482.6 | 17.9 | | |

(a) Boundary block

(b) Infills block

Figure B.1 Typical failure mode of CMUs

## B.4 Mortar

One mortar mix was used in constructing specimens. Table B.3 shows the results obtained from compressive strength tests of mortar cubes. Figure B.2 illustrates a typical failure mode of mortar cubes.

Table B.3 Mortar sample strength

| Mortar cubes number | Compressive strength (MPa) | Avg. (MPa) | CV (%) |
|---|---|---|---|
| 1 | 15.7 | 16.9 | 14.5 |
| 2 | 14.6 | | |
| 3 | 14.9 | | |
| 4 | 16.1 | | |
| 5 | 15.1 | | |
| 6 | 17.7 | | |
| 7 | 21.6 | | |
| 8 | 19.2 | | |

Figure B.2 Typical failure mode for mortar samples

## B.5 Grout

To grout all specimens' columns and top beams a total of 11 grout batches were used. Table B.4 presents the grout strength for different batches. The average compressive strength for grout specimens was calculated to be 20 MPa with a CV of 4.6%. The failure pattern of grout is also shown in Figure B.3.

Figure B.3 Grout sample failure mode

Table B.4 Grout compressive strength (Foroushani, 2019)

| Grout batch number | Grout batch strength (MPa) | Avg. (MPa) | CV (%) |
|---|---|---|---|
| 1 | 20.1 | 20.0 | 4.6 |
| 2 | 20.7 | | |
| 3 | 17.2 | | |
| 4 | 20.1 | | |
| 5 | 20.7 | | |
| 6 | 20.2 | | |
| 7 | 19.1 | | |
| 8 | 18.1 | | |
| 9 | 23.0 | | |
| 10 | 19.4 | | |
| 11 | 20.4 | | |

## B.6 Masonry prisms

The net area of column masonry prism was calculated to be 36100 $mm^2$ and the face-shell area of the infilled masonry prism shown in Figure B.4 which was determined to be 8642 $mm^2$. The compressive strength of masonry prisms is presented in Table B.5. The average compressive

strength for infilled masonry prisms and column masonry prisms were 16.1 MPa and 14.6 MPa respectively. The failure mode for both infilled and column masonry prisms is illustrated in Figure B.5.

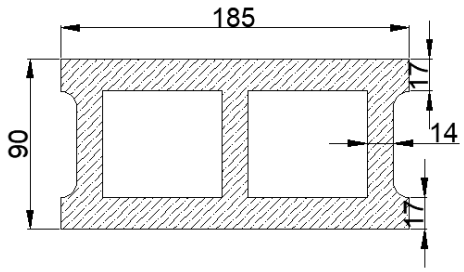


Figure B.4 Effective cross sectional area of infilled masonry prisms

Table B.5 Compressive strength of masonry prisms

| masonry prism | ID | Ultimate load (kN) | $f'_m$ (MPa) | Avg. (MPa) | CV (%) |
|---|---|---|---|---|---|
| Infilled masonry prisms | I1 | 122.5 | 14.1 | 16.1 | 6.5 |
| | I2 | 145.3 | 16.8 | | |
| | I3 | 138.5 | 16.0 | | |
| | I4 | 146.0 | 16.8 | | |
| | I5 | 145.4 | 16.8 | | |
| Column masonry prism | C1 | 389.3 | 10.8 | 14.6 | 26 |
| | C2 | 533.5 | 14.8 | | |
| | C3 | 665.2 | 18.4 | | |

(a) Infilled prism

(b) Column prism

Figure B.5 Failure mode of masonry prisms

## B.7 Concrete cylinder

All the base beams were cast at the same time using the same batch. The concrete samples were tested at 28 days and the day of testing to determine compressive strength. The results of compression test are presented in Table B.6. The typical failure pattern of cylinders is illustrated in Figure B.6.

Table B.6 Concrete cylinder compression test results

| Specimen ID | Ultimate load (kN) | Compressive strength (MPa) | Avg. (MPa) | CV (%) |
|---|---|---|---|---|
| S1 | 191.2 | 24.3 | 23.9 | 4.2 |
| S2 | 182.3 | 23.2 | | |
| S3 | 195.7 | 24.9 | | |
| S4 | 177.9 | 22.6 | | |
| S5 | 182.3 | 23.2 | | |
| S6 | 200.1 | 25.4 | | |
| L1 | 688.6 | 39.0 | 37.3 | 4.5 |
| L2 | 669.4 | 37.9 | | |
| L3 | 618.1 | 35.0 | | |

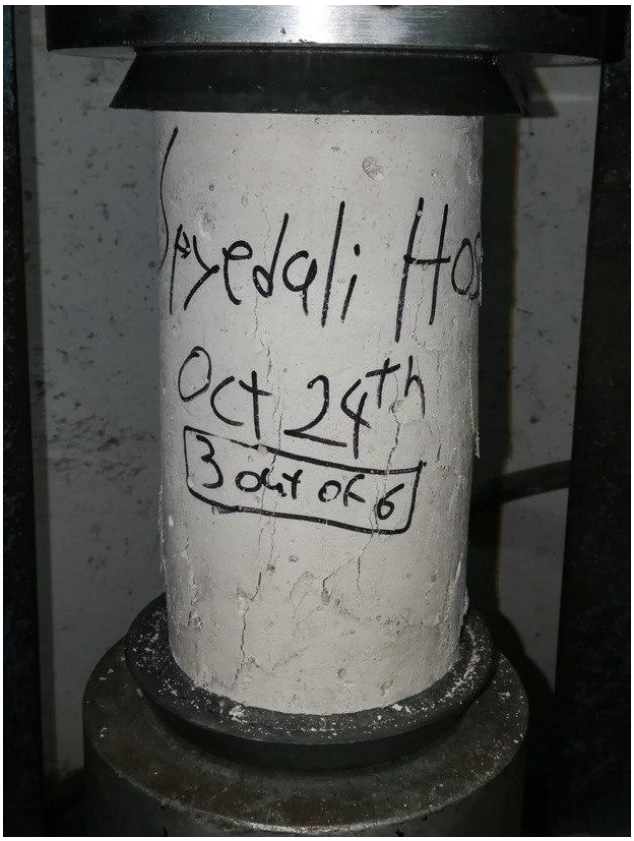


Figure B.6 Concrete cylinders failure pattern

## B.8 Summary of auxiliary test results

The mechanical properties of steel reinforcement including the yield stress and ultimate stress were collected from a previous study conducted by Hu (2015). The collected steel reinforcement and grout data and other auxiliary test results conducted in this study are summarised in Table B.7.

Table B.7 Summary of auxiliary test results

| Component | | Strength (MPa) |
|---|---|---|
| Infill CMUs | | 17.9 |
| Boundary CMUs | | `17.7 |
| Mortar | | 16.9 |
| Grout | | 20.0 |
| Column masonry prism | | 14.6 |
| Infilled masonry prism | | 16.1 |
| Small concrete cylinder (28 days) | | 23.9 |
| Large concrete cylinder (Day of specimen testing) | | 37.3 |
| Reinforcement (Hu 2015) | Yield strength | 446 |
| | Ultimate strength | 665 |

# APPENDIX C SAMPLE CALCULATIONS FOR DESIGN STRENGTH AND STIFFNESS

In this section, sample calculations for specimen IF-AS-0.5 is shown as an example. This specimen is depicted in Figure C.1 and its geometric and mechanical properties are as follows:

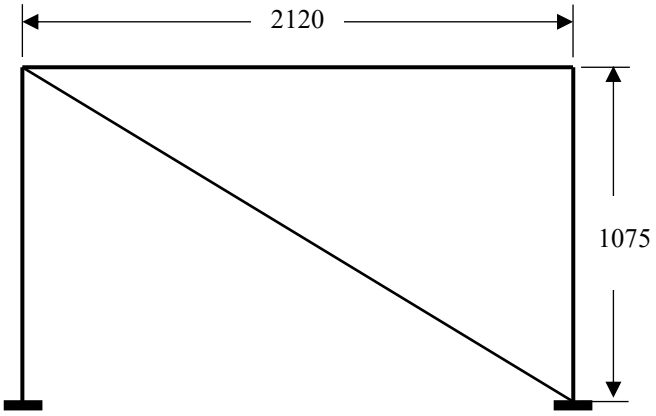


Figure C.1 Specimen IF-AS-0.5

Reinforced masonry frame:

$l_b = 2120\ mm,\ \ h_c = 1075\ mm$

$I_b = I_c = 108.6 * 10^6\ mm^4$

$$E_b = E_c = E_f = \frac{A_{block}E_{block} + A_{grout}E_{grout}}{A_{block} + A_{grout}} = 17.7 * 850 * 0.463 + 20 * 850 * 0.537$$

$$= 16094.8\ MPa$$

Masonry infill:

$l_m = 1930\ mm,\ \ h_m = 980\ mm,\ \ \theta = \tan^{-1}\left(\frac{h_m}{l_m}\right) = 0.47\ rad$

$b_w = 90\ mm, \qquad t_e = 34\ mm$

$f'_m = 16.8\,MPa, \qquad E_m = 850 f'_m = 14280\,MPa$

## C.1 CSA S304.14 stiffness evaluation

According to CSA S304.14, equivalent strut width can be estimated as:

$$w_{eff} = \frac{1}{2}\sqrt{{\alpha_h}^2 + {\alpha_l}^2} = \frac{1}{2}\sqrt{571.2^2 + 1353.2^2} = 734.4\,mm$$

Where

$$\alpha_h = \frac{\pi}{2}\sqrt[4]{\frac{4E_f I_c h_m}{E_m t_e \sin(2\theta)}} = \frac{\pi}{2}\sqrt[4]{\frac{4 * 16094.8 * 108.6e6 * 980}{14280 * 34 * \sin(2 * 0.47)}} = 571.2\,mm$$

$$\alpha_l = \pi\sqrt[4]{\frac{4E_f I_b l_m}{E_m t_e \sin(2\theta)}} = \pi\sqrt[4]{\frac{4 * 16094.8 * 108.6e6 * 1930}{14280 * 34 * \sin(2 * 0.47)}} = 1353.2\,mm$$

For evaluating stiffness based on strut width, CSA S340.14 mentioned that half of $w_{eff}$ must be used, while it is not greater than the quarter of infill diagonal length ($l_d$).

$$\frac{w_{eff}}{2} = 367.2\,mm < \frac{l_d}{4} = \frac{\sqrt{{h_m}^2 + {l_m}^2}}{4} = 541.1\,mm$$

Therefore $\frac{w_{eff}}{2} = 367.2\,mm$ is used for stiffness evaluation. This specimen was modeled in Etabs software as shown in Figure C.1 with an equivalent diagonal struth with 367.2 mm width and 34 mm thickness to represent the masonry infill. This model was linearly analyzed under 1 kN lateral point load on the level of top beam and its corresponding lateral displacement was observed equal to 0.012 mm. So, the specimen stiffness would be equal to $k = \frac{1\,kN}{\Delta} = 83.3\,\frac{kN}{mm}$.

## C.2 TMS 402/602-16 stiffness evaluation

According to TMS 402, the width of equivalent strut can be calculated using following equations:

$$w = \frac{0.3}{\lambda \cos\theta} = \frac{0.3}{\lambda \cos\theta} = \frac{0.3}{0.0027 * cos\, 0.47} = 122.3\, mm$$

where

$$\lambda = \sqrt[4]{\frac{E_m t_e \sin 2\theta}{4E_f I_c h_m}} = \sqrt[4]{\frac{14280 * 34 * \sin(2 * 0.47)}{4 * 16094.8 * 108.6e6 * 980}} = 0.0027$$

An Etabs braced model with strut width of 122.3 mm created and linearly analyzed. TMS 402 model showed 0.026 mm displacement under 1kN lateral load. Therefore, stiffness according to TMS 402 is 38.5 kN/mm.

## C.3 CSA S304.14 strength evaluation

According to CSA S304.14, masonry infill lateral strength is the minimum of diagonal cracking, shear sliding, and corner crushing strength of the infill.

**1- Diagonal cracking strength**

$$V_r = \phi_m(v_m b_w d_v + 0.25P_d)\gamma_g \leq 0.4\, \phi_m \sqrt{f'_m} b_w d_v \gamma_g$$

$$V_r = 1.0(1.148 * 90 * 1544 + 0.25 * 0) * 0.378 = 60.30\, kN$$

$$\leq 0.4 * 1 * \sqrt{16.8} * 90 * 1544 * 0.378 = 86.11\, kN$$

where

$$\phi_m = 1.0 \;\; to\ compare\ with\ the\ raw\ experimental\ data$$

$b_w = 90\ mm$

$d_v = 0.8 l_m = 0.8 * 1930 = 1544\ mm$

$v_m = 0.16\sqrt{f'_m}\left(2 - \frac{M_f}{v_f d_v}\right) = 0.16 * \sqrt{16.8}(2 - 0.25) = 1.148\ MPa$

$P_d = 0\ as\ self\ weight\ is\ negligible$

$\gamma_g = \frac{34}{90} = 0.378\ \ effective\ mortared\ area$

**2- Shear sliding strength**

$\mathrm{V}_r = 0.16\phi_m\sqrt{f'_m}A_{uc} + \phi_m\mu P_1 = 0.16 * 1 * \sqrt{16.8} * 52496 + 1 * 1 * \frac{\mathrm{V}_r}{2}$

$\mathrm{V}_r = 68.85\ kN$

where

$A_{uc} = 0.8 l_m t_e = 0.8 * 1930 * 34 = 52496\ mm^2$

$\mu = 1.0\ for\ masonry\ to\ masonry\ sliding\ friction$

$P_1 = \frac{\mathrm{V}_r}{2}\ due\ to\ vertical\ component\ of\ diagonal\ compression\ force$

**3- Corner crushing strength**

According to CSA S304, compressive capacity of the diagonal strut must be considered along with slenderness of the strut length which is

$\frac{kl}{t} = \frac{0.9\left(l_d - \frac{w}{2}\right)}{t} = 0.9 * \frac{1817.3}{90} = 18.17 < 30 \quad No\ reinforcing\ is\ required$

where

$l = l_d - \frac{w}{2} = \sqrt{980^2 + 1930^2} - \frac{734.4}{2} = 1797.8\ mm$

Compressive strength of strut with a minimum eccentricity of 0.1t:

$$P_r = \phi_m \chi \left(0.85 f'_m\right) w (t_e - r) = 1.0 * 0.5 * 16.8 * 734.4 * (34 - 6) = 146.8\ kN$$

where

$$r = \left(\frac{t}{2} + e\right) - \frac{1}{2}\sqrt{t^2 + 4\ t\ e + 4e^2 - 16 e t_f} = \left(\frac{90}{2} + 0.1 * 90\right) -$$

$$\frac{1}{2}\sqrt{90^2 + 4 * 90 * 0.1 * 90 + 4(0.1 * 90)^2 - 16(0.1 * 90) * 17} = 6\ mm$$ first trial to find eccentricity.

The magnified moment based on slenderness is:

$$M_{ftot} = P_r e \left( \frac{C_m}{1 - \frac{P_f}{P_{cr}}} \right) = P_f e'$$

where

$$C_m = 1\ for\ minimum\ eccentricity$$

$$P_{cr} = \frac{\pi^2 \phi_e (EI)_{eff}}{(kh)^2 (1 + 0.5\beta_d)} = \frac{\pi^2 * 1 * 1.93 * 10^{11}}{(0.9 * 1075)^2 (1 + 0.5 * 0)} = 2039.7\ kN$$

and

$$(EI)_{eff} = 0.4 E_m I_o = 0.4 * 850 * 16.8 * 3.39 * 10^7 = 1.93 * 10^{11}\ N.mm^2$$

$$I_o = \frac{1}{12}\ w\ t_e^3 = \frac{1}{12}\ 734.4 * (90^3 - (90 - 34)^3) = 3.39 * 10^7 mm^4$$

$$k = 0.9\ effective\ length\ (CSA\ S304)$$

$$\beta_d = 0\ temporary\ loading$$

$e' = \frac{1}{1 - \frac{P_r}{P_{cr}}} e = \frac{1}{1 - \frac{146.8}{2039.7}} 0.1 * 90$ =9.7 mm, second trial to estimate eccentricity

Therefore, r and $P_r$ will be calculated based on this eccentricity ($e = e'$). Then, $e'$ is obtained again and this process continues as the value of eccentricity converges.

The converged values are:

$e = 9.687\ mm$

$P_r = 144.74\ kN\ compressive\ strength\ of\ strut$

Therefore, horizontal strength of infill based on corner crushing is:

$$P_{cc} = \frac{l_m}{l_d} P_r = \frac{1930}{2164.5} 144.74 = 129.0\ kN$$

## C.4 TMS 402/602-16 strength evaluation

Lateral strength of masonry infill, based on TMS 402/602-16, is the minimum of corner crushing, sliding shear failure, and the strength corresponding to 25 mm lateral displacement.

**1- Corner crushing**

$$V_r = (6.0\ inches) t_e f'_m = 6 * 25.4 * 34 * 16.8 = 87.05\ kN$$

**2- Sliding shear failure**

$$V_r = \frac{V_n}{1.5}$$

where

$$V_n = min \begin{cases} 3.8\ A_{nv} \sqrt{f'_m} \\ 300\ A_{nv} \\ 56\ A_{nv} + 0.4 N_u\ if\ not\ fully\ grouted \\ 90\ A_{nv} + 0.45 N_u\ if\ fully\ grouted \end{cases}$$

and

$N_u = 0.81V_n$ *Normal compressive force acting on shear surfaces*

$A_{nv} = 0.8\, l_m t_e = 0.8 * 1930 * 34 = 52496\, mm^2 = 81.37\, in^2$

The minimum of above equations is

$$V_n = min \begin{cases} 3.8 * 81.37\sqrt{16.8 * 145.04} = 15.26\, kips \\ 300\, A_{nv} = 300 * 81.37 = 24.41\, kips \\ 56\, A_{nv} + 0.4N_u = 56 * 81.37 + 0.4 * 0.81 * V_n : \; V_n = 6.74\, kips \\ NA \end{cases}$$

$V_n = 6.74\, kips = 30.0\, kN$

$$V_r = \frac{V_n}{1.5} = \frac{32.9}{1.5} = 20.0\, kN$$

**3- 25 mm lateral displacement**

To find lateral strength corresponding to 25 mm displacement a braced model with strut width of w=122.3 mm was created in ETABS and analyzed. By iteration it was observed that 930 kN lateral load on top beam will cause 25 mm lateral displacement and 545.3 kN internal axial force in the strut. So, lateral strength of infill is equal to horizontal component of strut compression load as follow:

$$V_r = \frac{1930}{2164.5} * 545.3 = 486.2\, kN$$